

UC Irvine

UC Irvine Electronic Theses and Dissertations

Title

Mass Balance of the Earth's Glaciers and Ice Caps using multi-sensor data

Permalink

<https://escholarship.org/uc/item/8zb7p4tv>

Author

Ciraci, Enrico

Publication Date

2018

Copyright Information

This work is made available under the terms of a Creative Commons Attribution License, available at <https://creativecommons.org/licenses/by/4.0/>

Peer reviewed|Thesis/dissertation

UNIVERSITY OF CALIFORNIA,
IRVINE

Mass Balance of the Earth's Glaciers and Ice Caps using multi-sensor data

DISSERTATION

submitted in partial satisfaction of the requirements
for the degree of

DOCTOR OF PHILOSOPHY

in Earth System Science

by

Enrico Ciraci

Dissertation Committee:
Professor Isabella Velicogna, Chair
Professor Eric Rignot
Professor Mathieu Morlighem

2018

DEDICATION

To my parents

TABLE OF CONTENTS

	Page
LIST OF FIGURES	v
LIST OF TABLES	xi
ACKNOWLEDGMENTS	xii
CURRICULUM VITAE	xiii
ABSTRACT OF THE DISSERTATION	xv
1 Introduction	1
1.1 Glacier Mass Balance	4
1.2 Time-Variable Gravity for GIC Mass Balance	6
1.2.1 Time-Variable Gravity from GRACE	10
1.3 Satellite Altimetry for GIC Mass Balance	14
1.3.1 ICESat	14
1.3.2 CryoSat-2	15
1.4 Research Objectives and Outline of the Dissertation	19
2 Acceleration in mass loss of the GIC between 2002 and 2017	22
2.1 Introduction	23
2.2 Data and Methodology	25
2.3 Results	27
2.4 Discussion	32
2.5 Conclusions	37
3 Mass Balance of the Novaya Zemlya Archipelago between 2002 and 2017	44
3.1 Introduction	45
3.1.1 Study Region	46
3.1.2 Mass Balance of NZEM during the 20th Century	48
3.2 Data and Methods	52
3.2.1 Time Variable Gravity and Mascon Inversion	52
3.2.2 Satellite Altimetry	52
3.2.3 Noise Reduction - Local Regression Filter	58
3.2.4 Statistical Analysis	58

3.2.5	Spatial Extrapolation	59
3.2.6	From Volume To Mass Change	61
3.3	Other Data	64
3.3.1	Glacier Inventories	64
3.3.2	Glacier Hypsometry	65
3.3.3	Atmospheric Temperatures, Total Precipitation, and Ocean Data	66
3.4	Results	68
3.4.1	GRACE	68
3.4.2	ICESat and CryoSat-2	70
3.4.3	Single Drainage Basin Analysis	72
3.4.4	Surface Temperatures and Total Precipitation	73
3.4.5	Sea Ice Concentration and Sea Surface Temperatures	75
3.4.6	North Atlantic Oscillation	76
3.5	Discussion	76
3.6	Conclusions	79
4	Water Balance of the Indus River Basin between 2002 and 2012	97
4.1	Introduction	98
4.1.1	Study Region	100
4.2	Data and Methods	104
4.2.1	Time Variable Gravity and Mascon Inversion	104
4.2.2	Water Balance Model	106
4.2.3	Climatic Forcing	108
4.2.4	Other Datasets	109
4.3	Results	111
4.3.1	Comparison with GRACE	111
4.3.2	Comparison with River Gauges	113
4.3.3	Comparison with GRCDD	113
4.3.4	Comparison with Satellite Altimetry	114
4.3.5	Water Budget	114
4.3.6	Comparison with Ground Stations	116
4.4	Discussion	118
4.5	Conclusions	121
5	Conclusions	135
5.1	Summary of Results	136
5.2	Implications and Future Directions	138
	Bibliography	142

LIST OF FIGURES

	Page
1.1 GIC location map: (1) Alaska, (2) Western Canada–US, (3) Canadian Arctic Archipelago ((3a) Arctic Canada North, (3b) Arctic Canada South), (4) Iceland, (5) Svalbard, (6) Scandinavia, (7) Russian High Arctic Archipelagos, (8) North Asia, (9) Central Europe, (10) Caucasus Middle East, (11) High Mountains Asia, (12) Low Latitudes, (13) Southern Andes, (14) New Zealand. The names of the GIC regions are taken from the Randolph Glacier Inventory version 6.0 [Pfeffer et al., 2014].	2
2.1 (a) Glaciers and Ice Caps (GIC) mass change derived from GRACE for April 2002 to August 2016, in centimeter of water. (b) GRACE-derived ice mass time series for the GIC, with the best-fit quadratic trend (blue) line, with mean loss and acceleration in mass loss in $Gt = 10^{12}$ kg per year, and monthly errors (light blue).	39
2.2 (a) Glaciers and Ice Caps locations from the Randolph Version 6.0 inventory divided into 13 regions and subregions. GRACE-derived ice mass time series for the time period April 2002 - August 2016 are shown for (b) Canadian Archipelago, (c) Alaska, (d) the Southern Andes, (e) Iceland, (f) the Russian High Arctic, (g) High Mountain Asia, and (h) Svalbard in decreasing mass loss values. Data filtered for the seasonal dependence using a 13-month window are shown (gray dashed line). The blue line represents the best-fit linear or quadratic trend. Light color bands are monthly errors.	40
2.3 Ice mass time series, in gigatons (Gt): (a) Scandinavia, (b) Caucasus and Middle East, (c) North Asia, (d) Low Latitudes, (e) Central Europe, (f) New Zealand, and (g) Western Canada. Data filtered for the seasonal dependence using a 13-month window are shown (gray dashed line). The blue line represents the best-fit linear or quadratic trend to the time series. Light color band are monthly errors. Included are GRACE linear and quadratic trend. (h) location of the ice covered regions according to the Randolph Glacier Inventory.	41

2.4	Ice mass time series, in gigatons (10^{12} kg) for: (a) Canadian Arctic Archipelago, (b) Arctic Canada North, (c) Arctic Canada South, (d) Southern Andes, (e) North and South Patagonia Ice Fields, (f) Russian High Arctic, (g) Franz Joseph Land, (h) Novaya Zemlya, and (i) Severnaya Zemlya. Data filtered for the seasonal dependence using a 13-month window are shown (gray dashed line). The blue line represents the best-fit linear or quadratic trend to the time series. Light color band are monthly errors. Included are GRACE linear and quadratic trend estimates.	42
2.5	Ice mass time series for High Mountain Asia (HMA) from GRACE data for the time period April 2002 to March 2016. The distribution of mascons is shown for (b) region 11a (E and W Tien Shan), (c) region 11b (Karakoram, Hindu Kush, W Kunlun, Pamir, and Hissar Alay), (d) region 11c (Himalaya, Hengduan Shan S and E Tibet) and (e) region 11d (Qilian Shan, Inner Tibet and E Kunlun). Data filtered for the seasonal dependence using a 13-month window are shown (gray dashed line). The red line represents represents the best-fit linear or quadratic trend to the time series. Light color band are monthly errors. Included are GRACE linear and quadratic trend estimates.	43
3.1	(a) Novaya Zemlya Glaciers: in red, Marine-Terminating Glaciers facing the Kara Sea, in blue, Marine-Terminating Glaciers facing the Barents Sea, in green, Land-Terminating Glaciers facing the Kara Sea, in yellow, Land-Terminating Glaciers facing the Barents Sea, in orange, Minor Glaciers. Glaciers Outlines from Rastner et al. [2017]. (b) Location of Novaya Zemlya.	80
3.2	NZEM ice mass time series for the time period between April 2002 and August 2016. In black, the GRACE-derived mass change time series. The light grey band shows the monthly measurement error affecting GRACE estimates. The red line shows the ice mass loss estimated using ICESat between October 2003 and October 2009. The red-dashed lines represent the upper and the lower bounds of the estimated mass loss. In green, the mass change time series evaluated using CryoSat-2 between July 2010 and August 2016. The green error-bars correspond to estimated uncertainties in the monthly mass anomalies estimated using CryoSat-2. Time series and relative uncertainties are calculated as described in the main text.	83
3.3	Map of Ice Elevation Change for NZEM estimated using ICESat for the time period between October 2003 and October 2009. Regional glaciers outlines are extracted from the sixth release of the Randolph Glacier Inventory [Pfeffer et al., 2014].	84
3.4	Map of Ice Elevation Change for NZEM estimated using CryoSat-2 Method 1 (CryoSat-2-M1) for the time period between July 2010 and July 2016. Regional glacier outlines are extracted from the new glacier inventory described in Rastner et al. [2017].	85
3.5	Map of Ice Elevation Change for NZEM estimated using CryoSat-2 Method 2 (CryoSat-2-M2) for the time period between July 2010 and July 2016. Regional glacier outlines are extracted from the new glacier inventory described in Rastner et al. [2017].	86

3.6	Ice Elevation Change Uncertainty Map calculated for: (a) CryoSat-2 Method 1 (CryoSat-2-M1) and (b) CryoSat-2 Method 2 (CryoSat-2-M2). Grid-points uncertainty values are calculated as described in the text and expressed in meters-per-year [m/yr]. Regional glacier outlines from Rastner et al. [2017].	87
3.7	Elevation Vs Elevation Changes calculated for the major marine-terminating glaciers facing the Kara Sea calculated using ICESat, CryoSat-2 - M1, and CryoSat-2 - M2. (a) Novaya Zemlya Glaciers, (b) Moshniy Glacier, (c) Koproktin Glacier, (d) Navopashenny Glacier, (e) Vershinsky Glacier, (f) Rozhdestvensky Glacier, (g) Roze Glacier, (h) Vylki and Shury Glaciers.	88
3.8	Elevation Vs Elevation Changes calculated for the major marine-terminating glaciers facing the Kara Sea calculated using ICESat, CryoSat-2 - M1, and CryoSat-2 - M2. (i) Novaya Zemlya Glaciers, (l) Krayniy Glacier, (m) Arkhangelosky Glacier, (n) Inostrntsev Glacier, (o) Borzov Glacier, (p) Tssija Glacier, (q) Rikachev Glacier, (h) Shokalsky Glacier.	89
3.9	Elevation Vs Elevation Changes calculated for the major land-terminating glaciers facing the Kara Sea calculated using ICESat, CryoSat-2 - M1, and CryoSat-2 - M2. (a) Novaya Zemlya Glaciers, (b) NZ South East Glaciers, (c) RGI60-09.0073, (d) RGI60-09.0013, (e) RGI60-09.0015. Glaciers with not available name are identified using the relative Randolph Inventory ID.	90
3.10	Elevation Vs Elevation Changes calculated for the major land-terminating glaciers facing the Barents Sea calculated using ICESat, CryoSat-2 - M1, and CryoSat-2 - M2. (a) Novaya Zemlya Glaciers, (b) NZ South East Glaciers, (c) RGI60-09.0073, (d) RGI60-09.0013, (e) RGI60-09.0015. Glaciers with not available name are identified using the relative Randolph Inventory ID.	91
3.11	(a), Seasonal Atmospheric Temperature Anomaly (ERA/Interim - monthly means 2 meters temperature) calculate using the interval between 1979 and 2002 as a reference period. (b), Total Seasonal Precipitation (ERA/Interim - Total Precipitation Synoptic Monthly Means) Anomaly calculated using the interval between 1979 and 2002.	92
3.12	Comparison between mean summer temperature (JJA) from ERA/Interim and annual mass balance from GRACE for the time period 2002 – 2016.	93
3.13	Time series of (a) winter North Atlantic Oscillation Index (DJFM NAO), and (b) Annual North Atlantic Oscillation Index (Annual NAO). The black dashed lines represents the smoothed version of the indices time series obtained using a seven-year moving average filter applied to to remove low-frequency variability and assess annual and decadal relations.	94

3.14	Validation of Surface Temperature and Total Precipitation calculated using ERA/Interim with direct observation from the weather station located at Malye Karmakuly (NZEM) provided by the World Data Centre Baselain Climatological Data Sets. (a, c) Atmospheric Temperature and Total Precipitation measured by the Weather Station at Malye Karmakuly. (b, d) Atmospheric Temperature and Total Precipitation employing data from ERA/Interim linearly interpolated at the Malye Karmakuly station location. ERA/Interim correctly reproduces monthly/seasonal surface temperature. Seasonal total precipitation evaluated using the two datasets show instead different patterns. This difference is probably related to the systematic underestimation of solid precipitation by the climatic station.	95
3.15	Sea Surface Temepatures (SST) and Sea Ice Concentration (SIC) calculated for the Barents Sea and the Kara Sea Coasts. (a, b) SST expressed as seasonal anomalies calculated with respect the time period 1979 - 2002. (c, d) SIC expressed as percentage of the total coastal area covered by sea ice. The black error bars are	96
4.1	Indus River Basin. The Upper Indus Basin (UIB) is defined as the part of the region located above 2,000 meters. In Red the ice covered regions according to the sixth release of the Randolph Glacier Inventory [Pfeffer et al., 2014]. .	124
4.2	Indus Basin Irrigation System (IBIS). Red dots indicate the location of the four river gauges provided by the Water and Power Development Authority (WAPDA). Green dots indicate the position of all the climatic stations used to validate precipitation and temperature from WBM. The background of the figure shows the percentage of the total area equipped for irrigation on a 5 arc-minute grid extracted by the version 5.0 of the Global Map of Irrigation Areas distributed by the Food and Agriculture Organization of United Nations (FAO) and available at (http://www.fao.org).	125
4.3	Mascon Configuration used to evaluate monthly gravity anomalies over the Indus River Basin. Each mascon is designed as 3.1 a degrees spherical cap. Spherical Caps used to extract the gravity signal relative to the Upper Indus Basin (UIB) are reported in blue, those used for the Lower Indus Basin (LIB) are reported in red. The gray spherical caps are used to cover regions surrounding the Indus River Basin in order to minimize the effect of their gravity signal on our final estimates. The background of the figure represents the total water storage (TWS) trend map extracted from GRACE for the time period between April 2002 and December 2012. The trend map was smoothed using a 350 km radius Gaussian smoothing filter. The purple dots indicate the location of the High Mountains of Asia glaciers.	126

4.4	(a): Upper Indus River Basin (UIB): TWS anomaly for the time period between December 2002 and April 2012 from GRACE (in blue), WBM/Era Interim (in green) and WBM/APHRODITE. (b): Average annual TWS anomaly calculated from the time series presented in (a). (c): Lower Indus River Basin (LIB): TWS anomaly for the time period between December 2002 and April 2012 from GRACE (in red), WBM/Era Interim (in green) and WBM/APHRODITE (in gold). (d): Average annual TWS anomaly calculated from the time series presented in (c). Monthly mass anomaly values are expressed in giga-tonnes. Linear trend have been removed from the original time series.	127
4.5	(a): Indus River Basin, with location of the considered river gauges. (b, c, d, e): Monthly river discharge time series measured at the interface between the UIB and the LIB for the main Indus River tributaries within the Pakistani territory. Monthly discharge measured by WAPDA river gauges are in red. Discharge time series simulated by WBM/Era Interim and WBM/Aphrodite are in green and gold. Discharge time series are expressed in giga-tonnes. Mean error values are calculated as the average difference between river gauges measurements and WBM estimates.	128
4.6	Average monthly discharge evaluated at the Indus River Delta. In red, estimates by the GRFCDD project; in blue and gold, estimates by WBM/ERA Interim and WBM/APHRODITE.	129
4.7	(a): Indus River Basin, with location of the considered altimetric virtual stations from the DAHITI project. (b-o): comparison between normalized river elevation time series and normalized river flux estimates from WBM. Altimetry time series are in red. Normalized discharge time series simulated by WBM/Era Interim and WBM/Aphrodite are in green and gold	130
4.8	Water Budget: (a) Upper Indus River Basin (UIB): In blue, TWS average annual climatology from GRACE; in green, TWS average annual climatology from WBM; in brown, (U2L - Disch) average monthly discharge simulated by WBM at the interface between UIB and LIB; in yellow, average monthly runoff calculated as $R = P - ET - TWS$, where P and ET are extracted from WBM and TWS is measured by GRACE. (b) Lower Indus Basin (LIB): In blue, TWS average annual climatology from GRACE; in green, TWS average annual climatology from WBM; in brown, (U2L - Disch) average monthly discharge simulated by WBM at the Delta of the Indus River Basin; in yellow, average monthly runoff calculated as $R = P - ET - TWS + U2L - Disch$, where P and ET are extracted from WBM and TWS is measured by GRACE. Monthly mass anomaly values are expressed in giga-tonnes. The values reported in the boxes on the lower-left of each subfigure represents the summer mass loss/gain calculated for each climatology as the difference between values assumed between November and May.	131

4.9	(a-b) Upper Indus River Basin Water Budget: In blue, TWS average annual climatology from GRACE; in green, TWS average annual climatology from WBM; in brown, (U2L - Disch.) average monthly discharge simulated by WBM at the interface between the UIB and the LIB; in yellow, average monthly runoff calculated as $R = P - ET - TWS$, where P and ET are extracted from WBM and TWS is measured by GRACE. (c-d) Lower Indus Basin Water Budget: In blue, TWS average annual climatology from GRACE; in green, TWS average annual climatology from WBM; in brown, (U2L - Disch.) average monthly discharge simulated by WBM at the Delta of the Indus River Basin; in yellow, average monthly runoff calculated as $R = P - ET - TWS + U2L - Disch.$, where P and ET are extracted from WBM and TWS is measured by GRACE.	132
4.10	(a): comparison between monthly temperatures from WBM/ERA Interim and temperatures measured by the 55 stations available within the Indus River Basin. (b): comparison between monthly temperatures from WBM/APHRODITE and temperatures measured by the 55 stations available within the Indus River Basin. The blue and red circles represent the sign and the amplitude of the mean error calculated as the mean of the monthly difference between measurements from the station and values estimated by the model at the same locations.	133
4.11	(a): comparison between monthly total precipitations from WBM/ERA Interim and precipitations measured by the 55 stations available within the Indus River Basin. (b): comparison between monthly total precipitation from WBM/APHRODITE and those measured by the 55 stations available within the Indus River Basin. The blue and red circles represent the sign and the amplitude of the mean error calculated as the mean of the monthly difference between measurements from the station and values estimated by the model at the same locations.	134

LIST OF TABLES

	Page
2.1 Longterm mass balance and acceleration calculated between April 2002 and August 2016. AIC_c indicates the model that best fits the signal based on the Akaike Information Criterion: L indicates linear model and Q quadratic model. $R_{adj}^2(L)$ and $R_{adj}^2(Q)$ are R-squared adjusted for linear (L) and quadratic (Q) model respectively, F-test indicates at which statistical level the improvement in the quadratic model fit is significant. Accelerations are reported only when the quadratic model provides the best fit to the regional time series according to the AIC_c criteria and the acceleration is statistically significant; otherwise a linear fit is used.	39
3.1 Annual Mass Balance of Novaya Zemlya expressed in Giga-tons [Gt].	81
3.2 NZEM Glacier Mass Balance calculated with GRACE. The table contains the Glacier Mass Change rates for the three time period analyzed in this study. Total mass balance and its components are expressed in Giga-tons [Gt] Uncertainties are calculated as described in the text.	81
3.3 Mass Change rates for NZEM glaciers and for the five considered sub-regions obtained with CryoSat-2-M1 and CryoSat-2-M2. NZEM glaciers are classified according coast and terminus type. Mass change rates are expressed in Giga-tons per year.	82
3.4 Ice Thinning Rate measured at below 500 m near the glacier frontal areas. NZEM glaciers are classified according coast and terminus type. Thinning rates are expressed in meters per year.	82
4.1 Mass Budget components calculated using WBM/ERA Interim	123
4.2 Mass Budget components calculated using WBM/APHRODITE	123

ACKNOWLEDGMENTS

I would like to thank my advisor Isabella Velicogna for giving me the opportunity to work in her lab, for her guidance through this research work, and for teaching me to look at things from a different perspective.

I wish to thank my dissertation committee members Eric Rignot and Mathieu Morlighem for their comments, suggestions, and insights on this research.

I would also like thank the UC Irvine Earth System Science department for supporting me and my fellow graduate students. Thank you to my longtime lab group members Tyler C. Sutterley, Chia-Wei Hsu, Yara Mohajerani, Meng Zhao, Zhuoya He, Geruo A and Kishore Pangaluru.

I would like thank my girlfriend Valentina. With all her love and support, she helped me to achieve this important result.

Finally, I would like to especially thank my cohort and the rest of the friends I've made here at UCI for being there along the way.

This work was performed at the University of California, Irvine and at the Jet Propulsion Laboratory. Funding for this research was supported by the NASA's Cryosphere, Interdisciplinary Science, Hydrology and High Mountain Asia Programs.

CURRICULUM VITAE

Enrico Ciraci

EDUCATION

Doctor of Philosophy in Earth System Science University of California, Irvine	2018 <i>Irvine, California</i>
Master of Science in Earth System Science University of California, Irvine	2014 <i>Irvine, California</i>
Master degree in Technologies for Remote Sensing University of Bari, Italian Space Agency (ASI)	2012 <i>Bari, Italy</i>
Master of Science in Telecommunications Engineering Polytechnic University of Bari	2010 <i>Bari, Italy</i>
Bachelor of Science in Telecommunications Engineering Polytechnic University of Bari	2008 <i>Bari, Italy</i>

RESEARCH EXPERIENCE

Graduate Research Assistant University of California, Irvine	2012–2018 <i>Irvine, California</i>
--	---

TEACHING EXPERIENCE

Teaching Assistant University of California, Irvine	2013–2016 <i>Irvine, California</i>
---	---

REFEREED JOURNAL PUBLICATIONS

P. Kishore, I. Velicogna, T. C. Sutterley, Y. Mohajerani, **E. Ciraci**, G. N. Madhavi, “A case study of mesospheric planetary waves observed over a three-radar network using empirical mode decomposition,” *Annales Geophysicae*, 2018. 10.5194/angeo-36-925-2018.

P. Kishore, J. Jayalakshmi, P. Lin, I. Velicogna, T. C. Sutterley, **E. Ciraci**, Y. Mohajerani, S. Kumar “Investigation of Kelvin wave periods during Hai-Tang typhoon using Empirical Mode Decomposition,” *Journal of Atmospheric and Solar-Terrestrial Physics*, 2017. 10.1016/j.jastp.2017.07.025.

REFEREED CONFERENCE PUBLICATIONS

Ciraci, E., Velicogna, I., Fettweis, X., Mass Balance of Novaya Zemlya Archipelago from 2002 to Present. *Poster, AGU Fall Meeting 2017*

Ciraci, E., Velicogna, I., Fettweis, X., van den Broeke, M. R. , High Arctic Glaciers and Ice Caps Ice Mass Change from GRACE, Regional Climate Model Output and Altimetry. *Poster, AGU Fall Meeting 2016*

Ciraci, E., Velicogna, I., Wahr J., Swenson, S. , Mass Loss of Glaciers and Ice Caps from GRACE during 2002-2015. *Poster, AGU Fall Meeting 2015*

Ciraci, E., Velicogna, I., Mass balance of the Canadian Arctic Archipelago using Remote Sensing. *Poster, AGU Fall Meeting 2014*

ACCOLADES

Best Student Thesis award

2010

IEEE Geoscience and Remote Sensing Society South Italy Chapter

ABSTRACT OF THE DISSERTATION

Mass Balance of the Earth's Glaciers and Ice Caps using multi-sensor data

By

Enrico Ciraci

Doctor of Philosophy in Earth System Science

University of California, Irvine, 2018

Professor Isabella Velicogna, Chair

The World's Glaciers and Ice Caps (GIC) contain a sea level rise (SLR) equivalent of about 0.4 m. Although their potential sea level contribution is small compared to Greenland (7.4 m) or Antarctica (58.3 m), the GIC are the largest contributor to global SLR at present. During the last 20 years, the GIC contributed 2.5 cm SLR vs 1 cm for Greenland and Antarctica. Rising global sea levels and posing a significant problem to society. Runoff from the melting GIC has an impact on the regional hydrology and freshwater supply. The latter is of great concern in highly populated regions such as Central Asia where it negatively affects economic activities and political stability. Defining consistent methodologies to monitor the state of GIC in these regions and reduce uncertainties regarding their specific ice mass loss and relative contribution to SLR is critical not only to science but to the public, policy development, and implementation. In this dissertation, we use available satellite and modeling techniques to estimate recent contribution to sea level rise by the ice-covered regions outside the two ice sheets during the last two decades. We estimate glacier mass balance employing: time-variable gravity measurements by the NASA GRACE mission, and satellite altimetry by the NASA ICESat and the ESA CryoSat-2 mission. These techniques are applied in key regions of the Arctic, where increasing atmospheric and ocean temperatures have led to accelerating glacier mass losses. In the second part of this work is focused on the glaciers High Mountains of Asia, the largest freshwater reservoir outside the Polar Regions. Here, we use

a mixture of remote sensed observations and atmospheric models to characterize the effect of glacier mass loss on the water cycle of the Indus River Basin. This work helps improve our general understanding of the mechanisms driving current glaciers and ice caps mass change and its relative impact on freshwater availability and sea level rise during the next century.

Chapter 1

Introduction

The World's Glaciers and Ice Caps (GIC) contain a sea level rise (SLR) equivalent of about 0.4 m [Vaughan et al., 2013] (see Figure 1.1). In the twentieth century, a marked increase in global atmospheric temperatures at the end of the Little Ice Age promoted a negative mass balance in most GIC. Estimates suggest that global GIC lost mass with an average rate ranging between 0.13 mm/year and 0.6 mm/year of Sea Level Rise (SLR) [Zuo and Oerlemans, 1997, Cogley, 2009, Dowdeswell et al., 1997, Meier et al., 2007]. Furthermore, SLR has accelerated during the last 50 years [Church et al., 2011]. Between 1993 and 2008, the global mean sea level rose at a rate of 3.22 ± 0.41 mm/year with 0.99 ± 0.04 mm/year attributed to GIC. Future projections indicate that the glacier shrinkage process will continue throughout the coming decades [Meier et al., 2007, Vaughan et al., 2013].

Runoff from water stored in snow and glaciers sustains river flow during the summer season and extended drought periods, when precipitations are scarce. For this reason, projected future glacier retreat is a reason of great concern in highly populated regions such as Central Asia. Here, river runoff generated upstream by meltwater from glaciers and snow is crucial to sustain the life of more than 1 billion people [Bolch et al., 2012, Immerzeel et al., 2010]. GIC

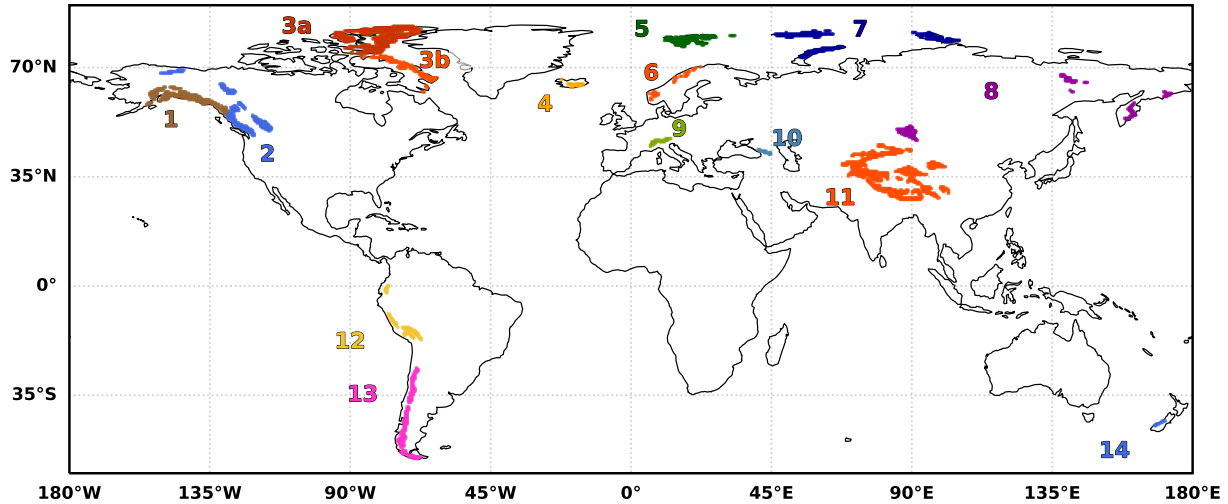


Figure 1.1: GIC location map: (1) Alaska, (2) Western Canada–US, (3) Canadian Arctic Archipelago ((3a) Arctic Canada North, (3b) Arctic Canada South), (4) Iceland, (5) Svalbard, (6) Scandinavia, (7) Russian High Arctic Archipelagos, (8) North Asia, (9) Central Europe, (10) Caucasus Middle East, (11) High Mountains Asia, (12) Low Latitudes, (13) Southern Andes, (14) New Zealand. The names of the GIC regions are taken from the Randolph Glacier Inventory version 6.0 [Pfeffer et al., 2014].

mass loss in the coming decades, is expected to drastically reduce river discharge [Immerzeel et al., 2010]. Declining river discharge, coincident with increasing population and heightened water demand, will enhance the risk of water stress. As a result, stressed regions are likely to face growing social instability, conflict, migration, and potential state collapse [Pritchard, 2017]. Defining consistent methodologies to monitor the state of GIC in these regions and reduce uncertainties regarding their specific ice mass loss and relative contribution to SLR is critical not only to science but also to the public, policy development, and implementation.

Pre-satellite era global assessments were obtained through interpolation of in-situ measurements based on local geodetic and glaciological techniques and glacier physical models

[Hirabayashi et al., 2010]. In the former case, estimates were based on a small and biased sample of the GIC, therefore affected by large uncertainties. In the latter, models did not capture the physical processes driving the glacier mass change at a local scale with high enough precision. Satellite observations provide a suitable tool to obtain a widespread characterization of regional GIC changes, at a uniform sampling, and with a known precision over long periods of time. They can thus be used to obtain a comprehensive assessment of the current state and future evolution of glaciers and relative contribution to SLR.

This research project aims at improving our understanding of the physical processes driving the GIC mass balance at present. We address this goal by employing independent satellite observation technologies combined with outputs from hydrological and reanalysis models.

In this work, we will pursue the following overarching science objectives:

- How is the mass balance of GIC changing in the current climate?
- What are the dominant physical processes driving the GIC mass balance and how do they change regionally and temporally?
- What is the actual contribution by glacier and snow melt to river discharge across the major river basins of Central Asia?
- How results from different data sources compare and how can this information be used to improve model forecast and the quality of the information provided to policy makers?

1.1 Glacier Mass Balance

GIC are perenniennial ice masses located in areas where climatic and topographic conditions allow snow to accumulate over many decades and centuries. Continuous accumulation increases the density of snow and compacts the deepest layers, gradually transforming snow into firn and finally into ice. Glaciers experience gravitational deformation and flow under their own weight as a result of mechanical deformation and basal sliding [Cuffey and Paterson, 2010]. This flux is directed from the accumulation areas toward lower areas the loss of snow and ice through melting, sublimation, wind erosion and calving (ablation) dominates. Accumulation occurs primarily as atmospheric precipitation, however wind deposition and/or avalanching of snow also contribute [Cuffey and Paterson, 2010]. The amount of ice stored within a glacier is not constant in time but varies according to the mutable environmental conditions (e.g. temperature and precipitation). Glacier mass balance (MB) is the index used in glaciology to characterize the state of a glacier and is the quantified difference between the mass input by accumulation and the mass output by ablation over a specified time interval, typically 1 year [Alley et al., 2007, Marshall, 2011]. MB is calculated as the integrated difference of two major components: surface mass balance (SMB) and ice dynamical discharge (D) (see Equation 1.1). SMB is quantified as the difference between mass inputs from precipitative fluxes in form of rainfall and snowfall (P) and mass losses by Runoff (RU) and sublimation (SU). RU is the portion of total snowmelt and liquid precipitation which is not maintained within the glacier's volume. SU is the total sublimation (from surface and drifting snow) and ER represents the snow and ice erosion by wind [van den Broeke et al., 2009]. The ice dynamics is determined by gravitational pulling and influences the rate of ice discharge into the oceans and the transport of ice from accumulation zones into ablation zones [Rignot and Kanagaratnam, 2006]. Glaciers flow via three different mechanisms: internal deformation,

decoupled sliding at the ice-bed interface, and deformation sediments [Marshall, 2011].

$$MB = \int (SMB - D)dt = \int ((P - RU - SU - ER) - D)dt \quad (1.1)$$

Interannual variability in glacier mass balance is influenced by annual precipitation and atmospheric temperatures [Marshall, 2011]. Glaciers are generally characterized according to their climate sensitivity and mass turnover. A classic distinction found in the literature is between maritime and continental glaciers. Maritime glaciers are usually found in mild and wet climates and characterized by high mass turnover. Continental glaciers are found in cool and dry climates and are characterized by lower mass turnover and higher sensitivity to changes in atmospheric temperatures [Marshall, 2011, Cuffey and Paterson, 2010]. The climate sensitivity of glaciers is usually parameterized in terms of glacier reaction and response time. The glacier reaction time is defined as the time lag between a climatic perturbation and the first glacier reaction (e.g. changes in MB and first retreat or advance of the glacier’s terminus). The response time is instead defined as the amount of time it takes for a glacier in equilibrium to reach a new state of equilibrium following a climatic perturbation [Marshall, 2011]. The reaction and response times of a glacier are strictly related to its mass. Small glaciers are characterized by short reaction and response time while the large ice caps in the polar regions have long reaction and response times.

The mass balance of glaciers can be quantified using three different approaches: the gravimetric method, the mass budget method, and the altimetric method. The gravimetric method evaluates changes in the total glacier’s mass by measuring temporal variations in the Earth’s gravity field. The mass budget method calculates the total glacier mass variation through the estimation of the different components of Equation 1.1. SMB is typically calculated employing specific models that reproduce input and output fluxes during the observation period [Lenaerts et al., 2013]. D is obtained employing measurements of the glacier’s velocity at a flux gate (usually the grounding line) obtained by Interferometric Synthetic Aperture Radar

(InSAR) or Optical Sensors together with estimates of ice thickness obtained by ice penetrating radars. [Millan et al., 2017, Rignot and Kanagaratnam, 2006, Strozzi et al., 2017]. The Altimetric method compares repeated measures of ice elevation to estimate temporal changes in the total glacier’s volume. The conversion from volume change to mass change requires information regarding the process driving the volume change or reconstruction of the ice density variation through the glacier profile in order to get the effective density of the change.

In this dissertation, we evaluate the GIC mass balance employing the gravimetric method and the altimetric method. In the next paragraphs, we provide a more detailed introduction to the two methodologies and to satellite systems used for their implementation.

1.2 Time-Variable Gravity for GIC Mass Balance

According to the Newton’s Law of Universal Gravitation, the force of attraction F between a central body (the Earth) of mass M and a second body of mass m located at a distance r is:

$$F = G \frac{Mm}{r^2} \tag{1.2}$$

where G is the universal gravitational constant ($6.674 \times 10^{-11} \text{ m}^3 \text{ kg}^{-1} \text{ s}^{-2}$) [Kaula, 2013, Hofmann-Wellenhof and Moritz, 2006]. Combining Equation 1.2 with Newton’s second law of motion ($F = ma$), we obtain the acceleration of the second body with respect to the center of mass of the dynamic system:

$$a = \frac{Gm}{r^2} \tag{1.3}$$

The gravitational acceleration a represents the magnitude of a vector directed along the line connecting the two bodies. The vector \vec{a} can be expressed as the gradient of a scalar function called gravitational potential.

$$\vec{a} = \text{grad}(V) = \frac{GM}{r} \quad (1.4)$$

Outside the central body, the gravitation potential satisfies Laplace's equation ($\nabla^2 V = 0$). The solutions of this equation are called harmonic functions [Kaula, 2013, Hofmann-Wellenhof and Moritz, 2006] and can be used to express the gravitational potential outside the central body:

$$V(r, \theta, \phi) = \frac{GM}{r} \left\{ 1 + \sum_{l=0}^{\infty} \sum_{m=0}^l \left(\frac{a}{r}\right)^l \tilde{P}_{lm}(\cos(\theta)) [\tilde{C}_{lm} \cos m\phi + \tilde{S}_{lm} \sin m\phi] \right\} \quad (1.5)$$

with, a being the average radius of the Earth ($\approx 6371 \text{ Km}$), r the geocentric radial coordinate, θ the colatitude, ϕ the longitude, and $\tilde{P}_{lm}(\cos(\theta))$ the fully-normalized associated Legendre polynomials of degree l and order m , and \tilde{C}_{lm} and \tilde{S}_{lm} are the fully-normalized spherical harmonic Stoke's coefficients [Kaula, 2013, Hofmann-Wellenhof and Moritz, 2006, Wahr, 2015]. The harmonic functions constitute an orthonormal basis, therefore, the integral over the unit sphere of the product of two different harmonics (with different l or m) is zero [Hofmann-Wellenhof and Moritz, 2006].

The total mass of the Earth is not distributed uniformly. For this reason, the gravitational attraction is not characterized by the spherical symmetry shown in Equation 1.4, but is more irregular. In physical geodesy, the shape of the gravitational field is described in terms of a surface of equipotential energy, the geoid. The geoid is defined as the equipotential surface that would coincide with sea surface if the oceans were at rest [Kaula, 2013]. The geoid height, or geoid ondulation, is defined as the distance between a reference ellipsoid, such as the WGS84 ellipsoid, and the geoid [Chao and Gross, 1987]. The geoid height, $N(\theta, \phi)$, at

colatitude θ and longitude ϕ , expressed in spherical harmonics is reported below:

$$N(\theta, \phi) = a \sum_{l=1}^{\infty} \tilde{P}_{lm}(\cos \theta) [C_{lm} \cos m\phi + S_{lm} \sin m\phi] \quad (1.6)$$

Temporal changes of the Earth's gravitational field are expressed in terms of changes of geoid height. Variations of the geoid height ΔN are commonly expressed in terms of the changes in the Stokes coefficients, $\Delta \tilde{C}_{lm}$ and $\Delta \tilde{S}_{lm}$. As reported in Wahr et al. [1998], the $\Delta \tilde{C}_{lm}$ and $\Delta \tilde{S}_{lm}$ coefficients are calculated by:

$$\begin{Bmatrix} \Delta \tilde{C}_{lm} \\ \Delta \tilde{S}_{lm} \end{Bmatrix} = \frac{3}{4\pi\rho_{ave}(2l+1)} \int \Delta\rho(r, \theta, \phi) \left(\frac{r}{a}\right)^{l+2} \tilde{P}_{lm}(\cos \theta) \begin{Bmatrix} \cos \phi m \\ \sin \phi m \end{Bmatrix} \sin \theta d\theta d\phi dr \quad (1.7)$$

where $\Delta\rho(r, \theta, \phi)$ is the density redistribution driving the variation in gravity and ρ_{ave} is the average density of the Earth ($\approx 5517 \text{ kg m}^{-3}$). $\Delta \tilde{C}_{lm}$ and $\Delta \tilde{S}_{lm}$ in Equation 1.7 provides information only on the radial integral of the density coefficients but not on how the density depends on depth within the Earth [Wahr, 2015]. Therefore, Equation 1.7 does not have a unique solution. A unique solution to the problem can be found assuming that the variations in geoid height are caused by mass redistribution concentrated within a thin layer near the Earth's surface. This assumption is acceptable considering that much of the fluctuation in global water storage and transport takes place within a very thin layer, of thickness $H \approx 10 \text{ km}$ that is small relative to the average radius of the Earth. In these conditions, $(l_{max} + 2/a \ll 1)$ and $(r/a)^{l+2} \approx 1$ for all values of l . Thus, Equation 1.7 reduces to:

$$\begin{Bmatrix} \Delta \tilde{C}_{lm}^{surf \ mass} \\ \Delta \tilde{S}_{lm}^{surf \ mass} \end{Bmatrix} = \frac{3}{4\pi\rho_{ave}(2l+1)} \int \Delta\sigma(\theta, \phi) \tilde{P}_{lm}(\cos \theta) \begin{Bmatrix} \cos \phi m \\ \sin \phi m \end{Bmatrix} \sin \theta d\theta d\phi dr \quad (1.8)$$

and the change in surface mass density $\Delta\sigma(\theta, \phi)$ can be uniquely calculated from the total gravitational field anomaly [Wahr et al., 1998].

Changes in superficial mass distribution induce an elastic response by the deep solid Earth that provides an additional contribution to the total geoid anomaly [Farrell, 1972]. This effect must be taken into account in order to fully characterize the gravitational signal at a given time [Wahr et al., 1998]. As reported in Wahr et al. [1998], the original surface mass redistribution and the consequent response by solid Earth are linked by the following relation:

$$\begin{Bmatrix} \Delta\tilde{C}_{lm}^{solid\ Earth} \\ \Delta\tilde{S}_{lm}^{solid\ Earth} \end{Bmatrix} = k_l \begin{Bmatrix} \Delta\tilde{C}_{lm}^{surface\ mass} \\ \Delta\tilde{S}_{lm}^{surface\ mass} \end{Bmatrix} \quad (1.9)$$

where k_l are the degree-dependent load Love Numbers reported in Wahr et al. [1998] and Farrell [1972]. The total geopotential can be expressed as the sum of the contribution by the superficial mass redistribution and the contribution by the elastic response by the deep solid Earth:

$$\begin{Bmatrix} \Delta\tilde{C}_{lm} \\ \Delta\tilde{S}_{lm} \end{Bmatrix} = \begin{Bmatrix} \Delta\tilde{C}_{lm}^{solid\ Earth} \\ \Delta\tilde{S}_{lm}^{solid\ Earth} \end{Bmatrix} + \begin{Bmatrix} \Delta\tilde{C}_{lm}^{surface\ mass} \\ \Delta\tilde{S}_{lm}^{surface\ mass} \end{Bmatrix} = (k_l + 1) \begin{Bmatrix} \Delta\tilde{C}_{lm}^{surface\ mass} \\ \Delta\tilde{S}_{lm}^{surface\ mass} \end{Bmatrix} \quad (1.10)$$

A new version of Equation 1.8 in which the contribution by the elastic response by the deep solid Earth has been taken into account is given below:

$$\begin{Bmatrix} \Delta\tilde{C}_{lm} \\ \Delta\tilde{S}_{lm} \end{Bmatrix} = \frac{3}{4a\pi\rho_{ave}} \frac{1 + k_l}{(2l + 1)} \int \Delta\sigma(\theta, \phi) \tilde{P}_{lm}(\cos\theta) \begin{Bmatrix} \cos m\phi \\ \sin m\phi \end{Bmatrix} \sin\theta \, d\theta \, d\phi \quad (1.11)$$

Inverting the former relation, we find the equation that expresses the changes in surface mass distribution $\Delta\sigma(\theta, \phi)$ in function of the Stokes Coefficients [Wahr et al., 1998]:

$$\Delta\sigma(\theta, \phi) = \frac{a\rho_{ave}}{3\rho_{H_2O}} \sum_{l=0}^{\infty} \sum_{m=0}^l \frac{2l + 1}{1 + k_l} \tilde{P}_{lm}(\cos\theta) [\Delta\tilde{C}_{lm} \cos m\phi + \Delta\tilde{S}_{lm} \sin m\phi] \quad (1.12)$$

1.2.1 Time-Variable Gravity from GRACE

The Gravity Recovery and Climate Experiment (GRACE) was a joint operation by the National Aeronautics and Space Administration (NASA) and the German Aerospace Center (DLR) that measured changes in the Earth’s gravitational field between 2002 and 2017 [Tapley et al., 2004]. GRACE measurements of time-variable gravity are a unique tool for studying changes in the distribution of the Earth’s liquid water, snow and ice [Wahr et al., 1998]. The satellite system consists of two identical satellites following each other on the same orbit at a distance of about 220 km. The two satellites are connected by a microwave ranging instrument that monitors their separation distance over time [Bettadpur, 2012]. The separation between the two satellites changes as they fly through spatial gradients in the gravity field [Wahr, 2015]. Changes in the Earth’s gravity field are measured by monitoring the temporal variation of the distance between the two satellites. The satellites fly at an elevation below 500 km, providing the system an unprecedented spatial resolution compared to previous generations of Satellite Laser Ranging systems (SLR). However, the low orbit elevation exposes the satellites to the effect of atmospheric drag, which can introduce spurious non-gravitational accelerations. These accelerations are measured by an on-board accelerometer and removed from the final gravity solutions [Wahr, 2015].

GRACE data are distributed by three processing centers: the Center for Space Research at the University of Texas (CSR), the Jet Propulsion Laboratory (JPL) and the German Research Centre for Geoscience (GFZ). Level-1 data consist of all the satellite measurements needed in order to compute solutions of the Earth’s gravity field, such as satellite-to-satellite distances, non-gravitational accelerations, spacecraft attitudes, and GPS positions of each satellite [Wahr, 2015]. The Level-2 data products consist of monthly averaged estimates of the Earth’s gravity field expressed in the form of spherical harmonics, \tilde{C}_{lm} and \tilde{S}_{lm} , supplied up to a maximum degree, l_{max} and order m_{max} , (typically $l_{max} = 120$) [Wahr, 2015]. The maximum spherical harmonic degree (l_{max}) is inversely proportional to the maximum spatial

resolution R of the GRACE data [Wahr et al., 1998, Wahr, 2015]:

$$R \approx \frac{20000}{l_{max}} km \tag{1.13}$$

Harmonics solutions are converted into maps of surface mass density changes by applying Equation 1.11. However, they need to be further post-processed, before the conversion, in order to reduce the contribution from possible error sources [Wahr, 2015]. The energy associated with a single harmonic of degree l decreases with increasing radius, r as $(a/r)^{l+1}$, where a is, again, the average radius of the Earth. A signal-to-noise ratio decreasing with l makes the measured gravity field less accurate over short wavelengths. Monthly solutions are, for this reason, truncated to a maximum degree l_{max} in order to improve the accuracy of the final solutions [Wahr et al., 1998]. However, the truncation introduces ringing artifacts from the Gibbs phenomenon [Wahr, 2015]. A simple way to reduce the effect of noise and truncation error is to use a degree-dependent Gaussian smoothing filter [Wahr et al., 1998]. A significant correlation between GRACE harmonics of the same degree introduces spurious north/south "stripes" easily detectable after the conversion into the spatial domain. Several solutions have been developed to reduce the effect of correlated error in the final gravity field estimates [Swenson and Wahr, 2006b]. Application of post-processing techniques can affect the amplitude of the original geophysical signal, such that it must be restored to obtain unbiased estimates of regional mass change [Swenson and Wahr, 2002, Landerer and Swenson, 2012].

Temporal variations of the gravity field are caused by a multitude of natural phenomena associated with mass redistribution above and below the Earth's surface. The main contributions to monthly variations of the gravity field arise from: regional changes in terrestrial water storage in form of water (including snow and ice); earthquakes and tectonic activity; glacial isostatic adjustment; sea level rise; ocean tides; and atmospheric and oceanic trans-

port [Wahr et al., 1998]. Given the non-uniqueness of the gravity-to-mass inversion problem discussed above, it is not possible to distinguish the contribution from any given geophysical processes from another to the gravity anomaly observed at a certain location [Wahr, 2015]. To isolate the mass change associated to a single signal component, the other contributions must be independently estimated and removed from the GRACE signal [Wahr, 2015]. In the case of GIC mass balance, changes in terrestrial hydrology outside of the ice covered regions and glacial isostatic adjustment constitute the largest source of uncertainty [Jacob et al., 2012b].

Least Squares Mascon Inversion

A major issue when using GRACE to evaluate mass storage changes on a regional scale is associated with the leakage error introduced by the signal ringing caused by the truncation of the spherical harmonic series. The local signal can be, in fact, contaminated by gravity signals originating at locations outside the region of interest [Swenson and Wahr, 2002, Wahr, 2015]. Several approaches, mainly based on the use of averaging kernels, have been developed in order to reduce this effect [Velicogna and Wahr, 2005, Swenson and Wahr, 2002]. In this dissertation, we employ the mascon approach presented in Jacob et al. [2012a]. A brief description of the inversion technique is reported below. A mascon is defined as a region with a uniform mass distributed over its surface. A mascon configuration is composed by a set of non-overlapping mascons designed in order to provide the best possible model for the mass redistribution field under study. Every mascon is therefore designed to minimize the error introduced by the assumption of uniform mass distribution and the real mass distribution within the mascon. For each mascon, we calculate a set of Stokes coefficients equivalent to 1 cm of water uniformly distributed over its surface. It is then possible to derive the relation between a GRACE spherical harmonics solution evaluated at time t , $\Delta\tilde{C}_{lm}(t)$, $\Delta\tilde{S}_{lm}(t)$ and

the sum of N mascons constituting our design matrix:

$$\begin{bmatrix} \Delta C_{00}^*(t) \\ \vdots \\ \Delta C_{l_{max}m_{max}}^*(t) \\ \Delta S_{00}^*(t) \\ \vdots \\ \Delta S_{l_{max}m_{max}}^*(t) \end{bmatrix} = \begin{bmatrix} C_{00}^{mascon,1} & \dots & C_{00}^{mascon,N} \\ \dots & \dots & \dots \\ C_{l_{max}m_{max}}^{mascon,1} & \dots & C_{l_{max}m_{max}}^{mascon,N} \\ S_{00}^{mascon,1} & \dots & S_{11}^{mascon,N} \\ \dots & \dots & \dots \\ S_{l_{max}m_{max}}^{*,1} & \dots & S_{l_{max}m_{max}}^{mascon,N} \end{bmatrix} \begin{bmatrix} c_1(t) \\ \vdots \\ \vdots \\ \vdots \\ c_N(t) \end{bmatrix} + \begin{bmatrix} \delta C_{00}^*(t) \\ \vdots \\ \delta C_{l_{max}m_{max}}^*(t) \\ \delta S_{11}^*(t) \\ \vdots \\ \delta S_{l_{max}m_{max}}^*(t) \end{bmatrix} \quad (1.14)$$

where, $\delta C_{lm}^*(t)$ and $\delta S_{lm}^*(t)$ represent the uncertainty associated to each harmonic coefficient at time t [Jacob et al., 2012a]. The solution to the problem is obtained least squares fitting the mascon Stokes coefficients with GRACE:

$$B = (M^T M)^{-1} M^T G \quad (1.15)$$

where, M is the mascon design matrix and G is the column vector containing the GRACE spherical harmonics. The solution of the normal equation returns N scale factors, one for each mascon. The mass variation associated to the mascon k is calculated as reported below:

$$M_k(t)[g] = (\hat{\beta}_k(t) * 1[cmw.e]) * A_k [cm^2] * \rho_{H_2O} \left[\frac{g}{cm^3} \right] \quad (1.16)$$

where $\hat{\beta}_k(t)$ and A_k are the scale factor and the total area of the mascon k .

1.3 Satellite Altimetry for GIC Mass Balance

1.3.1 ICESat

Launched in January of 2003, the NASA Ice, Cloud, and Land Elevation Satellite (ICESat) was an Earth orbiting laser altimeter designed to measure elevation changes of ice sheets and arctic ice caps in order to constrain their contribution to contemporary sea level rise [Zwally et al., 2002]. The mission was operative between February 2003 and October 2009, accomplishing the original requirements of a five year long mission. The main instrument carried by the satellite was the Geoscience Laser Altimeter System (GLAS), a single-beam laser altimeter operating at a wavelength of 1064 nm [Zwally et al., 2002]. The sensor accuracy has been proven to be higher than 0.05 m, allowing the detection of ice elevation changes as little as 1.5 cm/year over gently sloped terrain [Fricker et al., 2005]. The laser accuracy decreases to 0.5 m with higher sloped terrains [Brenner et al., 2007]. The satellite flew at an elevation of 600 kilometers with an orbit inclination of 94°. GLAS took measurements at 40-Hz, therefore sampling the Earth's surface elevation every 172 meters along the satellite flight direction with a footprint size of almost 70 meters [Schenk and Csatho, 2012] (The laser footprint has an elliptical shape with dimension 52 x 95 m for Laser 1 and 2 and 24 x 61 m for Laser 3 [Moholdt et al., 2010, Abshire et al., 2005]). The mission was equipped with three different lasers that intended to last for the lifetime of the mission (each laser had been designed to have a lifetime of 1-1.15 years) [Zwally et al., 2002, Brenner et al., 2007]. The first of the three lasers failed after just 38 days. For this reason, NASA was forced to redesignate the mission from continuous operation to a campaign mode. Instead of the planned 183-day repeat orbit, a 91-day repeat orbit with a 33-day sub-cycle was adopted. This resulted in a reduction of the number of ground tracks and the switch from temporally continuous coverage to a discrete one with campaigns 3 to 4 times per year. During the entire lifetime of the mission there were a total of 18 campaigns of 33 days [Borsa et al.,

2014]. In this dissertation, we use level-2 Global Land Surface Altimetry (GLAH14) release 34. The data are provided together with quality attributes and elevation corrections (range correction of the Troposphere, solid Earth Tide, ocean tide and pole tide) for each footprint. The data quality attributes include a wave saturation flag to indicate saturation of the sensor when recording the returned pulse and a correction of a potential bias in the extracted elevations [Smith et al., 2005].

1.3.2 CryoSat-2

The ESA CryoSat-2 satellite system was launched in April 2010 with the aim of providing the scientific community a powerful tool to study changes affecting the arctic regions (sea and land ice) in the context of a warming climate [Wingham et al., 2006]. CryoSat-2 payload consists of a highly sophisticated radar altimeter suitable to study sea and land ice with an unprecedented temporal and spatial resolution (short repeat cycle and small inter-track spacing). The use of radar technology allows the altimeter to work in all weather conditions with no limitations related to cloud coverage, which is persistent in the Arctic and highly affects laser altimeters. The satellite flies at an elevation of 717 km with an orbit inclination equal to 92° degrees that allows an almost unprecedented coverage of polar regions. Old generation radar altimeters like GeoSat, SeaSat, ERS1/2, and Envisat were designed as classic beam- and pulse-limited radar systems and were therefore characterized by large ground illumination diameters (2 - 15 kilometers) making them mainly usable for geodetic applications or measurement of changes in sea level and arctic sea-ice coverage [Wingham et al., 2006, Roca et al., 2009, Katsaros and Brown, 1991, Davis, 1992, Raney, 1998]. Given their coarse resolution, elevation measurements by these systems could not be used over small regions like the arctic ice caps or the ice sheets boundaries that are characterized by small size, steep slopes, and discontinuous surfaces. The CryoSat-2 mission overcomes these limitations employing a new generation delay-doppler radar altimeter, the SAR Interfero-

metric Radar Altimeter (SIRAL). Radar altimeters are usually designed with a single nadir looking antenna, and measure the distance between the satellite and the Earth surface included within the antenna footprint [Davis, 1992]. In this way the altimeter measures the distance between the satellite and the surface location closest to the satellite, called Point-Of-Closest-Approach (POCA). SIRAL is classified as a pulse limited delay-doppler altimeter (working in the Ku band - 13.573 GHz, wavelength ~ 2.2 cm) with a footprint size of $1.65 \times 1.65 \text{ km}^2$. Instead of transmitting a single pulse per time, SIRAL transmits a burst of 64 pulses every 50 microseconds. The returning echoes are affected by small shift in phase due to the movement of the satellite during the interval between the burst transmission and acquisition (delay doppler effect) [Raney, 1998]. The phase shift between the different echoes is used to increase the altimeter resolution along the direction of flight of the satellite (azimuth direction) up to a maximum of 400 meters on a flat terrain [Jensen and Raney, 1996]. The small size of the radar footprint enables, for the first time, application of satellite radar altimetry in regions like ice sheet margins and small arctic ice caps where the presence of steep slopes and discontinuous surfaces limited the application of previous microwave altimeters [Wingham et al., 2006]. CryoSat-2 is equipped with a secondary antenna that receives each backscattered signal from a slightly different position with respect to the primary one. The signals received by the two antennas are characterized by a shift in phase due to the different paths linking them to the ground scatterer. Analyzing the difference in phase delay between the two signals, SIRAL detects not only the range distance between the satellite and the ground scatterer but also its location in the across-track plane [Jensen, 1999, Rey et al., 2001]. SIRAL can operate in three different configurations:

- **Low Resolution Mode (LRM)**: in this case, the satellite operates like a conventional pulse-limited radar altimeter with a ground resolution of $1.65 \times 1.65 \text{ km}^2$. This operation mode is employed over the oceans and over the interior part of the ice sheets.

- Synthetic Aperture Radar Mode (**SARM**): in this configuration, bursts of radar pulses are transmitted consecutively within 50 microsecond intervals and processed coherently in order to increase the altimeter resolution along the azimuth direction up to 300-400 meters (over flat terrain). This is an unprecedented resolution for a radar altimeter [Wingham et al., 2006]. A single burst is composed of 64 consecutive pulses with a pulse repetition frequency of 18.182 Khz. A new burst is transmitted every 11.7 ms (A single bust must be transmitted and received before the transmission of a new burst). This second configuration is mainly used to study sea ice and sea level near the coasts, where the resolution of the LRM results too coarse [Jensen, 1999].
- SAR Interferometry Mode (**SARIn**): this mode is operated by employing a second antenna. The two antennas spaced by 1.2 meters, thus receiving the return echoes from a slightly different position. The phase delay present in the two echoes is analyzed and the direction of arrival (in the across-track plane) of the returning echoes is determined [Jensen, 1999]. This mode is used on the ice sheet margins and over glaciers and ice caps.

Large radar footprints pose major limitations to the application of CryoSat-2 in estimating elevation changes over GIC. Generally the radar footprint is more than an order or magnitude larger than any other lidar system. Radar performances significantly degrade over terrains with slopes higher than 1° due to increasing footprint size as a function of slope. However, Wang et al. [2015] demonstrated that even in these conditions, the accuracy of SIRAL is one order of magnitude higher than those of previous radar altimeters like ERS-e, ERS-2 and Envisat. A second major limitation on the use of radar altimeters like CryoSat-2 to study ice elevation changes is related to the temporal variability in the dielectric properties of ice and snow. Unlike lasers, whose signal energy is reflected almost entirely by the snow surface, the radar signal penetrates beyond the snow-air interface and is partially reflected by the interior layers of the snowpack/firn/ice column. The ratio between the energy of the radar signal

reflected by the snow surface (Surface Scattering) and the energy reflected by lower layers of the snowpack/firn/ice column (Volume Scattering) changes over time. The reflection ratio can vary from season to season and from year to year depending on the many variables that influence the snow layers such as water content, snow impurities, surface roughness, and the highly variable density between different layers. As an example, in dry seasons, the energy could be reflected not by the upper snow surface but by the previous summer's surface [McMillan et al., 2016, Nilsson et al., 2015b]. Elevation observations can therefore be influenced by past weather conditions. Temporal changes in glacier scattering properties can introduce variable biases in the determination of ice elevation and elevation changes. As reported by Nilsson et al. [2015b] changes in snowpack reflection properties have a relatively small influence on long-term ice elevation trend, but can introduce episodic extreme artifact changes. This can then influence the estimation of ice elevation variability, especially when estimated over short time periods [Gray et al., 2015, Nilsson et al., 2015b]. In this dissertation, we employ Level-2 Baseline-C SAR Interferometry mode elevation data provided by the European Space Agency [Bouffard et al., 2017]. Elevation data are distributed together with latitude, longitude, measurement acquisition time, geophysical and tidal corrections applied in the Level-2 processing, and several quality flags.

Elevation Change Estimation

Ice elevation changes with satellite altimeters have been historically estimated employing two approaches:

- Crossover Analysis;
- Collinear Analysis;

The crossover analysis estimates elevation changes at the intersection between ascending and descending orbits [Smith et al., 2005]. This approach has been widely used to study the mass balance of Greenland and Antarctica [Pritchard et al., 2012], however it is not the most applicable in the case of GIC [Moholdt et al., 2010]. Given that the large inter-track spacing and small size of these regions, the number of crossover points do not provide a large enough sample of the total glacier area. The available data sample results, for this reason, too sparse to be used to assess the regional glacier mass balance. A Collinear analysis or Along-Track approach, in these cases, is preferred. In this dissertation we evaluate ice elevation changes employing an updated version of the "plane-fit" technique presented in [Moholdt et al., 2010]. This approach evaluates ice elevation change rates and terrain slope by simultaneously least squares fitting a time-variable plane function to a set of measurements located within a selected spatial range. The simplest possible plane function, in which the glacier surface is approximated by a bilinear model, is presented below:

$$z(x, y, t) = \alpha_0 + \alpha_1 x + \alpha_2 y + \frac{dz}{dt} t \quad (1.17)$$

where α_1 and α_2 represent the planes slopes in the x and y directions, and $\frac{dz}{dt}$ is the rate of change of the plane's average elevation with time. The degree of the polynomial used to define the time-variable plane is chosen as the trade-off between the complexity of the model function (higher order polynomials provide a better approximation of the actual shape of the glacier's surface) and the total number of elevation measurements available within the considered spatial range.

1.4 Research Objectives and Outline of the Dissertation

The technical objectives for this research are listed below:

- Improve GIC mass balance estimates by GRACE developing post-processing techniques optimized for the study of these regions;
- Develop a robust statistical analysis approach to detect long-term trends and to study the inter-annual variability in the GIC mass balance time series;
- Design of new algorithms optimized to process altimetric data over GIC and to generate maps and time series of ice elevation change;
- Combine gravimetric and altimetric observations (when both available) in order to gain further insights about the physical processes driving the regional MB;
- Design new ad-hoc mascon configuration for studying glacier changes within the main river basins of Central Asia;
- Develop a standardized approach in order to use time-variable gravity from GRACE to validate hydrological and regional climates models over mountainous environments and reduce their uncertainties.

In Chapter 2, we present a new mascon configuration optimized to recover GIC mass change signal from GRACE. We present regional MB time series for the time period between April 2002 and August 2016 (equal to the life-time of the mission). We analyze the regional time series and we perform a rigorous statistical analysis in order to detect significant accelerations in mass loss during the time period under study.

In Chapter 3, we focus on the Novaya Zemlya Archipelago, in the Russian High Arctic. This regions has received significantly less attention by the scientific community compared the other GIC regions in the Arctic. The estimates previously available were based either in sparse ground observations or on the extrapolation of satellite observations over extremely short temporal intervals. We evaluate the glacier mass loss in the region using independent estimates by GRACE and by altimetric observations from the ICESat and the CryoSat-2

missions. We present a new algorithm designed to evaluate spatial and temporal characteristics of the evolution of ice elevation. We finally assess the impact of coast and terminus type in glacier thinning rates in order to evaluate the effect of different physical processes on the observed glacier mass loss. In Chapter 4, we present a new mascon configuration designed to study the water cycle of the major river basins of Central Asia with the aim of quantifying the contribution by glacier melt to the total river runoff available in the downstream regions. We use the Indus River Basin as a case study. We compare total water storage anomalies by GRACE with independent estimates from a high resolution hydrological model optimized to simulate the water cycle of the region. We employ results from the comparison to determine the best model set-up and we analyze the outputs from this model version to evaluate the partitioning of the total river discharge generation between precipitation and meltwater. We afterwards compare the model outputs with a set of independent satellite and ground based observations in order to detect the main sources of uncertainties in the climatic forcing used to constrain the model.

In Chapter 5 we summarize the major findings and implication of this dissertation.

Chapter 2

Acceleration in mass loss of the GIC between 2002 and 2017

We use time series of time-variable gravity from the NASA/DLR GRACE mission to evaluate the mass balance of Glaciers and Ice Caps (GIC) for April 2002 to August 2016, excluding Antarctica and Greenland peripheral glaciers. We report a mass loss of 209.7 ± 39.0 Gt/yr, with an acceleration of 6.7 ± 2.5 Gt/yr², equivalent to a 0.6 ± 0.1 mm/yr sea level rise and a potential 13.2 ± 3.5 cm sea level rise for the next century. Seven regions dominate the mass loss, 3/4th from the Arctic: Canadian Arctic Archipelago, CAA (68.1 ± 9.7 Gt/yr), Alaska (57.1 ± 10.5 Gt/yr), Southern Andes (35.1 ± 19.2 Gt/yr), Iceland (15.2 ± 4.5 Gt/yr), Russian High Arctic (14.5 ± 6.5 Gt/yr), High Mountain Asia, HMA (14.3 ± 12.7 Gt/yr), and Svalbard (9.0 ± 2.8 Gt/yr). The majority of the acceleration in loss is from CAA (3.5 ± 0.6 Gt/yr²), HMA (2.9 ± 0.7 Gt/yr²), Svalbard (0.9 ± 0.2 Gt/yr²), and Russian High Arctic (0.4 ± 0.3 Gt/yr²). In HMA and the Arctic, strong inter-annual variabilities in mass balance, larger than the long term trends, complicate the analysis but hold potential to inform regional atmospheric climate models.

2.1 Introduction

The World's Glaciers and Ice Caps (GIC) contain a sea level rise (SLR) equivalent of about 0.4 m [Vaughan et al., 2013]. Although their potential sea level contribution is small compared to Greenland (7.4 m) or Antarctica (58.3 m), the GIC has been the largest contributor to global SLR in the last 20 years. They contributed 2.5 cm SLR vs 1 cm for Greenland and Antarctica [Vaughan et al., 2013].

Runoff from the GIC has a major impact on the regional hydrology and freshwater supply. The latter is of great concern in highly populated regions such as the Indian subcontinent where it affects economic activities and political stability [Bolch et al., 2012, Rupper et al., 2012, Koppes et al., 2015]. Defining consistent methodologies to monitor the state of GIC in these regions and reduce uncertainties regarding their specific ice mass loss and relative contribution to SLR is critical not only to science but also to the public, policy development, and implementation.

Pre-satellite era global assessments were obtained through interpolation of in-situ measurements based on local geodetic and glaciological techniques and glacier physical models [Hirabayashi et al., 2010]. In the former case, estimates were based on a small and biased sample of the GIC, therefore affected by large uncertainties. In the latter, models did not capture the physical processes driving the glacier mass change at a local scale with high enough precision.

Previous studies [Tiwari et al., 2009, Jacob et al., 2012b] have demonstrated the use of satellite gravimetry from the Gravitational Recovery and Climate Experiment (GRACE) to generate regional GIC ice mass change estimates. Jacob et al. [2012b] calculated a GIC mass loss, outside Greenland and Antarctica, of 148 ± 30 Gt/yr during 2003-2010. Gardner et al. [2013] compared GRACE-derived GIC estimates with estimates from satellite laser altimetry and extrapolations of in situ measurements to yield a consensus mass loss for 2003-2009 of

215 ± 26 Gt/yr, outside Greenland and Antarctica. More recently, Rietbroek et al. [2016] reported a lower loss of 141 ± 26 Gt/yr for 2002-2014 by applying a joint least-squares inversion including GRACE, altimetry and GPS data, whereas Schrama et al. [2014] found a loss of 162 ± 10 Gt/yr for 2003-2013. Reager et al. [2016] estimated a 253 ± 35 Gt/yr mass loss for 2002-2014 mixing estimates for different time periods and different methodologies: 2002-2014 GRACE-derived estimates for Alaska, CAA, Iceland, Svalbard, and Russian High Arctic; 2003-2009 altimetry-derived estimates for HMA [Gardner et al., 2013]. These studies used variable, short time periods, which makes it difficult to compare the different estimates and come up with a consensus estimate because the mass balance signal also exhibits a strong temporal variability. Similarly, these studies have not examined the acceleration in mass loss of the GIC and the impact of the inter-annual variability of the signal on estimating the acceleration.

Here, we use a complete time series of GRACE observations to improve the estimation of the GIC mass balance for April 2002-August 2016. We do not include solutions obtained after October 2016 when only one accelerometer remained in operation because the errors in the GIC signal became too large after that date. We employ an optimized mascon configuration that best fits the latest Randolph Glacier Inventory version 6.0 (RGI) [Pfeffer et al., 2014] and minimizes the uncertainty in ice loss retrieval. We evaluate if the mass loss has accelerated at a significant level during the analyzed period at the regional and global scales. We examine how different regions contribute to the total GIC mass loss and acceleration in mass loss and discuss the linkage of the mass loss with climatic processes driving the mass changes. We conclude on the importance of the GIC in the global SLR budget and its decadal rate of acceleration.

2.2 Data and Methodology

We use 156 monthly GRACE Release-5 (RL05) spherical harmonic gravity solutions truncated to degree 60 from the Center for Space Research at the University of Texas for the period April 2002-August 2016 [Tapley et al., 2004, Bettadpur, 2012]. We employ monthly C_{20} coefficients from satellite laser ranging [Cheng et al., 2013] and include degree-1 coefficients calculated following Swenson et al. [2008]. We include an additional pole tide correction to remove the long-period pole tide signals not included in the standard correction [Wahr et al., 2015]. We remove the glacial isostatic adjustment (GIA), i.e. the viscoelastic response by the solid Earth after the ice removal at the end of the last ice age, using A et al. [2013] GIA model. We remove the effects of post-Little Ice Age (LIA) isostatic rebound, not included in the GIA model, using Jacob et al. [2012b] and Sørensen et al. [2017] corrections.

To isolate the GIC signal, the GRACE data are corrected for contamination by the land hydrology signal using the average output from two updated land surface models: 1) the latest version of the Community Land Surface Model (CLM) version 4.5 [Oleson et al., 2013] and 2) the new Global Land Data Assimilation System 2 (GLDAS-2) model, version NOAH-3.3 at 0.25° resolution [Rodell and Beaudoing, 2016]. The hydrology correction is only applied to regions surrounding the glaciers. In addition, in High Mountain Asia (HMA), we minimize the leakage from the groundwater signal in the plains of northern India, Pakistan, and Bangladesh [Rodell et al., 2009, Tiwari et al., 2009] by covering these regions with specific mascons.

We calculate glacier mass change time series using least squares fit mascon introduced in Chapter 1. We develop a new mascon configuration following the approach presented in Jacob et al. [2012b] (Figure 2.1, 2.2). Every mascon is composed by many small blocks with area equal to $0.5^\circ \times 0.5^\circ$ degrees. We manually adjust the blocks that define each mascon to ensure that all glacierized area larger than 100 km^2 are included. We define the mascon

shape to optimize the recovery of the glacier signal, to minimize the leakage from outside the region due to signal truncation and the leakage due to the assumption that the mass change is uniform within each mascon [Jacob et al., 2012b, Velicogna and Wahr, 2013]. We cover Greenland and Antarctica with mascons to avoid leakage from these areas into our solution. For each mascon, we calculate the set of Stokes Coefficients which we smooth with a 150 km Gaussian function and convert into mass. We simultaneously fit the mascon Stokes coefficients to the monthly GIA and hydrology corrected GRACE coefficients to obtain estimates of the monthly mass variability for each mascon. We calculate the regional ice mass time series by summing the contributions from all mascons within the region.

We calculate the glacier mass trend and acceleration by simultaneously fitting to the glacier mass time series an annual, semiannual, linear trend, and constant for the mean mass change, and an annual, semiannual, quadratic trend, and constant for the acceleration in mass change. To compare the quadratic and linear models, we use a variant of the Akaike Information Criterion, AIC_c for use with small sample sized datasets [Burnham and Anderson, 2002] that accounts for the goodness of the fit and the number of parameters, and rigorously identifies which model best fits the data. We only report acceleration that satisfies the AIC_c criteria and is significant at the $2\text{-}\sigma$ level. For major GIC contributors and subregions, we calculate the R_{adj}^2 for both the linear and the quadratic models which provides the percent of variance of the observed signal explained by the model. R_{adj}^2 increases only if the additional term improves the model more than would be expected by chance. To evaluate at which statistical level the improvement in the quadratic model fit is significant, we use an F-test. Finally, we also estimate the inter-annual variability of the signal in the different regions. To do so, we remove the long term trend (linear or quadratic based on the statistical test) from the 13-month smoothed time series and calculate the amplitude of the inter-annual variability.

Uncertainty in the glacier mass changes combines GRACE measurement errors, GIA and

LIA errors, hydrology correction error, leakage errors, and ocean mass correction errors. The ocean mass correction is applied by processing centers prior to computing gravity field solutions using the Ocean Model for Circulation and Tides (OMCT) ocean general circulation model Dobslaw et al. [2013] and the statistical uncertainty of the model fit (Table S1). Trends uncertainties due to the ocean mass correction are calculated following Velicogna and Wahr [2013]. GRACE measurement errors are calculated following Wahr et al. [2006]. GIA, LIA, and hydrology correction errors are calculated as in Jacob et al. [2012b] and Gardner et al. [2013]. To evaluate the leakage error, we use a Monte Carlo approach. For each mascon in each glacier region, we generate 10,000 synthetic monthly mass changes that are non-uniformly distributed within the blocks composing each mascon by distributing the monthly mass anomaly calculated assuming the uniform mass distribution using 10,000 Gaussian pseudo-random weight with standard deviation equal to 1 and zero mean. We apply our mascon procedure to the data and calculate the $2\text{-}\sigma$ of the difference between the mass obtained with the uniform distribution and that obtained with the non-uniform distribution. The total error is calculated as the sum in quadrature of the different errors

2.3 Results

Time series for the total GIC mass loss (Figure 2.1) and the largest contributors (Figure 2.2) are shown along with mass changes and accelerations (Table 2.1). Subregions are shown in Figure 2.3 and the remaining GIC regions in Figure 2.4. During 2002-2016 the total GIC mass loss, outside Greenland and Antarctica, is 209.7 ± 39.0 Gt/yr, with a statistically significant acceleration in loss of 6.7 ± 2.5 Gt/yr² (Figure 2.1b). This total loss combines a mass loss of 217 ± 32 Gt/yr for 11 regions with a mass gain of 8.4 ± 15 Gt/yr for 3 regions (Scandinavia, North Asia and Caucasus Middle East). The R_{adj}^2 is 97% (p<0.001) for the quadratic model and a difference in fit skill between the quadratic and linear models of 2%

significant at the 99.9% confidence level.

Seven regions covering 94% of the total GIC area account for 98% of the total mass loss: 1) the Canadian Archipelago (CAA), 2) Alaska, 3) Southern Andes, 4) Iceland, 5) Russian High Arctic, 6) High Mountain Asia (HMA) and 7) Svalbard. The Arctic alone, with 65% GIC in area, accounts for 78% of the mass loss (CAA, Alaska, Iceland, Svalbard, Russian High Arctic) (Table 2.1).

The CAA exhibits the largest mass loss of all regions with 68.1 ± 9.7 Gt/yr and the largest acceleration in loss of 3.5 ± 0.6 Gt/yr² (Figure 2.2b), with a R_{adj}^2 of 97%(p<0.001) for the quadratic model (vs 95%(p<0.001) for the linear). The quadratic improvement is significant at the 99.9% confidence level. For the northern part of the Archipelago (Arctic Canada North, Fig 2.4b), we find a mass loss of 36.8 ± 6.7 Gt/yr and an acceleration in loss of 2.2 ± 0.4 Gt/yr² versus 31.3 ± 6.1 Gt/yr and 1.3 ± 0.3 Gt/yr² for the southern part (Arctic Canada South, Figure 2.4c). The quadratic R_{adj}^2 is 95%(p<0.001) (vs 93%(p<0.001) for the linear) and the improvement of the quadratic fit significant at the 99.9% confidence level. Over the time period 2003-2009, our estimated mass loss for CAA of 55 ± 10 Gt/yr agrees with Gardner et al. [2013] GRACE RL05 (58 ± 9 Gt/yr) and consensus (60 ± 6 Gt/yr) mass loss. Over Sep 2003-Sep 2012, our estimated mass loss of 69 ± 9 Gt/yr agrees with Lenaerts et al. [2013] (69 ± 6 Gt/yr). Our record extends the previous records by several years and unambiguously reports acceleration in the mass loss of CAA for the entire period 2002-2016.

Alaska (Figure 2.2c) has the second largest mass loss with 57.1 ± 10.5 Gt/yr. In contrast to CAA, we find no significant acceleration in mass loss during the observation period, R_{adj}^2 is 93%(p<0.001) for both the quadratic and linear models. Results for the Canadian Archipelago and Alaska are in line with what observed by Harig and Simons [2016] for the period 2002-2014.

The Southern Andes (Figure 2.2d) have the third largest loss with 35.1 ± 19.2 Gt/yr, almost

entirely due to the Northern and Southern Patagonia ice fields (NSPI) (26.7 ± 7.4 Gt/yr, Figure S2), with no significant acceleration. The R_{adj}^2 is 69%($p < 0.001$) and 92%($p < 0.001$) for both the quadratic and linear fits for the Southern Andes and the northern and southern Patagonia ice fields, respectively. The estimated mass loss for NSPI over the time 2002-2012 agrees within the error bounds with Willis et al. [2012].

Iceland (Figure 2.2e) has the fourth largest loss with 15.2 ± 4.5 Gt/yr. The mass loss is decreasing with time at a rate of 1.1 ± 0.2 Gt/yr². R_{adj}^2 is 92%($p < 0.001$) for the quadratic model, vs 90%($p < 0.001$) for the linear, and the difference is significant at the 99.9% confidence level.

The Russian High Arctic (Figure 2.2f) has the fifth largest mass loss with 14.5 ± 6.5 Gt/yr and an acceleration in loss of 0.4 ± 0.3 Gt/yr². The quadratic R_{adj}^2 is 82%($p < 0.001$), vs 81%($p < 0.001$) for the linear, and the improvement of the quadratic fit significant at the 85% confidence level. Within the Russian High Arctic, we find a mass loss of 3.9 ± 3.6 Gt/yr for Franz Joseph Land, 8.0 ± 3.9 Gt/y for Novaya Zemlya, and 2.7 ± 3 Gt/yr for Severnaya Zemlya (Figure 2.4), and a small acceleration in loss of 0.2 ± 0.1 Gt/yr² for both Franz Joseph Land and Severnaya Zemlya.

The HMA has the sixth largest loss with 14.3 ± 12.7 Gt/yr and an acceleration in loss of 2.9 ± 0.7 Gt/yr² (Figure 1g). The R_{adj}^2 is 64%($p < 0.001$) for the quadratic model, vs 58%($p < 0.001$) for the linear, and the difference is significant at the 99.9% confidence level. We divide the HMA into four subregions defined based on their precipitation regime and their compatibility with the GRACE spatial resolution: (11a) the Tien Shan, (11b) Karakoram, Hindu Kush, Kunlun, Pamir, and Hissar Alay, (11c) Himalaya (West, Central, and East) and South and East Tibet and Hengduan Shan, and (11d) the Qilian Shan, Inner Tibet and E Kunlun (Figure S3). The largest signal comes from region 11c with a mass loss of 10.3 ± 7.4 Gt/yr and acceleration in loss of 0.6 ± 0.4 Gt/yr², followed by region 11a with a loss of 6.0 ± 4.7 Gt/yr and an acceleration in loss of 1.1 ± 0.2 Gt/yr², and region 11b with

a loss of 2.5 ± 6.3 Gt/yr and an acceleration in loss of 1.2 ± 0.4 Gt/yr². These results agree with estimates by Brun et al. [2017] for the time period 2000-2016. In region 11d, we find a mass gain of 6.4 ± 5.1 Gt/yr which is instead inconsistent with Brun et al. [2017] that finds instead a mass loss equal to -0.8 Gt/yr.

The HMA region displays a strong inter-annual variability, which explains why the R_{adj}^2 is lower than for most other regions that dominate the mass budget. The subregional analysis further indicates that the inter-annual variability and the observed acceleration in mass loss are dominated by the contribution from the western portion of the HMA, i.e. regions 11a and 11b. No such variability is visible in region 11c or 11d.

Svalbard has a mass loss of 9.0 ± 2.8 Gt/yr and an acceleration in loss of 0.9 ± 0.2 Gt/yr² (Figure 2.2h). R_{adj}^2 is 82%(p<0.001) for the quadratic model, vs 79%(p<0.001) for the linear, and the difference is significant at the 99.9% confidence level.

For the remaining small regions of Central Europe, Caucasus, Central America, North Asia, Scandinavia, Low Latitudes which represent only 6% of the total GIC area, the uncertainty in mass loss is proportionally larger using the GRACE data, but their contribution to the total mass loss of GIC is less than 2%.

We calculate the glacier mass trend and acceleration by simultaneously fitting to the glacier mass time series an annual, semiannual, linear trend, and constant for the mean mass change, and an annual, semiannual, quadratic trend, and constant for the acceleration in mass change. To compare the quadratic and linear models, we use a variant of the Akaike Information Criterion, AIC_c for use with small sample sized datasets [Burnham and Anderson, 2002] that accounts for the goodness of the fit and the number of parameters, and rigorously identifies which model best fits the data. We only report acceleration that satisfies the AIC_c criteria and is significant at the $2\text{-}\sigma$ level. For major GIC contributors and subregions, we calculate the R_{adj}^2 for both the linear and the quadratic models which provides the percent of

variance of the observed signal explained by the model. R_{adj}^2 increases only if the additional term improves the model more than would be expected by chance. To evaluate at which statistical level the improvement in the quadratic model fit is significant, we use an F-test. Finally, we also estimate the inter-annual variability of the signal in the different regions. To do so, we remove the long term trend (linear or quadratic based on the statistical test) from the 13-month smoothed time series and calculate the amplitude of the inter-annual variability.

Uncertainty in the glacier mass changes combines GRACE measurement errors, GIA and LIA errors, hydrology correction error, leakage errors, and ocean mass correction errors. The ocean mass correction is applied by processing centers prior to computing gravity field solutions using the Ocean Model for Circulation and Tides (OMCT) ocean general circulation model [Dobslaw et al., 2013] and the statistical uncertainty of the model fit. GRACE measurement errors and trends uncertainties due to the ocean mass correction are calculated following Velicogna and Wahr [2013]. GIA, LIA, and hydrology correction errors are calculated as in Jacob et al. [2012b] and Gardner et al. [2013]. To evaluate the leakage error due to assuming a uniform mass distribution within each mascon, we use a Monte Carlo approach. For each mascon we generate 10,000 synthetic monthly mass time series by distributing non-uniformly the monthly mass signal calculated applying the mascon inversion to the GRACE data, using 10,000 pseudo-random weights generated from a Gaussian distribution with standard deviation equal to 1 and zero mean. For each glacier region we calculate the differences between the trends obtained applying the mascon procedure to the GRACE data and to the synthetics. We calculate the $2\text{-}\sigma$ of the distribution of the trend differences and we define this to be the $2\text{-}\sigma$ leakage error for the trend. The total error is calculated as the sum in quadrature of the different errors (Table 2.1).

2.4 Discussion

Our GIC estimates for the common time period 2003-2009 agree within errors with Gardner et al. [2013] (Table S2), except for the Southern Andes where we use an updated inventory. Our error estimates for HMA are twice lower than in Gardner et al. [2013] because we use updated hydrological corrections (Table S2). Our mass loss estimates are higher than Rietbroek et al. [2016] for the period 2002-2014. While the authors find that their 2002-2014 results agree with Jacob et al. [2012b] for a different period, 2003-2010, we find this to be inconsistent with an increase in mass loss after 2010. Similarly, our total GIC loss is lower than Reager et al. [2016] (253 ± 35 Gt/yr), but their study mixes different time periods and data sets. In HMA, they use the period 2003-2009, when the mass loss was twice larger according to our time series (Figure 2.2g, Table S2). We find higher losses in Svalbard and Russian High Arctic because the mass loss increased after 2014. For Iceland, we use Sørensen et al. [2017] LIA correction of -5.5 ± 1 Gt/yr which was not used elsewhere and yields a larger mass loss. We find higher mass losses than Schrama et al. [2014] for 2003-2013 (142.7 ± 7.8 Gt/yr), with the largest difference in Alaska, Southern Andes where we agree with other studies [Gardner et al., 2013, Reager et al., 2016].

Our longer time series enables a more robust analysis of the interannual variability in mass change and a first, statistically significant, estimation of the acceleration in mass loss of the entire GIC and individual regions for the analyzed 14.3-year period. Based on the GRACE time series, the mass loss of the GIC approximately doubles every 24 years. While this acceleration is significant, it is less than that recorded for Greenland and Antarctica estimated, respectively, at 25.4 ± 1 Gt/yr² and 10.6 ± 4 Gt/yr² for the time period 2003-2013 [Velicogna et al., 2014b]. Hence, the ice sheets in Greenland and Antarctica will continue to dominate the contribution of sea level rise from melting land ice in decades to come.

We double the duration of observations compared to Gardner et al. [2013] using the complete

GRACE record, with optimized mascons for the latest inventory. The strong inter-annual variability of the signal is more apparent in our longer time series than from shorter periods, which helps explain in part the discrepancies between earlier studies for regions such as HMA. When we estimate the mass trend over 4 to 14 years, we find that the values stabilize after 10-11 years, for almost all regions, i.e. the uncertainty in mass trend reduces significantly over time periods greater than 11 years.

Both the mean loss and acceleration provide a more complete summary of the GIC mass balance. Four of the seven largest contributors (CAA, HMA, Russian High Arctic, and Svalbard) display a statistically significant increase in mass loss with time. HMA displays the largest inter-annual variability in the signal, which limits the detection of long-term trends from shorter-time period records, and explains why the HMA estimates over various periods have varied by more than a factor 2.

The largest acceleration in mass loss ($3.5 \pm 0.6 \text{ Gt/yr}^2$) is from the CAA with $2.2 \pm 0.4 \text{ Gt/yr}^2$ from the Arctic Canada North and $1.3 \pm 0.3 \text{ Gt/yr}^2$ from the Arctic Canada South. While the CAA exhibits a strong inter-annual variability in mass balance of $\pm 75 \text{ Gt}$ during the 14.3 year period, this signal does not affect our ability to detect a long term trend and acceleration. The mass loss increased after 2005 due to an increase in runoff [Lenaerts et al., 2013]. Regional mean summer temperature over the CAA for the period 2002-2016 based on monthly observations by the Climate Research Unit Time Series version 4.01 (CRU-TS) [Harris et al., 2014] indicate that the increase in mass loss after 2005 was associated with summer temperatures above the 2002-2016 average. We find that 8 years after 2005 (2007-2012, 2015-2016) have a mean temperature above the 2002-2016 mean, hence indicating that the warming has continued up to present. These trends are reflected in the GRACE data, including a pause in mass loss in 2013-2014 during two cold summers [Tedesco et al., 2015, Millan et al., 2017].

In the Russian High Arctic, Moholdt et al. [2012] used altimetry data for the time period

2003-2009 to report a total loss of 9.1 Gt/yr, with 0.9 Gt/yr for Franz Joseph Land (10% of the total loss), 7.6 Gt/yr for Novaya Zemlya (80%), and 1.3 Gt/yr for Severnaya Zemlya (10%). We find a higher loss 14.5 ± 6.5 Gt/yr for the longer period, more balanced between regions: 3.9 ± 3.6 Gt/yr for Franz Joseph Land (26% of the total loss, 4 times higher), 8.0 ± 3.9 Gt/yr for Novaya Zemlya (55%), and 2.7 ± 2.7 Gt/yr for Severnaya Zemlya (19%, 2 times higher). Melkonian et al. [2016] reported that the mass loss for Novaya Zemlya in 2012-2014 (8.8 ± 2 Gt/yr) was significantly higher than the mass loss in the last 65 yr (0.5 Gt/yr). They attributed the increase in mass loss in 2012-2014 to enhanced glacier runoff from warmer air temperatures [Zhao et al., 2014] and enhanced thinning of marine terminating glaciers due to enhanced flow and calving speed [Carr et al., 2017, Melkonian et al., 2016]. Our time series indicates that the mass loss has proceeded at similarly high rates for the entire period 2002-2016.

In Svalbard, prior studies indicated that the increase in GRACE-derived mass loss after 2010 was due to a combination of enhanced ice discharge and reduced surface mass balance [Matsuo and Heki, 2013, McMillan et al., 2014, Lang et al., 2015]. McMillan et al. [2014] reported for the marine-based sector of Austfonna, the largest ice cap in the Eurasian Arctic, an increase in glacier thinning after 2009, followed by an exceptionally high thinning after 2012, coincident with an increase in ice velocity [Dunse et al., 2015]. Record runoff levels were observed in 2013 due to warm summer air temperatures caused by a change in atmospheric circulation that brought a south-southwesterly flow over Svalbard [Lang et al., 2015]. Our results are consistent with this climatic record and indicate that the increase in runoff due to warmer summer air temperature has continued up to present. After the warm 2013 summer until Aug. 2016, we find that Svalbard lost more than 75 Gt. During 2005-2010, there was a long pause in surface mass balance [Lang et al., 2015] that translates to a period of near-zero mass balance in our data. The inter-annual variability in the signal is ± 20 Gt, which is large compared to the mass loss signal.

In Iceland, we observe a small positive acceleration in mass loss of $1.1 \pm 0.2 \text{ Gt/yr}^2$ due to a slow down of the mass loss after 2011. Analysis of the mean summer temperature over Iceland for the period 2002-2016 using monthly CRU-TS temperature observations [Harris et al., 2014] show that the decrease in mass loss during 2011-2016 is associated with summer temperatures below average: mean summer temperature for four of the five years (2011-2013, and 2015-2016) is below the 2002-2011 mean, consistent with Foresta et al. [2016]. Previous studies highlighted the high inter-annual variability of the icelandic mass change [Björnsson et al., 2013], which reflects its high sensitivity to both temperature and precipitation [Björnsson et al., 2013, De Woul and Hock, 2005, Aðalgeirsdóttir et al., 2006]. In 2010, we observe an abrupt drop in mass of $30 \pm 10 \text{ Gt}$, which matches in time and magnitude with the large melt event caused by the Eyjafjallajökull eruption, which had been estimated at 25 Gt by [Björnsson et al., 2013]. After 2010, the mass loss decreases significantly. The interannual variability over Iceland is $\pm 20 \text{ Gt}$, similar to Svalbard and the Russian High Arctic, but not in phase with them after 2005. This signal reflects the complex spatial variability in Arctic climate during the analyzed time period that has been attributed to the alternation of positive and negative phases of the Arctic Oscillation and North Atlantic Oscillation [Matsuo and Heki, 2013].

HMA, with a glacier area of $97,606 \text{ km}^2$ and the largest ice covered region outside the Arctic, exhibited no acceleration during the time period 2003-2009 [Gardner et al., 2013]. Our inferred acceleration in loss of $2.9 \pm 0.7 \text{ Gt/yr}^2$ for 2002-2016 is almost entirely (80%) from regions 11a and 11b, whereas region 11c controls the majority of the net loss ($10.3 \pm 7.4 \text{ Gt/yr}$) and displays only a small increase in mass loss ($0.6 \pm 0.4 \text{ Gt/yr}^2$). The acceleration in mass loss in regions 11a and 11b is driven by a large inter-annual variability in mass, which is more apparent in the longer GRACE record after year 2009 (Figure 2.5). Regions 11a and 11b are strongly affected by the westerlies according to [Yao et al., 2012, Zhan et al., 2017], whereas the high Arctic which is more significantly affected by the seasonal variability. The inter-annual variability in glacier mass loss of HMA has been linked to changes in

precipitation [Pohl et al., 2015, Wang et al., 2017]. These fluctuations are manifest in the GRACE record as changes in mass of the order of ± 60 Gt, which is considerably larger than the mean loss of ice over HMA. This variability come entirely from the western regions 11a and 11b (Figure 2.5b-c) with ± 20 Gt and ± 40 Gt, respectively. The mass increase in 2005 in region 11b agrees with Wang et al. [2017] who indicate a mass gain in the Pamir, especially in the Hindu Kush, with a peak precipitation in 2005. Pohl et al. [2015] reports an increase in precipitation in 2005, a decrease in 2008, and an increase in 2010, which are visible in our time series of mass balance as periods of lower loss and even small mass gain around 2010 (Figure 2.5). We conclude that for both region 11a and region 11b, the inter-annual variability of the glacier signal is dominated by changes in precipitation.

In the Southern Andes, our uncertainty in mass loss is higher than in Gardner et al. [2013] over the same period because we use a region $2,800 \text{ km}^2$ larger. The Southern Andes mass loss is dominated by the Patagonia icefields, not by the glaciers in the northern Andes or the Cordillera Darwin in the south, which was not known previously because these regions were lumped together or simply omitted. We attribute the inter-annual variability in the signal, about ± 40 Gt, to temporal variations in snowfall accumulation [Mouginot and Rignot, 2015].

Outside of the main seven regions (CAA, Alaska, Svalbard, Iceland, Russian High Arctic, HMA, Southern Andes), the total ice covered area of $26,500 \text{ km}^2$, or 5% of the total GIC area, does not contribute significantly ($5.2 \pm 17 \text{ Gt/yr}$) to the total loss of the GIC ($209.7 \pm 39.0 \text{ Gt/yr}$) (Table 2.1). Our uncertainty in mass loss is comparatively higher in these small regions than in the large regions, but it is unlikely that their total contribution could be much larger than estimated herein because our errors are conservative.

Several studies have indicated that the mass balance of major regions of the GIC is dominated by surface mass balance processes [Larsen et al., 2015, Millan et al., 2017], with only a small contribution from ice discharge, except for Svalbard and the Russian Archipelagos [Matsuo and Heki, 2013, McMillan et al., 2014, Lang et al., 2015, Dunse et al., 2015, Carr et al.,

2017, Melkonian et al., 2016]. This dominance expresses that ice dynamics from marine-terminating glaciers does not play a major role in the total loss. As a consequence, the time series of regional mass balance of the GIC, as presented herein, are directly useful for evaluating surface mass balance products from regional atmospheric climate models, e.g. reconstructions of runoff and precipitation. Changes in surface mass balance reflect changes in atmospheric circulation, moisture flux, and air temperature at the regional level. In a few localized areas, the ice dynamics signal may be important, but this signal could eventually be removed using independent estimates, e.g. Svalbard, CAA or Alaska, if needed at all. Hence, the GRACE time series provide a unique opportunity to evaluate climate models over a range of latitude and climatic regimes, for instance across the Arctic. We highlighted in our discussions a number of inter-annual variations that are directly related to fluctuations in precipitation and temperature. The GIC record provides a unique opportunity to test the phasing and magnitude of the changes in precipitation and melt reconstructed by these models, which for the most part are still in development for the GIC.

The coverage of the GIC will be extended with the launch of GRACE follow-on in early 2018. The GRACE follow-on record will provide improved data quality compared to GRACE. The data gap between August 2016 and the GRACE follow-on data could be filled using reconstructions of surface mass balance from regional atmospheric climate models. A longer record of GRACE data will be useful to evaluate these models in regions with a strong inter-annual variability, e.g. HMA and the Arctic.

2.5 Conclusions

We employ the latest glacier inventories, improved hydrological corrections, complete time series, and optimized mascons minimizing leakage errors to extend the mass budget of the World's Glaciers and Ice Caps (GIC) and nearly halve the uncertainties using a time series of

time-variable gravity data for the entire GRACE mission. Due to lower errors and a longer record, we unambiguously detect an acceleration in mass loss of several major regions and for the entire GIC. We find that seven regions, five in the Arctic, dominate the mass loss from GIC. The largest contributors to sea level rise are the CAA, followed by Alaska, Patagonia, Iceland, Russian High Arctic, and HMA. The acceleration in mass loss is dominated by the CAA, HMA, Svalbard, and the Russian High Arctic. The total acceleration of the GIC mass loss is sufficient to double the mass loss every 24 years. Over one century, from 2000 to 2100, the mass loss of the GIC would cumulate to 13.2 ± 3.5 cm if the acceleration in mass loss were to continue. Several regions are affected by a significant inter-annual variability which implies that assessments of acceleration in mass loss must be conducted using a rigorous statistical test using the longest possible time series, at least longer than 11 years. This inter-annual variability of the GRACE signal however contains invaluable information about the local climatology that will enable a detailed and quantitative evaluation of regional and global atmospheric climate models over large areas in follow-on studies.

Glacier Region	Mass Balance [Gt/yr]	Acceleration [Gt/yr ²]	$R_{adj}^2(L)$	$R_{adj}^2(Q)$	F-test	AIC_c Q/L
1. Alaska	-57.1 ± 10.5	–	92	92	L at 99	L
2. Western CanadaUS	-1.3 ± 13.1	–	32	32	L at 99	L
3. Canadian Arctic Archipelago	-68.1 ± 9.7	-3.5 ± 0.6	95	97	Q at 99	Q
3a. Arctic Canada North	-36.8 ± 6.7	-2.2 ± 0.4	93	95	Q at 99	Q
3b. Arctic Canada South	-31.3 ± 6.1	-1.3 ± 0.3	93	95	Q at 99	Q
4. Iceland	-15.2 ± 4.5	1.1 ± 0.2	90	92	Q at 99	Q
5. Svalbard	-9.0 ± 2.8	-0.9 ± 0.2	79	82	Q at 99	Q
6. Scandinavia	1.6 ± 5.1	–	17	17	L at 99	L
7. Russian High Arctic	-14.5 ± 6.5	-0.4 ± 0.3	81	82	Q at 85	Q
7a. Franz Joseph Land	-3.9 ± 3.6	-0.2 ± 0.1	65	66	Q at 77	Q
7b. Novaya Zemlya	-8.0 ± 3.9	–	80	80	L at 99	L
7c. Severnaya Zemlya	-2.7 ± 2.7	-0.2 ± 0.1	59	60	Q at 95	Q
8. North Asia	4.3 ± 13.0	–	10	10	L at 99	L
9. Central Europe	-1.6 ± 4.4	–	25	25	L at 99	L
10. Caucasus Middle East	2.5 ± 4.7	–	20	20	L at 99	L
11. High Mountains Asia	-14.3 ± 12.7	-2.9 ± 0.7	58	64	Q at 99	Q
11a. E and W Tien Shan	-6.0 ± 4.7	-1.1 ± 0.2	57	63	Q at 99	Q
11b. Hindu Kush, Karakoram, W Kunlun, Pamir, Hissar Alay	-2.5 ± 6.3	-1.2 ± 0.4	43	46	Q at 99	Q
11c. Himalaya, Hengduan Shan S and E Tibet	-10.3 ± 7.4	-0.6 ± 0.4	62	63	Q at 89	Q
11d. E Kunlun, Inner Tibet and Qilian Shan	6.4 ± 5.1	–	55	55	Lat99	L
12. Low Latitudes	-1.3 ± 8.7	–	10	10	L at 99	L
13. Southern Andes	-35.1 ± 19.2	–	68	68	Lat99	L
13a. Northern and Southern Patagonia Ice Fields	-26.7 ± 7.4	–	92	92	Lat99	L
14. New Zealand	-1.0 ± 4.2	–	63	63	Lat99	L
Total	-209.7 ± 39.0	-6.7 ± 2.5	95	97	Q at 99.9	Q

Table 2.1: Longterm mass balance and acceleration calculated between April 2002 and August 2016. AIC_c indicates the model that best fits the signal based on the Akaike Information Criterion: L indicates linear model and Q quadratic model. $R_{adj}^2(L)$ and $R_{adj}^2(Q)$ are R-squared adjusted for linear (L) and quadratic (Q) model respectively, F-test indicates at which statistical level the improvement in the quadratic model fit is significant. Accelerations are reported only when the quadratic model provides the best fit to the regional time series according to the AIC_c criteria and the acceleration is statistically significant; otherwise a linear fit is used.

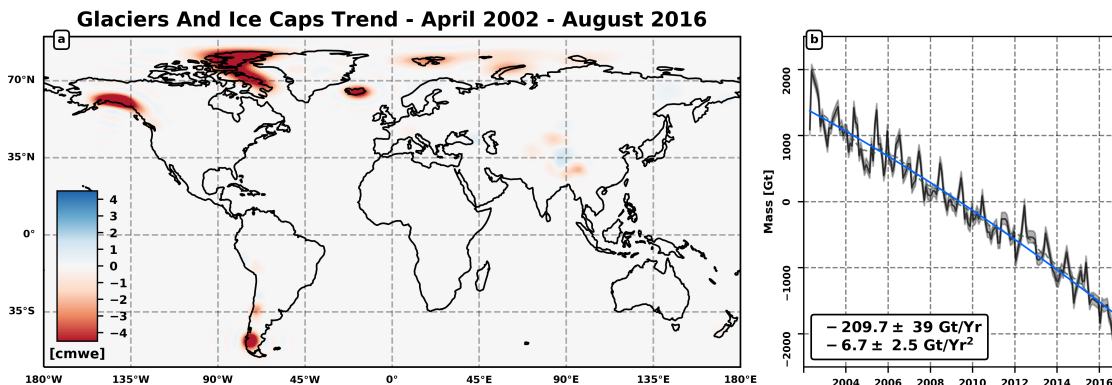


Figure 2.1: (a) Glaciers and Ice Caps (GIC) mass change derived from GRACE for April 2002 to August 2016, in centimeter of water. (b) GRACE-derived ice mass time series for the GIC, with the best-fit quadratic trend (blue) line, with mean loss and acceleration in mass loss in Gt = 10^{12} kg per year, and monthly errors (light blue).

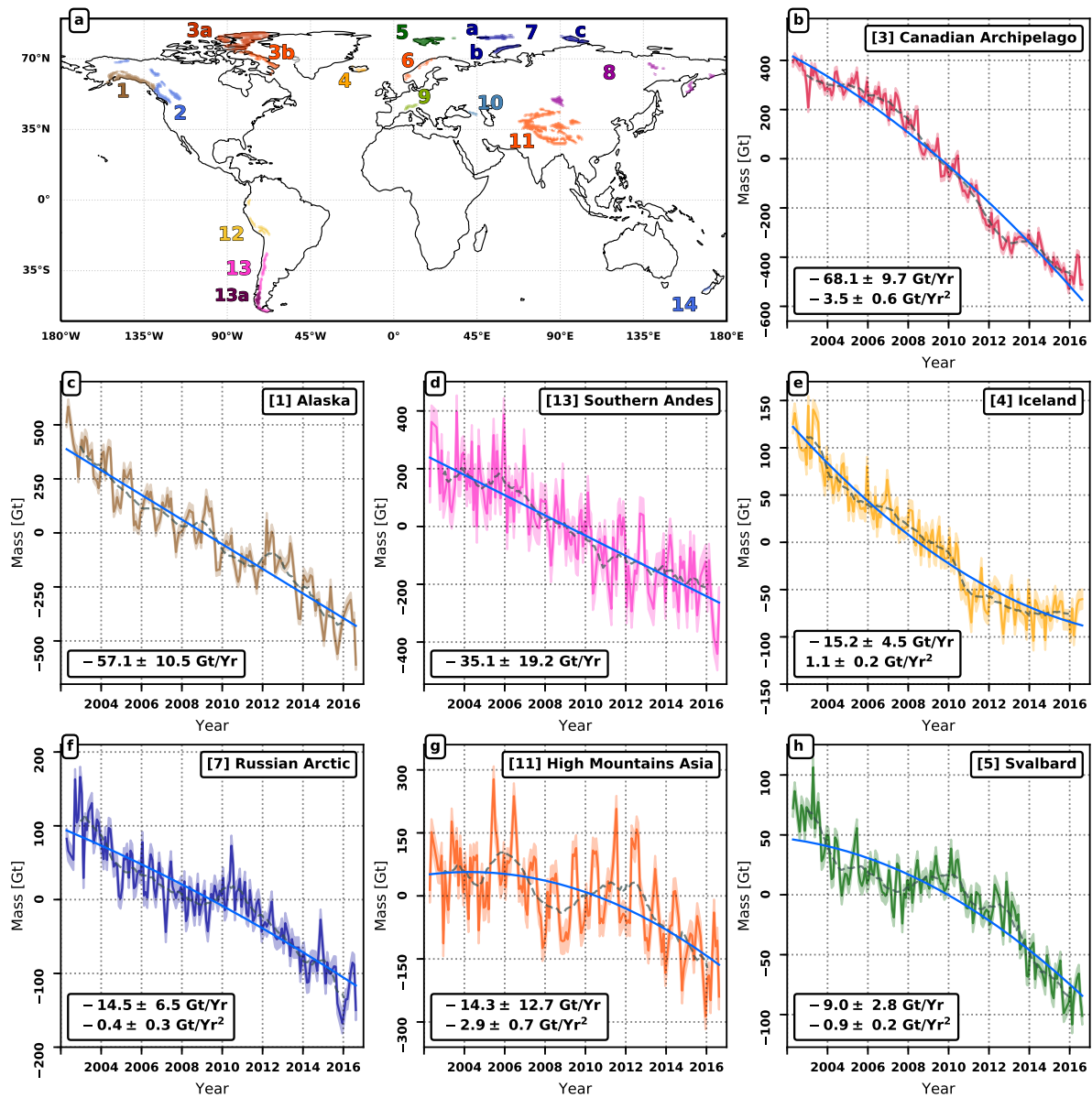


Figure 2.2: (a) Glaciers and Ice Caps locations from the Randolph Version 6.0 inventory divided into 13 regions and subregions. GRACE-derived ice mass time series for the time period April 2002 - August 2016 are shown for (b) Canadian Archipelago, (c) Alaska, (d) the Southern Andes, (e) Iceland, (f) the Russian High Arctic, (g) High Mountain Asia, and (h) Svalbard in decreasing mass loss values. Data filtered for the seasonal dependence using a 13-month window are shown (gray dashed line). The blue line represents the best-fit linear or quadratic trend. Light color bands are monthly errors.

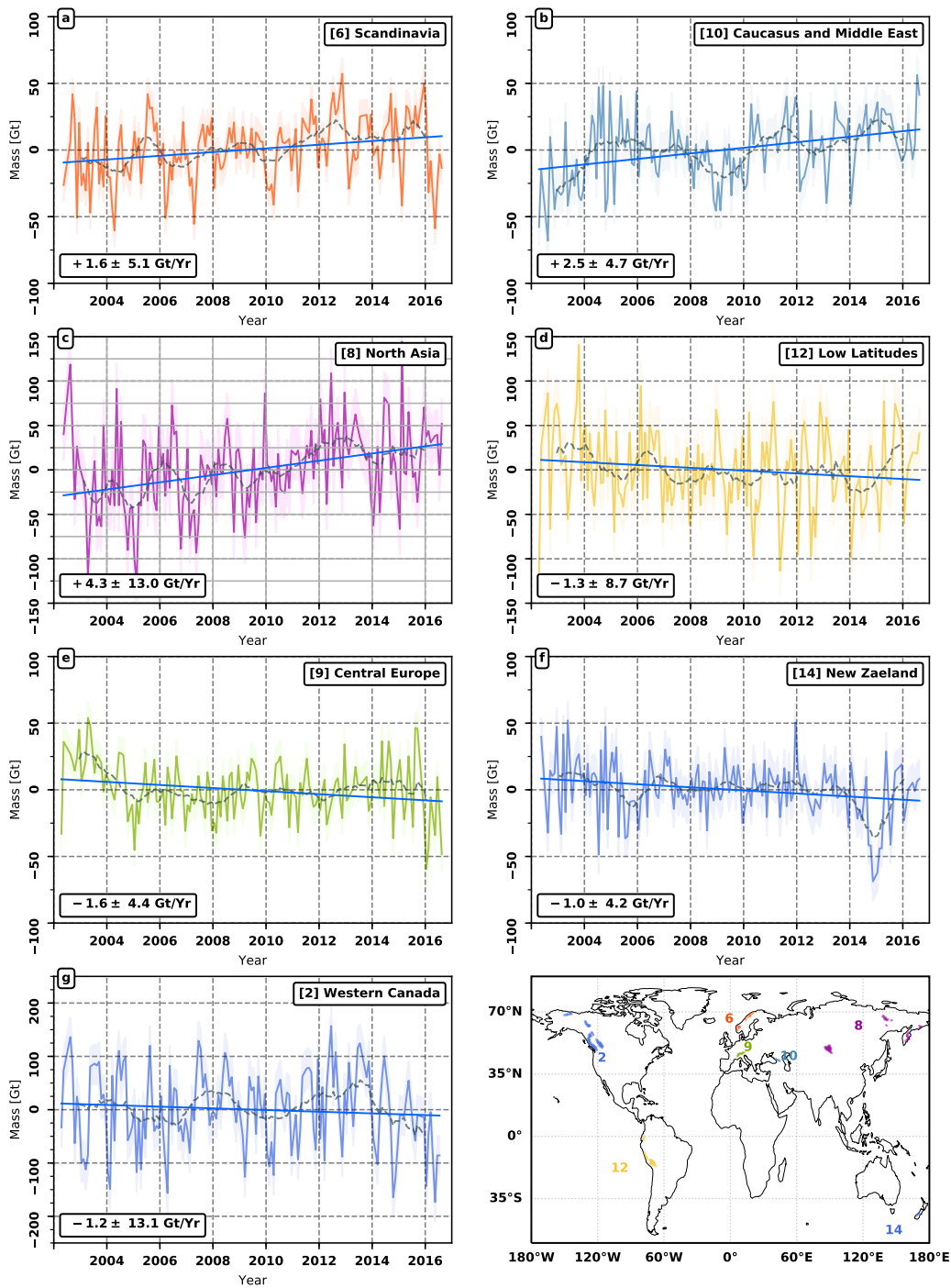


Figure 2.3: Ice mass time series, in gigatonnes (Gt): (a) Scandinavia, (b) Caucasus and Middle East, (c) North Asia, (d) Low Latitudes, (e) Central Europe, (f) New Zealand, and (g) Western Canada. Data filtered for the seasonal dependence using a 13-month window are shown (gray dashed line). The blue line represents the best-fit linear or quadratic trend to the time series. Light color band are monthly errors. Included are GRACE linear and quadratic trend. (h) location of the ice covered regions according to the Randolph Glacier Inventory.

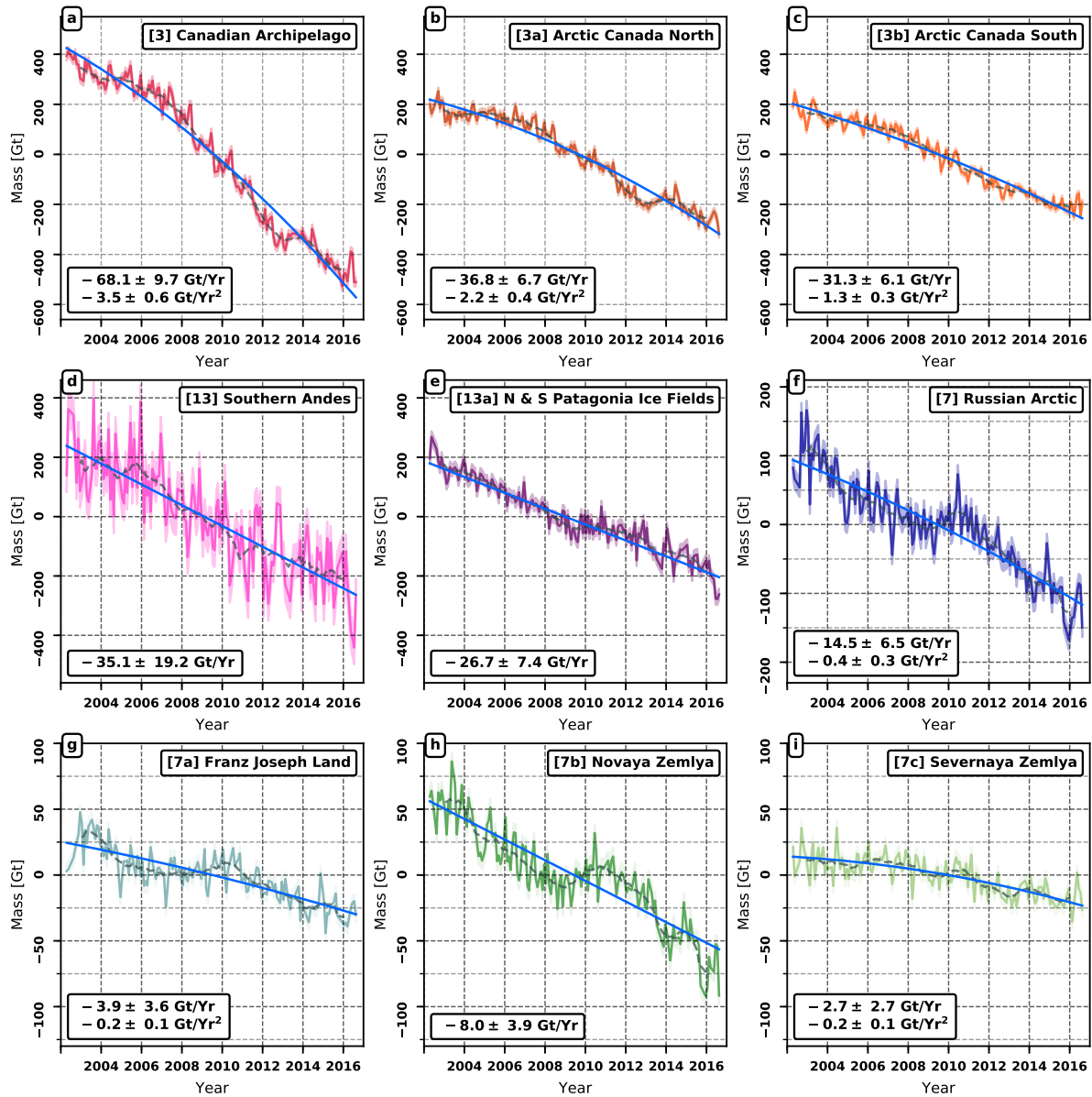


Figure 2.4: Ice mass time series, in gigatons (10^{12} kg) for: (a) Canadian Arctic Archipelago, (b) Arctic Canada North, (c) Arctic Canada South, (d) Southern Andes, (e) North and South Patagonia Ice Fields, (f) Russian High Arctic, (g) Franz Joseph Land, (h) Novaya Zemlya, and (i) Severnaya Zemlya. Data filtered for the seasonal dependence using a 13-month window are shown (gray dashed line). The blue line represents the best-fit linear or quadratic trend to the time series. Light color band are monthly errors. Included are GRACE linear and quadratic trend estimates.

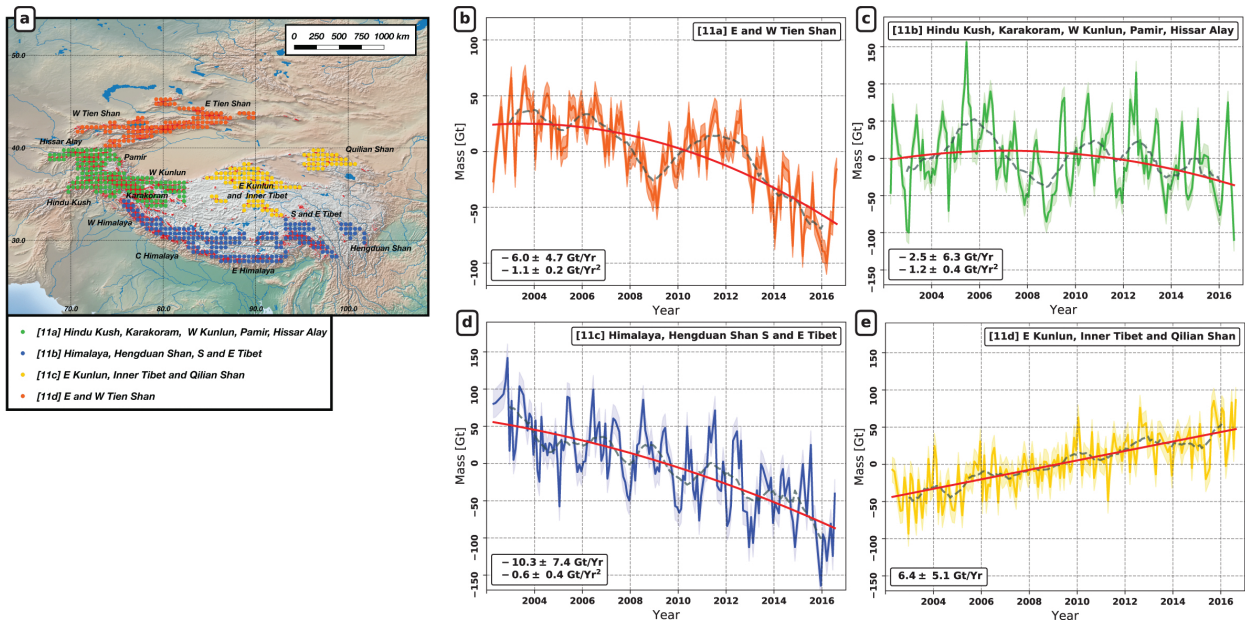


Figure 2.5: Ice mass time series for High Mountain Asia (HMA) from GRACE data for the time period April 2002 to March 2016. The distribution of mascons is shown for (b) region 11a (E and W Tien Shan), (c) region 11b (Karakoram, Hindu Kush, W Kunlun, Pamir, and Hissar Alay), (d) region 11c (Himalaya, Hengduan Shan S and E Tibet) and (e) region 11d (Qilian Shan, Inner Tibet and E Kunlun). Data filtered for the seasonal dependence using a 13-month window are shown (gray dashed line). The red line represents represents the best-fit linear or quadratic trend to the time series. Light color band are monthly errors. Included are GRACE linear and quadratic trend estimates.

Chapter 3

Mass Balance of the Novaya Zemlya Archipelago between 2002 and 2017

We evaluate the mass balance of the Novaya Zemlya Archipelago between April 2002 and August 2016 employing independent estimates obtained using time-variable gravity from the NASA/DLR GRACE mission and satellite altimetry data from the NASA ICESat and the ESA CryoSat-2 missions. We present two new algorithms designed to derive ice elevation change maps using altimetry data and we compare their performance over the region of interest. Gravimetric and Altimetric observations provide consistent results and show that over the period under analysis, glaciers in the region have lost mass at a rate of -8 ± 4 Gt/yr corresponding to a sea level contribution of 0.021 mm/yr. The negative trend increased after 2010, reaching a maximum rate of -14.3 ± 4 Gt/yr between 2010 and 2016. The increased mass loss was associated with high thinning rates at low elevations (below 500 m), with marine-terminating glaciers thinning significantly faster than those terminating on land. The mass loss process was associated to a shift in climatic conditions in the region due to enhanced atmospheric and ocean temperatures and decreased sea ice concentrations. These results indicate that glaciers in the region are sensitive to variations of both climatic

mass balance and ice discharge.

3.1 Introduction

This study focuses on the glaciers of the Novaya Zemlya Archipelago (NZEM), located in the Russian High Arctic (RHA). The RHA lost ice mass at a rate -10 ± 5 Gt/yr between 2002 and 2014, with more than 80% of the mass wastage attributed to the glaciers of NZEM [Reager et al., 2016, Moholdt et al., 2012, Jacob et al., 2012b]. Recent studies have highlighted that both negative surface mass balance (SMB) and accelerating ice dynamics (D) resulted in an increasing glacier mass loss in the region after the year 2000 [Melkonian et al., 2016, Carr et al., 2017, Strozzi et al., 2017]. These results diverge from what has been observed in other Arctic regions like the Canadian Arctic Archipelago [Gardner et al., 2011, Lenaerts et al., 2013, Van Wychen et al., 2014, Millan et al., 2017] and Alaska [Larsen et al., 2015], where negative SMB has been indicated as the main process driving regional glacier mass loss. Nonetheless, a definitive assessment of the relative weight of the two components in the NZEM total glacier mass balance is not yet available. Atmospheric temperatures will continue to rise in the course of the next century [Vaughan et al., 2013] and available model projections indicate the RHA as one of the major sources of SLR for the 21st century, losing almost the 50% of its total volume corresponding to a value between 20 ± 8 and 28 ± 8 mm of SLR by 2100 [Radić et al., 2014, Kotlyakov et al., 2010], thus suggesting that the regional mass loss will significantly increase in the coming decades. However, model projections are based on surface mass balance simulations that, neglecting glacier dynamics and calving fluxes, may underestimate the future glacier mass loss. Additional observations, therefore, are necessary in order to gain a better understanding of the physical processes driving ice mass change in the region and to produce more reliable forecasts of future glacier evolution and contribution to sea level rise. In this study we evaluate the mass balance of NZEM

glaciers employing time series of time-variable gravity from the NASA/DLR GRACE mission between April 2002 and August 2016. We compare results from GRACE with independent estimates obtained using satellite altimetry data from the NASA ICESat mission between October 2003 October 2009 and the ESA CryoSat-2 mission between July 2010 and July 2016. We compare results from two algorithms designed in order to generate maps of ice elevation/volume change employing CryoSat-2 elevation data with the aim of optimizing the spatial coverage of elevation change measurements and minimizing the effect of seasonal biases due to temporal variations of surface and subsurface scattering properties in the elevation change retrieval. We calculate regional mean elevation change time series with CryoSat-2 and compare them with glacier mass change time series obtained using GRACE for the overlapping time period. We examine the inter-annual variability present in the mass change and elevation change time series and compare them with available climatic data (Total Precipitation, Atmospheric Temperature, Sea Surface Temperature and Sea Ice Concentration) in order to gain further insight into the processes driving the glacier mass loss. Finally, we assess the impact of coast and terminus type in glacier thinning rates in order to investigate the role of different climatic and oceanic forcings on glacier elevation change.

3.1.1 Study Region

The RHA (latitudes 53°N to 83°N, and longitude 45°E to 105°E) contains a total of 51,592 km^2 of glaciers and ice caps, corresponding to almost 13% of the total glacier area outside Greenland and Antarctica [Pfeffer et al., 2014, Rastner et al., 2017]. The total ice volume is distributed across four regions: Novaya Zemlya (NZEM), Severnaya Zemlya (SZEM), Franz Josef Land (FJL), and Ushakon Island (UI). With a total glacier area of 22,379 km^2 [Rastner et al., 2017], NZEM is the region with the largest glacier coverage (Figure 3.1). NZEM lies between the Barents Sea and the Kara Sea and consists of two major islands - Severny Island

in the North-East and Yuzhny Island in the South-West - and several minor islands. Severny and Yuzhny Islands are separated by the Matochkin Strait, a 600 meters wide and 100 km long water channel that connects the Barents Sea with the Kara Sea. An axial mountain range extends over the entire length of the archipelago and reaches a maximum elevation of 1340 m.a.s.l. on Yuzhny Island and 1596 m.a.s.l. on Severny Island [Kotlyakov et al., 2010]. 25% of the total land area ($82,000 \text{ km}^2$) is covered by ice, while the remaining land has a cover of tundra vegetation consisting of mosses, lichens, and shrubs [Zeeberg, 2001, Serebryanny and Malyasova, 1998]. 92% of the total glacier area ($20,784.4 \text{ km}^2$) is located on Severny Island and concentrated in a single large ice cap (Northern Icefield) that covers 45% of the island area and constitutes the second largest body of ice in the Eurasian Continent after Austfonna (Svalbard) [Grosval'd and Kotlyakov, 1969]. The Northern Icefield has a length of more than 400 km along the North-South ridge and a mean East-West extension of 80 km [Rastner et al., 2017]. The ice cap has an average elevation of 800 meters and a thickness ranging between 400 and 450 meters [Grosval'd and Kotlyakov, 1969]. 71% of the Northern Icefield area ($16,064 \text{ km}^2$) is composed by marine-terminating glaciers while most of the glaciers separated from the main ice cap terminate on land. Glaciers in the region were classified in the past as cold-based [Zeeberg et al., 2003]; however, recent studies suggest a widespread change in regional glacier thermal regime and a transition to predominantly warm-based/polythermal condition [Kotlyakov et al., 2010, Grant et al., 2009]. The climate in the region is one of the most severe on the planet and is determined by a complex interaction between multiple oceanic and atmospheric forcings. On the North-West, mild temperatures are favored by the advection of warm and salty water transported by the North Cape current from the Atlantic Ocean [Zeeberg, 2001, Venegas and Mysak, 2000, Dickson et al., 2000]. Abundant annual precipitation $\sim 400 \text{ mm/yr}$ is favored by the influx of air masses rich in moisture by the Atlantic Cyclone [Zeeberg, 2001, Dickson et al., 2000]. Atmospheric conditions become gradually drier and colder toward the South-East: the central mountain chain provides an orographic barrier for the eastward penetration of the Atlantic

cyclonic system [Zeeberg, 2001] and precipitation gradually decreases toward South. On the Kara Sea coast, annual precipitation amounts to ~ 250 mm/yr. Here, lower atmospheric temperatures, especially in winter and spring, are determined by mostly permanent sea ice and dominance of cold Arctic water [Zeeberg, 2001]. January and February are typically the coldest months of the year with minimum air temperatures decreasing from the North-West (-15°C) to the South-East (-21°C). Maximum temperatures ($+2^{\circ}\text{C}$) are registered in August but are not significantly different between the two coasts. Maximum precipitation is measured between September and October, while the end of the spring season, between April and May, is the driest period of the year.

3.1.2 Mass Balance of NZEM during the 20th Century

Novaya Zemlya's present-day average temperatures are about 3° higher than during the nineteenth century [Przybylak and Wyszynski, 2016]. A progressive atmospheric warming throughout the first decades of the twentieth century contributed to the beginning of a long phase of glacier's shrinkage [Zeeberg and Forman, 2001], during which the glaciers in the region lost mass with an average rate between 0.16 and 0.30 m we/yr [Dowdeswell et al., 1997, Kotlyakov et al., 2010, Melkonian et al., 2016, Williams and Ferrigno, 2010, Sharov et al., 2009]. The process was not uniform in time, but consisted of a first phase (1920s-1960s) with extremely fast recession (Zeeberg and Forman [2001] observed retreat rates > 300 m/yr, and maximum cumulative retreat of between 2 and 14 km), followed by a second phase (1960s-1990s) characterized by less negative mass balance and lower retreat rates (50 to 150 m/yr) [Zeeberg and Forman, 2001, Kotlyakov et al., 2010]. Zeeberg and Forman [2001] observed that the decadal variability of glacier mass balance on Novaya Zemlya is strongly linked to long-term shifting of atmospheric and oceanic circulation patterns related to the North Atlantic Oscillation. The North Atlantic Oscillation (NAO) is a fluctuation in atmospheric conditions in the Atlantic Ocean related to difference in sea-level pressure between the Icelandic low

(Subpolar Low) and the (Subtropical High) Azores High that controls the strength and direction of Westerlies and location of storm tracks across the North Atlantic [Hurrell, 1996]. During a positive phase of the NAO, sea-level pressure at high latitudes is below normal, while above normal conditions are registered at mid-latitudes. An increased pressure gradient over the North Atlantic contributes to an intensified and more zonally oriented jet-stream. When the NAO is in a negative phase, a decreased pressure gradient between high and mid-latitudes weakens the jet-stream that becomes more meridionally oriented [Hurrell, 1996]. When the NAO is in a prolonged positive phase, the straightening of the polar vortex contributes to an increased flux of air masses from the Atlantic Ocean resulting in elevated winter precipitation over NZEM. A stronger North Atlantic pressure gradient intensifies the advection of warm water from the Atlantic into the Barents Sea [Zeeberg and Forman, 2001]. The Atlantic water releases heat into the atmosphere and determines warmer than normal winter and summer temperatures. On the other hand, during extended negative NAO phases, instead, the jet stream weakens and atmospheric conditions in the region become drier and colder. Between the 1920s and 1950s the NAO was in a predominantly positive phase and higher than normal atmospheric and ocean temperatures favored fast glacier recession and negative mass balance. After 1960, the NAO turned to a mostly negative phase in which colder atmospheric conditions and lower ocean temperatures contributed to slowing down the long-term glacier retreat [Zeeberg and Forman, 2001]. Several studies have documented the status of Novaya Zemlya glaciers since 1990 and shown that the archipelago is still undergoing a consistent negative mass balance [Reager et al., 2016, Kotlyakov et al., 2010, Moholdt et al., 2012, Pelto, 2016]. However, they differ on the importance of ice discharge as a driver of the total ice mass loss. Moholdt et al. [2012] used satellite laser altimetry by ICESat and satellite gravimetry by GRACE to study the mass balance of NZEM between October 2003 and October 2009. They estimated a glacier mass loss ranging from -7.6 ± 1.2 to -5.8 ± 3.0 Gt/year associated with rapid glacier thinning at elevations below 500 meters. The analysis of elevation change data showed no significant difference between frontal thinning

of marine- and land-terminating glaciers (-0.94 vs -0.89 m/yr). Significant difference was instead found between glacier thinning rates on the north-west (Barents Sea) (-0.45 m/yr) and those located on the south-east (Kara Sea) (-0.25 m/yr). According to the authors, these results are in line with what was observed in other Arctic regions such the Canadian Arctic Archipelago and Alaska, where glacier dynamics had limited impact on glacier mass loss during the last decades [Gardner et al., 2011, Lenaerts et al., 2013, Van Wychen et al., 2014, Millan et al., 2017]. Zhao et al. [2014] used multiple active and passive microwave sensors to study glacier surface melt dynamics throughout NZEM between 1995 and 2011. They found a progressive increase in melt season length (Total Melt Days) consistent with increased atmospheric temperatures and decreased late summer sea ice coverage over both the Barents and the Kara Sea. These results confirmed that increased snowmelt and summer runoff contributed to the high ice thinning rates observed by Moholdt et al. [2012]. On the other hand, recent studies presented new evidence suggesting that increased ice discharge by marine terminating glaciers played a non negligible role in the recent ice mass loss [Carr et al., 2013, Pelto, 2016, Carr et al., 2017, Melkonian et al., 2016]. Carr et al. [2017] documented NZEM glacier retreat between 1973 and 2015, observing significant recession for both marine- and land-terminating glaciers. Marine-terminating glaciers retreated on average 3.5 faster than land-terminating glaciers (46.9 vs 13.8 m/yr) with marine glaciers on the Barents Sea retreating on average significantly faster than on the Kara sea (55.9 vs 37.2 m/yr). Glacier recession accelerated after the year 2000 on the Barents Sea and after 2003 on the Kara Sea [Carr et al., 2013, Pelto, 2016] with marine glaciers reaching maximum retreat rates of 85.4 m/yr for the Barents Sea and 64.8 m/yr for the Kara Sea [Carr et al., 2017]. The exceptional retreat observed after 2000 coincided with significantly warmer atmospheric and ocean temperatures and lower sea ice concentrations with respect to the previous 27 years [Carr et al., 2017]. These results were validated by Melkonian et al. [2016], which mapped velocity (between 1999 and 2014) and elevation change (between 1952 and 2013/2014) of the major outlet glaciers of NZEM. Consistent with the high retreat rate observed by Carr

et al. [2013, 2017], the highest ice speeds and thinning rates were measured at the front of marine-terminating glaciers facing the Barents Sea. Melkonian et al. [2016] also presented evidence of a recent acceleration in ice velocity and ice thinning rates after the year 2000. Steady increase in marine-terminating glaciers velocities were also observed by Sun et al. [2017] between 2002 and 2015 and by Strozzi et al. [2017] between 2008 and 2016. All these findings indicate an increasingly negative regional glacier mass balance after the year 2000. In this paper we address the following science questions:

- Do GRACE and CryoSat-2 provide consistent estimates of glacier mass balance in the region?
- Can we use the elevation change estimates from CryoSat-2 in order to evaluate differences in thinning dynamics between marine- and land-terminating glaciers between 2010 and 2016?
- Does the comparison of mass change time series from GRACE and CryoSat-2 with climatic data improve our understanding of the physical processes driving the regional glacier mass loss? (Is the glacier mass balance in the region driven by surface mass balance or by ice discharge? What is the effect of variable atmospheric and oceanic conditions on the glacier mass loss?)
- Is the mass loss between 2010 and 2016 higher than between 2002 and 2009? Is the regional ice mass loss constant or accelerating with time?

3.2 Data and Methods

3.2.1 Time Variable Gravity and Mascon Inversion

We derive region time series of glacier mass balance using the least squares fit mascon approach presented in Chapter 2. We investigate the presence of long-term trends in glacier mass balance by fitting to the regional time series a model function composed by an annual, a semiannual signal, a linear trend, and a constant component. We add a quadratic term to the model function to investigate the presence of acceleration in mass loss during the period under study. We investigate the inter-annual variability of the glacier mass anomaly by smoothing the regional time series employing a 13-month moving average filter [Velicogna, 2009]. We define a glaciological year as the time period separating two consecutive ablation seasons, i.e. the 1st September in year n and 31st August in year $n+1$. We calculate the regional glacier annual mass balance as the difference between values assumed by the 13-month smoothed time series in two consecutive Septembers (e.g. the 2004 regional glacier mass balance is calculated as the difference between the value assumed by the smoothed mass anomaly in September 2004 and September 2003).

3.2.2 Satellite Altimetry

ICESat

In this study, we use level-2 Global Land Surface Altimetry HDF5 (GLAH14) release 34. The data are provided together with quality attributes and elevation corrections (range correction of the Troposphere, solid Earth Tide, ocean tide and pole tide) for each footprint. The data quality attributes include a wave saturation flag to indicate saturation of the sensor when recording the returned pulse and a correction of a potential bias in the extracted elevations

[Smith et al., 2005]. We apply the saturation, and the inter-campaign bias corrections. The Gaussian-Centroid correction has already been applied to this data release [Siegfried et al., 2011, Borsa et al., 2014]. We use glacier outlines from the sixth release of the Randolph Glacier inventory [Pfeffer et al., 2014] in order to isolate elevation measurements over the NZEM glacier area. Following Moholdt et al. [2012] and Gardner et al. [2011] we do not apply the data parameter-based cloud filtering [Smith et al., 2009], as it tends to be too strict and to discard a high number of elevation measurements that could be otherwise used to measure elevation changes. Over NZEM, the application of the data-culling procedure reduces the number of available measurements by 65%.

ICESat : Elevation Change Estimation

The application of ICESat to measure ice elevation changes over mountain glaciers and ice caps is complicated by:

- Significant loss in accuracy of elevation measurements in regions characterized by steep slopes [Brenner et al., 2007] due to increased size of laser footprint and major sensitivity to pointing errors [Gardner et al., 2011];
- Frequent laser detector saturation due to sudden changes in energy of the returning echoes caused by the high variability in scattering properties of the sampled terrain;
- Non-uniform data availability between winter and summer campaigns due to the different meteorological conditions. Especially during summer campaigns, higher atmospheric humidity and cloud coverage favor the conditions for receiver saturation (Reflection from thick clouds layers) and forward scattering (thin cloud layers) [Moholdt et al., 2010, Fricker et al., 2005, Brenner et al., 2007]. summer tracks over NZEM are in fact often discontinuous or sometimes completely missing.

The transition from a continuous to a campaign mode determined a decrease in the number of ground tracks and an increased inter-track spacing. At the latitude of NZEM we observe an inter-track spacing ranging between 20 and 30 kilometers. The large orbit spacing makes the elevation observations sparse and complicates the application of methodologies used in the past to assess the mass balance of Greenland and Antarctica with other altimetric missions. The ICESat campaign mode was characterized by a 91-day repeat orbit with a 33-day sub-cycle. However, orbits were not exactly repeated but spaced by several hundreds meters (150 meters) [Moholdt et al., 2010]. Here, we employ the along-track "plane-fit" regression technique presented by Chapter 1. The plane-fit is applied at multiple locations considering circular patches with a radius equal to 700m with centroids equally spaced along each satellite track. The spacing is chosen equal to one half the size of the plane radius (350 meters), consecutive planes are therefore partially overlapped [Moholdt et al., 2012]. In order to reduce the effect of erroneous elevation measurements on the elevation change estimates, the least squares inversion is applied iteratively at each centroid location discarding all the measurements with a residual value larger than three times the standard deviation of all the residuals. This procedure is repeated iteratively until all observations have a residual contained within the $3\text{-}\sigma$ interval [Nuth et al., 2010, McMillan et al., 2014]. In order to further reduce the effect of erroneous measurements on the final regional mass change estimate we consider in the following analyses only elevation change measurements derived from planes: with a total number observations equal or larger than 15; containing observations from more than 4 different sub-tracks (4 different satellite passages); containing observations distributed on a temporal interval of at least two years; with an estimated slope in the easting/northing direction lower than 10 degrees.

CryoSat-2

In this study, we employ Level-2 Baseline-C SAR Interferometry mode elevation data provided by the European Space Agency [Bouffard et al., 2017]. Given the use of radar interferometry, elevation measurements by CryoSat-2 are not aligned along the direction of flight of the satellite but, are scattered over the entire region under observation, complicating the application of the classic crossover or collinear analysis used with other altimeters. The non uniform distribution of the returning echoes introduces possible bias in the calculation of ice elevation changes. The radar Point-Of-Closest-Approach (POCA) are in fact mainly located at higher elevations while depressions and low elevation regions are in general under-sampled [Gray et al., 2015]. Elevation data are distributed together with latitude, longitude, measurement acquisition time, geophysical and tidal corrections applied in the Level-2 processing, and several quality flags. In the case of CryoSat-2 case, we locate elevation measurements over ice using the recently released glacier inventory by Rastner et al. [2017].

CryoSat-2 : Elevation Change Estimation

In the present section, we describe the two methodologies used to evaluate/estimate ice elevation changes over NZEM using CryoSat-2 elevation data.

CryoSat-2 Method-1 (CryoSat-2-M1): Elevation changes are obtained applying the plane-fit on a regular 1 km grid covering the entire NZEM's glacier area. The grid is defined on the standard NSIDC/North Polar Stereographic Projection (EPSG: 3413). We select a 1 km resolution grid as the best trade off between the size of the radar footprint and the possible approximation of the glacier surface with a plane. An elevation change value for each grid cell is obtained considering all the measurements available within 1000 m from the cell centroid and following the same steps applied in the ICESat case. Given the larger

glacier area considered in this case, we repeat the inversion using two more model functions:

$$z(x, y, t) = \alpha_0 + \alpha_1x + \alpha_2y + \alpha_3x^2 + \alpha_4y^2 + \frac{dz}{dt}t \quad (3.1)$$

$$z(x, y, t) = \alpha_0 + \alpha_1x + \alpha_2y + \alpha_3x^2 + \alpha_4y^2 + \alpha_5xy + \frac{dz}{dt}t \quad (3.2)$$

We obtain our final estimate selecting the elevation trend value associated to the model providing the best fit to the considered elevation measurements. We use the R_{adj}^2 as a model selection criterion (i.e. we chose the dh/dt value associated with the model function characterized by the largest R_{adj}^2). Following McMillan et al. [2014] and Foresta et al. [2016], grid cells with a valid elevation change value are assigned an uncertainty value equal to the standard error associated to the linear temporal trend during the the application of the plane-fit. The standard error of the linear trend depends upon the distribution of elevation measurements accumulated within each grid cell, and provides a measure of the extent to which our prescribed model of linear elevation change through time fits these observations. This statistical measure does not formally account for all sources of uncertainty, but includes factors such as radar speckle, some error in satellite location, retracker imprecision, and non modeled atmospheric attenuation [Wingham et al., 1998, McMillan et al., 2014].

CryoSat Method-2 (CryoSat-2-M2): The second methodology used to map ice elevation changes over NZEM is based on the application of the plane-fit employing all the available elevation measurement locations as plane centroids following Wouters et al. [2015]. An elevation change value is therefore estimated for every available elevation observation. The plane-fit is applied following the same steps presented in the previous paragraph. Given a single centroid:

- We locate all the elevation observations available within a distance of 1000 meters from the plane centroid.
- We least squares fit the time variable plane function of the elevation observations. We repeat the fit iteratively until all the elevation measurements are contained within the $3\text{-}\sigma$ interval.
- We reject dh/dt values obtained by planes containing less than 15 points, with an estimated slope higher than 10 degrees, and with a temporal coverage shorter than two years.

Also in this case, we test three different plane model functions and we choose the one with the highest R_{adj}^2 to estimate the ice elevation change rate at the centroid location. In the case of ICESat and CryoSat-2-M2, before proceeding to the extrapolation phase, the measured elevation changes need to be averaged on the same 1 km grid used in the CryoSat-2-M1 case. The averaging procedure is applied as in Wouters et al. [2015] following the steps presented below:

- If the considered grid cell contains a single measurement, we assign this value to the entire grid cell and we set the cell elevation change rate uncertainty equal to 50% of the same observation (i.e. the grid cell uncertainty has the same amplitude of the elevation change signal).
- If the considered grid cell contains multiple measurements, we set its elevation change rate and uncertainty equal to the measurements mean and standard deviation. Also in this case, we use a $3\text{-}\sigma$ iterative filter in order to discard erroneous observations that could influence our final elevation change estimates.

3.2.3 Noise Reduction - Local Regression Filter

Before proceeding to the extrapolation phase, we apply a noise reduction procedure in order to reduce the effect of non realistic dh/dt values on our final estimates. For every grid cell with a valid dh/dt value, we find all the dh/dt estimates located at a distance smaller than or equal to the search radius distance that we set equal to 25 km. We use linear regression to find the quadratic polynomial function providing the best parametrization of the relation between the considered elevation change estimates and their absolute elevation. If the dh/dt value of the considered grid point is associated with a residual value larger than 3 times the standard deviation of all the residuals, it is marked as an outlier and excluded from the following extrapolation phase (The filter removes 5% in CryoSat-2-M1, 3% in CryoSat-2-M2 of the available measurements). We further discard anomalous positive elevation change rates with magnitudes above 2 m/yr. In order to validate our selection criterion, we evaluate the maximum accumulation rate in the region using synoptic monthly means of total precipitation from ERA/Interim. We cumulate the sum of liquid and solid precipitation between July 2010 and July 2016 and estimate their trend. We find maximum thickening rate of 0.6 meters/year, which is well below our selected threshold. We finally reject thinning rates above 10 meters per year that are well beyond maximum thinning rates observed over NZEM by Melkonian et al. [2016] and on the fastest glaciers of the Greenland and Antarctic ice sheets [McMillan et al., 2016]

3.2.4 Statistical Analysis

Statistical differences between thinning rates of marine- and land-terminating glaciers are investigated employing the Kruskal-Wallis test [Kruskal and Wallis, 1952]. The Kruskal-Wallis test is a nonparametric statistical test employed to compare samples from different populations when the normality and homoscedasticity assumptions required to apply the

one-way ANOVA (analysis of variance) are not met.

3.2.5 Spatial Extrapolation

ICESat inter-track spacing varies between 20 and 30 kilometers at the latitudes of NZEM. Therefore, large portions of the ice covered areas remain unsampled. Even when using the along track approach, we obtain elevation change estimates for less than 9% of the total glacier area. CryoSat-2, provides a spatial coverage one order of magnitude larger than that of ICESat. However, even in this case, elevation change measurements are missing for a portion of the total glacier area ranging between 33 and 36% depending on the methodology used to measure elevation change rates. In both cases, therefore, the evaluation of the total regional ice volume change requires the extrapolation of elevation change rates at the locations where measurements are not available. Moholdt et al. [2012] estimated the regional volume change for NZEM employing a hypsometric averaging approach based on the parametrization of the relationship between elevation change and absolute elevation using a third order polynomial function. The total ice volume change is calculated by multiplying the estimated polynomial function with the hypsometric areas within 50-meter elevation bins derived from an external DEM [Nuth et al., 2010, Moholdt et al., 2010]. The glacier area is therefore divided into elevation bands, with each band being assigned a mean elevation change rate equal to the value predicted by the polynomial function at the center of the 50-meter elevation interval. This extrapolation approach is based on the assumption that a single polynomial function can be used to characterize the variability of the elevation change rate with elevation at the entire regional scale. Nilsson et al. [2015a] tested the application of other regionalization schemes based on regional interpolation, obtaining mass balance estimates in agreement with those of Moholdt et al. [2012]. In this study, we update the approach presented in Moholdt et al. [2012] by designing an extrapolation scheme that considers not only the relation between elevation change and absolute elevation, but also its spatial variability.

We extrapolate elevation change rates for grid cells with no assigned elevation change value by applying the following steps. Given a grid cell with no value:

- we find all the measurements available within a distance smaller than or equal to a selected search radius and we evaluate the quadratic polynomial function that provides the best parametrization of the relation between the considered elevation change estimates and their mean elevation.
- We assign the considered grid cell an elevation change value equal to the value predicted by the quadratic polynomial at the mean absolute elevation of the grid cell calculated employing the ArcticDEM. We assign the grid cell an uncertainty value equal to the standard deviation of the dh/dt values used to determine the polynomial function that are contained within an elevation range of 50 meters from the mean elevation of the grid cell [Nuth et al., 2010].

In order to define a realistic distance useful for the noise reduction and extrapolation procedures, we evaluate the semivariogram of the elevation changes measured using the plane-fit. We find an autocorrelation distance (lag-correlation) equal to 50 kilometers. We obtain the same value when calculating the semivariogram of the regional glacier absolute elevation calculated employing the ArcticDEM previously downscaled to a 1 kilometer resolution. We therefore assume that ice elevation changes remain correlated for distances smaller than 50 km and we set the search radius equal to one half of the estimated autocorrelation distance. Our approach substantially differs from the one used by Moholdt et al. [2012]. In that case, the regional ice volume change was estimated by employing a regionalization scheme did not consider the spatial variability of the elevation change signal. The ice volume change was estimated through a single parametrization of the relation between elevation and elevation change for three main sub-regions (Glaciers facing Kara Sea, Glaciers Facing Barents Sea, and Glaciers outside the main ice cap). Their approach, therefore, did not consider the

local/spatial variability of the relation between elevation and elevation change.

3.2.6 From Volume To Mass Change

The ice volume change for each grid point is calculated by multiplying the relative mean elevation change value with the grid cell area. The total ice volume change is calculated by summing the contributions from all grid cells. The lack of data regarding possible changes in ice elevation due to snow/firn compaction complicates the conversion of ice volume change to mass volume change. Following Moholdt et al. [2012], we calculate the total ice mass change by multiplying the total volume change with the density of ice (0.917 g/cm^3) and consider the effect of this assumption in our error budget. We therefore assume that the elevation changes happen mainly at the density of ice, given that the largest part of the elevation change signal is located at low elevations (below 600-500 m) where ice melt and glacier dynamics should be the process driving elevation changes [Moholdt et al., 2012].

Error Analysis

We calculate the total uncertainty characterizing our final glacier mass change considering inaccuracy terms due to :

1. Elevation change measurement error ($\epsilon_{dh/dt}$);
2. Extrapolation error (ϵ_{ext});
3. Error in glacier area (ϵ_{area});
4. Sampling Bias Error (due to the non uniform distribution of the elevation change measurements on the glacier surface) (ϵ_{bias});

5. Error associated with the volume to mass conversion (ϵ_ρ);

We evaluate measurement error and extrapolation error following the approach used by Nilsson et al. [2015a]. We calculate at first the autocorrelation distance characterizing the measured elevation change values. The analysis of the ICESat dh/dt measurements shows a correlation length equal to 10 km in agreement with Nilsson et al. [2015a]. This value is significantly lower than the value found analyzing elevation changes measured by CryoSat-2: 50 km. This difference is probably related to the different distribution of elevation measurements between the two altimeters (ICESat observations are too sparse to fully characterize the spatial variability of the elevation change signal in the region). We use the correlation length obtained using elevation changes from CryoSat-2, taking a more conservative estimate of the elevation change signal autocorrelation. In the next step, we organize the measured elevation changes in bins regularly spaced by a distance equal to the autocorrelation length. Following Nilsson et al. [2015a], we consider elevation changes located in different bins to be uncorrelated. We calculate the elevation change mean measurement error per unit area as:

$$\epsilon_{dh/dt} = \frac{\sigma_{dh/dt}}{\sqrt{N}} \quad (3.3)$$

Where N is the number of non-empty uncorrelated bins and $\sigma_{dh/dt}$ is the mean standard deviation of the elevation changes calculated for each bin. Following Nilsson et al. [2015a] we calculate the mean extrapolation error per unit area as:

$$\epsilon_{ext} = \frac{\sigma_{ext}}{\sqrt{N}} \quad (3.4)$$

Where, N is again the number of non-empty uncorrelated bins and σ_{ext} is the mean standard deviation of the extrapolated elevation changes located within each bin.

We evaluate the Sampling Bias error by performing a Monte Carlo simulation. We generate a synthetic elevation change map on the 1km by 1km grid used for the averaging procedure.

We generate 1000 random sampling distributions defined in such a way that a fixed portion of the total glacier area is sampled at each iteration. We evaluate the sampling bias as the standard deviation of the difference between the value obtained in the 1000 iterations and the real mass change value. We estimate an error equal to 0.2 Gt/yr and we include it in the error budget. Elevation measurements over glacier surface are isolated employing glacier outlines designed using satellite imagery from the same decade of the two missions [Pfeffer et al., 2014, Rastner et al., 2017]. Following Moholdt et al. [2012], we assume the uncertainty associated with errors in glacier outlines to be within 5% of the total glacier area (A_{tot}). We calculate the volume error ϵ_{vol} as the sum in quadrature of all considered error components multiplied by the total glacier area:

$$\epsilon_{vol} = A_{tot} \cdot \sqrt{\epsilon_{dh/dt}^2 + \epsilon_{ext}^2 + \epsilon_{area}^2 + \epsilon_{bias}^2} \quad (3.5)$$

We finally include in the total error budget the error associated the volume to mass conversion following Moholdt et al. [2012]:

$$\epsilon_{mass} = \sqrt{(\epsilon_{vol} \cdot \rho_{ice})^2 + (\dot{V} \cdot \epsilon_{\rho})^2} \quad (3.6)$$

Where ρ_{ice} is the density of ice, \dot{V} is the estimated volume change and ϵ_{ρ} is calculated as $\epsilon_{\rho} = \frac{1}{2}(\rho_{ice} - \rho_{firn})$.

Time Series of Ice Elevation Change

CryoSat-2 has a repeat cycle of 369 days and a sub-cycle of 29 days [Wingham et al., 2006]. The same orbit is therefore nearly repeated with a small offset almost every month. Such a high repetition frequency allows the system to detect changes in ice elevation at a quasi-monthly temporal resolution. We estimate monthly mean variations of ice elevation employing the plane-fit residuals. Following Wouters et al. [2015] and Noël et al. [2018],

we evaluate monthly elevation anomalies at each 1 km grid centroid through summing the constant trend obtained by applying the plane-fit to the grid cell residuals. We parameterize the elevation anomalies obtained at the previous step as a function of absolute elevation. We calculate the mean elevation change time series for each 50-meter elevation bin. In order to obtain time series of regional ice volume change, we multiply single bin mean elevation change time series by the relative area. We finally obtain the regional glacier mass change time series by multiplying the sum of all 50-meter elevation bins volume change time series by the density of ice. We express the uncertainty associated with the single bin monthly volume anomaly as the standard deviation of the elevation residuals used to calculate the mean elevation anomaly value multiplied for the bin area. Different elevation bins are considered uncorrelated, therefore we sum their uncertainties in quadrature in order to evaluate the total monthly volume anomaly uncertainty. We finally consider the error introduced by the volume to mass conversion using equation 3.6.

3.3 Other Data

3.3.1 Glacier Inventories

The glaciers of NZEM are characterized by high dynamics and large changes on a decennial temporal scale [Carr et al., 2017, Pelto, 2016, Grant et al., 2009]. In order to minimize the uncertainty related to error in glaciers outlines we isolate ICESat and CryoSat-2 elevation data by employing glacier inventories based on independent observations obtained during the same time period of the missions. For the case of ICESat, we use glaciers outlines from the sixth release of the Randolph Glacier inventory, which was designed employing topographic data related to the time period 2000-2010 [Pfeffer et al., 2014]. For CryoSat-2, we employ the recently released glacier inventory designed at the University of Zurich and described

in Rastner et al. [2017]. This new database is based on the fusion of multi-source satellite data acquired between 2013 and 2016. Glaciers profiles were derived using Landsat 8 while glacier topographic attributes were obtained using elevation data from the ArcticDEM. The new inventory identifies a total glacier area of $22,379.0 \pm 246.2 \text{ km}^2$, larger than the total glacier area indicated by the Randolph Glacier Inventory 6.0: $22,128 \text{ pm } 6120 \text{ km}^2$.

3.3.2 Glacier Hypsometry

We derived the regional glacier hypsometry using the sixth release of ArcticDEM created by the National Geospatial-Intelligence Agency of the National Science Foundation. We used mosaic products provided at a 5-meter resolution and freely distributed by the Polar Geospatial Center at the University of Minnesota. This new digital elevation model is derived from Worldview and GeoEye-1 optical stereometric imagery acquired between 2013 and 2016 with the use of an automatic DEM generation algorithm, the Surface Extraction with Triangulated Irregular Network-based Search-space Minimization (SETSM) described in Noh and Howat [2017]. Vertical accuracy of each digital elevation model is improved by employing elevation data from the NASA ICESat mission. Elevation units are meters and are referenced to the WGS84 ellipsoid. We filled data gaps, especially located at low elevation, using the Aster GDEM V2 following Rastner et al. [2017]. Remaining data gaps that could not be filled with the Aster GDEM (these regions were also missing in this dataset) were filled employing elevation values from the GTOPO30 global elevation model.

3.3.3 Atmospheric Temperatures, Total Precipitation, and Ocean Data

Zeeberg and Forman [2001] observed a strong linear relation between mean summer temperatures and ablation, and between winter temperatures and accumulation. The analysis of seasonal temperatures can thus be useful in order to validate the seasonal/inter-annual variability present in the GRACE/CryoSat-2 mass/elevation change time series. We analyze air temperatures on NZEM employing 2-meter temperature (monthly mean of daily means) from the ERA/Interim reanalysis data [Dee et al., 2011]. ERA-Interim has a resolution of 0.75 degrees, which is quite coarse considering the size of the region of interest. We thus compare monthly temperature measurements obtained using meteorological stations provided by the Hydrometeorological Information - World Data Centre Baseline Climatological Data Sets (<http://meteo.ru/english/climate/temp.php>). We used data from two stations : Malye Karamakuly (59 E, 70.4 N - WMO ID: 20744) and E.K. Fedorova (52.7 E, 72.3 N - WMO Id: 20946). We compare monthly temperatures measured by the climatic stations with temperatures from ERA/Interim linearly interpolated at the same locations. The comparison shows a large agreement between the two datasets. In both cases, we find a root mean square difference below 0.7 celsius degrees and a significant correlation above 0.98 confirming the ability of ERA/Interim to correctly reproduce local surface temperatures. We perform the following analyses using monthly temperatures from ERA/Interim: we evaluate seasonal mean temperatures and their temporal anomalies for the time period between 1979 and 2002 in order to investigate climate variability in the region; we also use Synoptic Monthly Means of Total Precipitation in order to evaluate accumulation variability during the period under analysis. In this case, we do not use data from the meteorological stations, as these data are likely biased and underestimate solid precipitation [Moholdt et al., 2012].

We evaluate monthly Sea Surface Temperatures (SST) and Sea Ice Concentration (SIC) anomalies employing data from the Hadley Centre Sea Ice and Sea Surface Temperature data

set (HadISST) developed at the Met Office Hadley Centre for Climate Prediction and Research. Project data are freely available at (<https://www.metoffice.gov.uk/hadobs/hadisst/>) and provided on a global grid at a one degree resolution. SST and SIC are available at a monthly resolution for the time period between 1870 to present. The two datasets are the result of a combination of multiple data sources: SSTs are generated by merging historical and modern direct observations. SICs are generated combining ship- and air-born (digitized sea ice charts) with satellite data (passive microwave). A detailed description of this dataset can be found in Rayner et al. [2003]. We also evaluated SIC using data from NOAA/NSIDC Climate Data Record of Passive Microwave Sea Ice Concentration, Version 3 [Meier et al., 2017]. These datasets include SIC measured by passive microwave sensors (SMMR, SSM/I, SSMIS). Monthly SIC data are provided in this case at a 25 by 25 kilometers resolution. Our final SIC estimate is obtained as the average of the two datasets. As reported in Carr et al. [2017], NZEM glaciers are not located within long fjords and are relatively exposed to open ocean. Therefore we evaluate ocean temperature and sea ice fraction in a range of 50 kilometers from the NZEM shoreline in order to study the effect of variable ocean conditions on glacier mass balance.

In order to place the analysis of the NZEM mass balance's inter-annual variability on a broader scale, we use time series of the Hurrell North Atlantic Oscillation Station Based Index (NAO) [Hurrell, 2017]. We consider the Annual and the winter (December through March) versions of the index. The winter NAO Index (DJFM-NAO) is based on the difference of normalized sea level pressure (SLP) between Lisbon, Portugal and Stykkisholmur/Reykjavik, Iceland since 1864, while the Annual NAO Index (Annual-NAO) is based on the difference of normalized sea level pressures (SLP) between Ponta Delgada, Azores and Stykkisholmur/Reykjavik, Iceland since 1865.

In order to investigate the presence of linear trends in seasonal and annual time series of atmospheric and oceanic variables during the time period under study we employ the Mann-

Kendall test [Mann, 1945, Kendall, 1955] associated with the Sean-Slope estimator. The Mann-Kendall test is a non-parametric test commonly used to detect linear trends in time series analysis when the time series residuals are not normally distributed.

3.4 Results

3.4.1 GRACE

The mass change time series for NZEM between April 2002 and August 2016 are shown in Figure 3.2 while the total annual mass balance values are presented in Table 3.1. During the entire time period under analysis NZEM glaciers lost mass with an average rate of -8 ± 4 Gt/yr. We do not find evidence of a statistically significant acceleration in mass loss over time. This result is confirmed by both the AIC_c and the R_{adj}^2 criterion (i.e. adding a quadratic parameter to the model function does not help explain further variability in the mass change signal). At the same time, the GRACE-derived time series shows a pronounced inter-annual variability characterized by the alternation of phases with negative and positive annual mass balance. We observe a first phase of stable mass loss between 2003 and 2008, a second phase with positive glacier mass balance between 2008 and 2010, and a final phase with increasing mass loss between 2010 and 2017. We analyze the GRACE time series during the sub-periods overlapping with the ICESat and CryoSat-2 missions. Between October 2003 and October 2009, we estimate a mass loss equal to -10 ± 5 Gt/yr. During this phase, we register five consecutive years of negative annual mass balance with an extreme mass loss event of -24.9 Gt registered in 2004. After two consecutive year of mass gain (2009, 2010), the mass balance returned to a negative state. Between July 2010 and July 2016 we estimate an average loss rate equal to -14.3 ± 4 Gt/yr, resulting in a 44% increase in mass loss with respect 2003 to 2009 and almost doubling the mass loss registered for the entire time period

under analysis. During this last phase we register 3 of the 4 years with the highest mass loss over the entire period under analysis: 2013, 2015 and 2016 (see Table 3.1). More stable conditions are instead observed between 2014 and 2015. Between 2002 and 2017, glacier mass balance was negative for 11 of the 13 considered glaciological years, contributing to a cumulative ice loss of -124 Gt equivalent to 0.32 mm of SLR. Our estimates are in agreement with Reager et al. [2016] for the period (2002-2014) and with Matsuo and Heki [2013] for the period (2004-2012), both obtained using GRACE products from the fifth GRACE data release (RL05). We find, however, large disagreement with results by Sun et al. [2017], which measured a mass loss rate equal to -1.04 ± 0.25 Gt/yr between 2003 and 2014 (for the same time period we find -7.5 ± 4 Gt/yr). We attribute the large disagreement between the two estimates to the different data processing techniques applied to the GRACE data before evaluating the regional ice mass change. Following Jacob et al. [2012b] we do not apply a decorrelation (de-stripe) filtering [Swenson and Wahr, 2006a]; given the high latitude of the region of our interest, the effect of correlated noise present in the monthly gravity solutions has limited influence on the local mass change signal. In this way, we also avoid the spreading of the mass change signal caused by the application of the anisotropic de-stripping filter that would otherwise affect the estimated mass change in regions like NZEM, which are small compared to the satellite resolution. Moholdt et al. [2012] estimated a mass loss in the region using GRACE equal to -5.8 Gt/yr between October 2003 and October 2009. During the same period, we find a larger mass loss equal to -9.9 ± 4.8 Gt/yr. Even though the two estimates are in agreement within their error bounds, estimates by Moholdt et al. [2012] were obtained using an older GRACE data release (RL04) and a different GIA correction (ICE-5G, [Peltier, 2004]). Melkonian et al. [2016] used a mixture of geodetical techniques (Difference between WorldView Dems and Difference between WorldView Dems and ICESat) to evaluate the mass change on NZEM glaciers for the time periods 2003-2013/2014 and 2012-2013/2014. Between 2003-2013/2014, they estimate a mass loss equal to -12.1 Gt/yr, which is higher than the value we find for the same time period, -6.5 ± 4 Gt/yr. For the time

period 2012-2013/2014 they find a mass loss equal to -8.5 Gt/yr, which is almost 50% of the mass loss we estimate for the same time period. These large differences are related to the inability of geodetical techniques to capture long- and short-term variability in the mass loss signal like the decrease in mass loss observed between 2008 and 2010 and the record mass loss of -26.12 Gt between 2012 and 2013, which are however captured by GRACE. Figure 3.2 contains also the NZEM glacier mass change time series calculated with GRACE and CryoSat-2. CryoSat-2 mass change time series compares extremely well with GRACE not only in terms of trend but also in terms of annual/inter-annual variability. We find a correlation equal to 0.92 between 13-month smoothed versions of the two time series.

3.4.2 ICESat and CryoSat-2

Elevation change estimates obtained using ICESat are presented in Figure 3.3. Between 2003 and 2009 we estimate a glacier mass change equal to -7.8 ± 4 Gt/year in good agreement with the value found by GRACE (-10 ± 5 Gt/yr). These ICESat estimates are within errors with those presented by Moholdt et al. [2012], which found a mass loss rate equal to -7.6 ± 1.2 Gt/yr using ICESat. Our ICESat estimate differs from those by Moholdt et al. [2012] by 0.24 Gt/yr due to the different regionalization scheme used in this study. ICESat measurements show that the ice loss in the region is associated with marked glacier thinning at elevations below 500 meters, with the highest thinning rates measured over the Barents Sea coast where we observe thinning rates above 3 m/yr at elevations below 200 m.

Elevation change estimates from CryoSat-2-M1 and CryoSat-2-M2 are presented in Figures 3.4 and 3.5 with the relative uncertainty maps shown in Figure 3.6. For the time period under analysis (07/2010 - 07/2016) we estimate a glacier mass loss equal to -12.3 ± 5.4 Gt/yr with CryoSat-2-M1 and -13.3 ± 5 Gt/yr with CryoSat-2-M2. Results from the two methodologies are therefore consistent and in agreement with mass change estimates obtained

using GRACE during the same time period. Also in this case, the mass loss is associated to widespread glaciers thinning at low elevations. Thinning rates reach their maximum values below 200 meters while more stable conditions or even slight increase in elevation are observed above 700 meters on both the Barents and Kara Sea coasts. Figures 3.4 and 3.5 show maps of elevation change before the extrapolation phase and after the application of the local regression filter. In terms of spatial coverage, we obtain valid observations for 67% with CryoSat-2-M1 and 64% with CryoSat-2-M2 of the total glacier area. These values are one order of magnitude higher than the 9% obtained with ICESat. Final estimates by CryoSat-2 are therefore less dependent on the extrapolation scheme selected to evaluate the regional ice volume change. Table 3.3 shows how the mass loss is partitioned between five main sub-regions classified according to coast and terminus type (see Figure 3.1):

- Marine-Terminating Glaciers - Barents Sea (8,703 km^2);
- Marine-Terminating Glaciers - Kara Sea (7,016.4 km^2);
- Land-Terminating Glaciers - Barents Sea (2,260.9 km^2);
- Land-Terminating Glaciers - Kara Sea (2,277.9 km^2);
- Minor Glaciers (1,612.3 km^2).

Results from the two methodologies are consistent with differences less than than 1 Gt/yr in all the sub-regions. 50% of the total loss takes place over marine- and land-terminating glaciers facing the Barents Sea coast. The remaining 50% is partitioned between marine- and land-terminating glaciers facing the Kara Sea and all the Minor Glaciers located on the Souther part of the Archipelago between Yuzhny and Severny Island.

Between 2003 and 2009 Moholdt et al. [2012] found no significant difference between frontal thinning of marine- and land-terminating glaciers (-0.92 m/yr vs. -0.90 m/yr). Table 3.4

shows thinning rates measured at low elevations (below 500 m) calculated using CryoSat-2-M1 and CryoSat-2-M2 for the five NZEM sub-regions presented above. The Kruskal-Wallis test indicates that thinning rates on the Barents sea are significantly higher (p-value < 0.05) than thinning rates measured on the the Kara sea. In both cases, tidewater glaciers presented thinning rates at low elevations significantly higher than thinning rates of land terminating glaciers on the same coast. This result is consistent with those of Melkonian et al. [2016] and Carr et al. [2017]. The high thinning rates at low elevation found for tidewater glaciers facing the Barents and the Kara sea suggest that part of the observed ice volume loss can be attributed to dynamic thinning and thus ice dynamics and mass loss by calving play a significant role in the glacier mass balance of the region.

3.4.3 Single Drainage Basin Analysis

Figures 3.7, 3.8, 3.9, 3.10 show the relation between absolute elevation and elevation change evaluated using ICESat and CryoSat-2-M1 and CryoSat-2-M2 over the main marine- and land-terminating glaciers facing the Barents and the Kara Sea. Glaciers facing the Kara Sea are characterized by a more gentle slope and a less complex topography. Therefore CryoSat-2 provides a more uniform coverage over each drainage basin in this area. Scatter plots for marine- and land-terminating glaciers facing the Kara Sea (3.7, and 3.9) show a clear pattern of increasing thinning rates with decreasing absolute elevation. Figures 3.8 and 3.10, corresponding to the Barents Sea glaciers, are instead discontinuous and more affected by noise. In almost all considered glaciers, measurements at intermediate elevations are almost completely missing. Barents Sea glaciers are characterized by a more complex glacier morphology (more rugged surfaces, higher slopes and narrower drainage basins) together with a smaller average glacier area (The total Barents Sea glacier area is larger than the total glacier area of the Kara sea. However, single drainage basins on the Kara sea are on average larger. Marine-terminating glaciers on the Kara Sea have a mean area value of 559 km^2 , while

glacier on the Barents Sea have a mean area value of 306 km^2 , Land-terminating Glaciers on the Kara sea have a mean area value of 14.8 km^2 while the corresponding value on the Barents sea is 6.3 km^2). These differences limit the ability of CryoSat-2 to correctly capture changes in ice elevation especially on the North-Western side of the Archipelago (see Figure 3.6). However, in all the considered cases, a consistent pattern of increasing ice thinning rates with decreasing absolute elevation remains visible. We also compare elevation changes obtained with CryoSat-2-M1 and CryoSat-2-M2 with those obtained by ICESat over the same drainage basins. Given the small footprint size (one order of magnitude smaller than the footprint of CryoSat-2), ICESat measurements tend to be more accurate and less affected by noise. However, by comparing the elevation changes obtained with CryoSat-2 over the same glaciers, we observe the same pattern of variation of dh/dt with elevation. Finally, the comparison between elevation changes estimated with ICESat with those obtained using CryoSat-2 are consistent when compared over the same locations, indicating that the use of larger radius, when applying plane fit regression in the CryoSat-2 case, does not affect our ability to detect elevation changes at the single basin scale. The number of observations with CryoSat-2 is an order of magnitude larger than ICESat, allowing a more complete characterization of glacier changes over the entire region. The highest thinning rates are measured by CryoSat-2 over marine-terminating glaciers, especially for those facing the Barents Sea where CryoSat-2 measures peaks in elevation changes above 3 m/yr below 200 meters. Thinning rates over land-terminating glaciers are, in general, well below the rates measured for tidewater glaciers over the same coast and are almost never below -1 m/yr .

3.4.4 Surface Temperatures and Total Precipitation

Seasonal temperatures and total precipitation between 2002 and 2016, measured using data from the ERA/Interim reanalysis model, are shown in Figure 3.11. In order to evaluate the shift in the regional climate, we express both variables as anomalies with respect 1979-2002.

Between 2002 and 2004, we observe mean temperatures below normal (summer Temperature Anomaly: -0.7°C) and precipitation above the normal in almost all seasons (with maximum precipitation amounting to 190 mm in summer 2002). These atmospheric conditions contributed to the near-zero mass balance registered during the glaciological year 2002-2003. Between 2004 and 2009 we observe winter temperatures significantly higher with respect to those registered during the reference period (Mean positive anomaly of 4°C). Total Precipitation was above the mean during summer and autumn. The same pattern of increased precipitation and temperatures was observed by Moholdt et al. [2012]. They interpreted this result as evidence of regional climatic mass budget not deviating from values registered in the previous decades. The regional glacier mass balance was positive in 2009 and 2010. These two years were characterized by increased precipitation in almost all seasons and winter and summer temperatures being 0.2°C below the long-term average in 2010.

Between 2011 and 2016, summer temperatures were significantly above the 1979-2002 average in all seasons (4°C in winter, 3°C in spring, 2°C in autumn, and 0.8°C in summer) except for the summer and autumn of 2014. Maximum positive anomalies (above 1°C) were registered in the summers of 2013 and 2015, when mass balance measured by GRACE was highly negative (-26.12 and -23.09 Gt). We observe similar temperature anomalies in the time series of mean temperatures measured by the climatic station located at Malye Karmakuly (see Figure 3.14).

We use the Mann-Kendall test in order to investigate the presence of a trend in seasonal temperatures during the period 2002-2016. We find a significant positive trend during autumn ($2.4^{\circ}\text{C} \pm 1.5$ degree/decade) and summer ($1.1^{\circ}\text{C} \pm 0.6$ deg/decade).

Zeeberg and Forman [2001] observed a strong linear relation between mean summer temperatures and ablation. The analysis of seasonal temperatures can therefore be useful in order to validate the seasonal/inter-annual variability present in the GRACE/CryoSat-2 mass/elevation change time series. We compare time series of summer temperature anomalies with annual mass balance from GRACE. (We normalize the time series before the com-

parison: we remove their mean relative to the overlapping period and divide the result by the standard deviation of the residuals). We find that the two time series are significantly anti-correlated ($R=-0.69$) confirming that summer atmospheric temperatures are an optimal predictor of the annual glacier mass balance variability (see Figure 3.12).

3.4.5 Sea Ice Concentration and Sea Surface Temperatures

Figure 3.15 shows time series of Sea Surface Temperature (SST) and Sea Ice Concentration (SIC) measured over the coasts of the Barents and Kara Seas. SST series are expressed as anomalies with respect to 1979-2002. Ocean conditions on the two coasts were significantly different during the period of study. On the Barents Sea coast, SST were below the average between 2002 and 2004, while spring and winter temperatures were 1°C above the long-term mean were observed between 2004 and 2009. Between 2009 and 2016, we register instead positive temperature anomalies between 0.5°C and 1.5°C in the seasons. After 2004, monthly SSTs were always significantly warmer than the reference period. On the Kara Sea, we observe more stable conditions, with ocean temperatures not significantly above the mean until 2005. After 2010 we observe an exceptional increase in seasonal temperatures with peaks of 2°C above the long-term mean in summer. The Mann-Kendall test reveals positive trends in the order of $\sim 1^{\circ}\text{C}/\text{decade}$ of summer and autumn temperatures between 2002 and 2016 on both sides of the archipelago.

Large differences between the two coasts exist also in terms of Sea Ice Concentration. Low SIC values are registered on the Barents Sea during the entire period of study. We observe that the ice coverage was above 80% only during the spring of 2004. We measure decreasing concentration in all the seasons with summer and autumn concentration always below 10% after 2006. (Between 2010 and 2012 SIC coastal regions remained almost ice free). Conditions were generally more stable on the Kara Sea coast where winter and spring concentrations remained above 80%. Summer and autumn SIC decreased during the observation period

with values consistently below 20% between 2010 and 2014.

3.4.6 North Atlantic Oscillation

Time series of DJFM-NAO and Annual-NAO are presented in Figure 3.13. Between 1970s and 1990s the NAO remained locked in a prolonged positive phase. Decreasing NAO values are observed after 1995. Between 2000 and 2010 the NAO switched to an almost neutral phase characterized by index values largely below those observed during the previous decades. The index was strongly positive only between 2007 and 2008, before turning strongly negative between 2009 and 2010. The winter of 2010 was in fact characterized by the most negative DJFM-NAO registered since 1864 [Osborn, 2011]. Between 2011 and 2017, the NAO turned again to a positive phase with a strongly positive index during 4 of 5 considered years.

3.5 Discussion

We estimate the mass balance of the NZEM glacier for a 14-year time period extending for the entire lifetime of the GRACE mission. Our analysis covers a time period two times longer than the one considered in Moholdt et al. [2012] and extends by several years the the analysis of Reager et al. [2016]. A longer data record allows for a more complete analysis of the inter-annual variation of the glacier mass change signal. Our results from satellite gravimetry and satellite altimetry are consistent and indicate that during the period of our study the measured mass loss was associated with fast thinning rates affecting both land- and marine-terminating glaciers. Marine-terminating glaciers thinned significantly faster than land-terminating glaciers, suggesting that the observed mass loss between 2010 and 2016 was determined by both negative surface mass balance and accelerated ice discharge. Our findings are consistent with the high glacier retreat rates observed by Carr et al. [2017],

the increased melt season length observed by Zhao et al. [2014], and the marked acceleration of marine outlet glaciers observed by Melkonian et al. [2016] during the same time period.

We measure an average ice mass loss of -8 ± 4 Gt/yr, which makes NZEM the 6th contributor to SLR in the Arctic after Greenland, the Canadian Archipelago, Alaska, Iceland, and Svalbard. Glaciers in the region went through alternative phases of positive and negative mass balance. Between 2002 and 2009, the regional mass balance was negative (-10 ± 5 Gt/yr). This first period was characterized by winter temperatures on average 4 to 6°C higher than the long-term mean and increased total annual precipitation. Atmospheric temperatures in the other seasons were instead not significantly different from the past. We observe a similar pattern of variability in SST over the Barents Sea coast. Here, summer temperatures were not different from the previous decades, while we measure a $\sim 1^\circ\text{C}$ positive anomaly in winter and spring consistent with the contemporary rapid decline of Sea Ice Concentration.

The NAO index started declining after 1995 and remained in an almost neutral phase until 2009. Zeeberg [2001] suggested that there is a delay of three to five years between a strong variation in NAO and the response of seasonal atmospheric temperatures related to transit time of North Atlantic Water to the Barents Sea. Our analysis shows that after the NAO switched to a new phase at the end of the 1990's, the influx of warm water into the Barents Sea from the Atlantic might have continued favoring stable climatic conditions and a progressive decline in SIC. Our findings are therefore in agreement with those by Moholdt et al. [2012] and indicate that, during the first decade of this century, the NZEM's climatic mass budget did not significantly changed with respect to the previous decades.

The regional mass balance was positive between 2009 and 2010. During this time period, a record negative NAO favored summer temperatures below average and enhanced precipitation that contributed to the positive mass balance measured by GRACE and CryoSat-2.

After 2010, the glacier mass in the region started declining again, while the NAO switched to

a new strongly positive phase. We measure record mean summer Atmospheric Temperatures in 2013, 2015 and 2016 associated with the most negative annual mass balances measured by GRACE during the entire period of study. Seasonal temperatures were in general always above the 1979-2002 mean except for summer 2014. Ocean conditions kept changing with SST above the 1979-2002 mean in all the seasons and sea ice concentration in rapid decline. On the Kara Sea, we measure mean summer and autumn SIC below 20% for the first time during the entire time period covered by data used in our analysis (1870-Present). The more stable conditions observed in 2014 by both GRACE and CryoSat-2 are consistent with the slowdown in glacier retreat observed by Carr et al. [2017] between 2014 and 2015.

Our analysis shows a marked relation between summer Temperatures and NZEM's glacier mass balance. During the GRACE time period, we found three glaciological years with positive mass balance: 2003, 2009 and 2010. In all the three cases, Sumer temperatures were below the long-term mean. The highest summer temperatures anomalies are measured after 2010. This result is consistent with the increased mass loss observed during the same time period.

The analysis of the mass change time series together with those of the climatic variables suggests that the mass loss in the region is the result of a long-term warming process characterized by increasing atmospheric and ocean temperatures. The analysis also presents evidences of a shift of climate in the region after 2010 with the NAO turning to a highly positive phase and contributing atmospheric and ocean temperatures largely above the mean of the previous decades. The entire process was associated with a destabilization the ocean conditions on the Kara sea where we measure unprecedented high SST and low SIC.

3.6 Conclusions

We employ two independent techniques to evaluate the mass balance of the Novaya Zemlya Archipelago during the last two decades. Estimates by satellite altimetry and satellite gravimetry are in good agreement and show that glaciers in the region are losing mass as a consequence of a long-term warming process that begun at the end of the nineteenth century. During the period of study, we estimate a mean ice mass loss equal to -8 ± 4 Gt/yr corresponding to a yearly contribution to sea level of 0.021 mm. After 2010, a North Atlantic Oscillation in a strong positive phase contributed to a large increase in atmospheric and ocean temperatures. The largest changes took place on the Kara Sea coast where increasing ocean temperatures and declining sea ice concentrations were registered for the first time after 2005. The shift in regional climatic conditions determined a 44% increase in mass loss. Elevation changes measured by CryoSat-2 and ICESat show that the mass loss in the region was associated with rapid glacier thinning at elevations below 500 meters. After 2010, the fastest thinning rates took place at the front of marine-terminating glaciers, suggesting that glacier volume changes due to increased glacier dynamics and ice discharge played a role in the total mass loss.

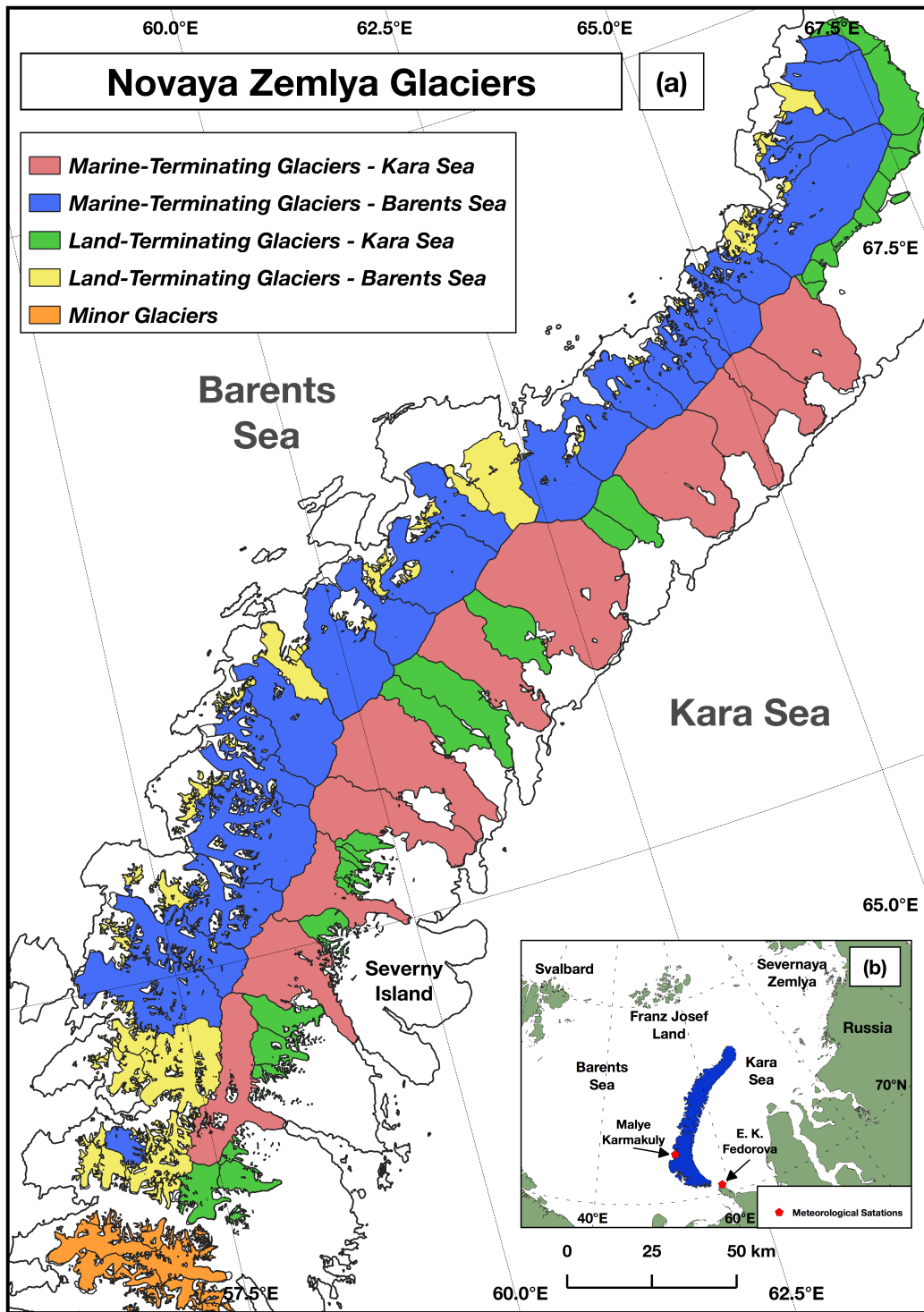


Figure 3.1: (a) Novaya Zemlya Glaciers: in red, Marine-Terminating Glaciers facing the Kara Sea, in blue, Marine-Terminating Glaciers facing the Barents Sea, in green, Land-Terminating Glaciers facing the Kara Sea, in yellow, Land-Terminating Glaciers facing the Barents Sea, in orange, Minor Glaciers. Glaciers Outlines from Rastner et al. [2017]. (b) Location of Novaya Zemlya.

Year	Annual Mass Balance
2003	-0.10
2004	-25.90
2005	-6.02
2006	-11.90
2007	-11.77
2008	-9.45
2009	4.45
2010	9.83
2011	-9.24
2012	-9.89
2013	-26.12
2014	-4.79
2015	-23.09
Total	-124

Table 3.1: Annual Mass Balance of Novaya Zemlya expressed in Giga-tons [Gt].

Time Period	Total Mass Balance	GRACE	GIA	Hydrology
04/2002 - 07/2016	-8 ± 4	-4.5 ± 2.9	-3.2 ± 1.6	-0.2 ± 0.2
10/2003-10/2009	-10 ± 5	-6.2 ± 2.6	-3.2 ± 1.6	-0.3 ± 0.1
07/2010-07/2016	-14.3 ± 4	-10.9 ± 2.4	-3.2 ± 1.6	-0.2 ± 0.1

Table 3.2: NZEM Glacier Mass Balance calculated with GRACE. The table contains the Glacier Mass Change rates for the three time period analyzed in this study. Total mass balance and its components are expressed in Giga-tons [Gt] Uncertainties are calculated as described in the text.

Region	CryoSat-2 - M1	CryoSat-2 - M2
Novaya Zemlya	-13.3±5.3	-12.9±5.1
Marine-Terminating - Barents Sea	-4.9±1.2	-5.1±1.3
Land-Terminating - Barents Sea	-1.8±0.6	-1.8±1.2
Marine-Terminating - Kara Sea	-2.4±0.8	-2.6±0.8
Land-Terminating - Kara Sea	-0.8±0.5	-0.9±0.5
Minor Glaciers	-2.5±0.8	-2.5±0.9

Table 3.3: Mass Change rates for NZEM glaciers and for the five considered sub-regions obtained with CryoSat-2-M1 and CryoSat-2-M2. NZEM glaciers are classified according coast and terminus type. Mass change rates are expressed in Giga-tons per year.

Region	CryoSat-2 - M1	CryoSat-2 - M2
Marine-Terminating - Barents Sea	-1,27	-1.37
Land-Terminating - Barents Sea	-1.00	-1.10
Marine-Terminating - Kara Sea	-0.90	-0.96
Land-Terminating - Kara Sea	-0.55	-0.68
Minor Glaciers	-2.50	-2.50

Table 3.4: Ice Thinning Rate measured at below 500 m near the glacier frontal areas. NZEM glaciers are classified according coast and terminus type. Thinning rates are expressed in meters per year.

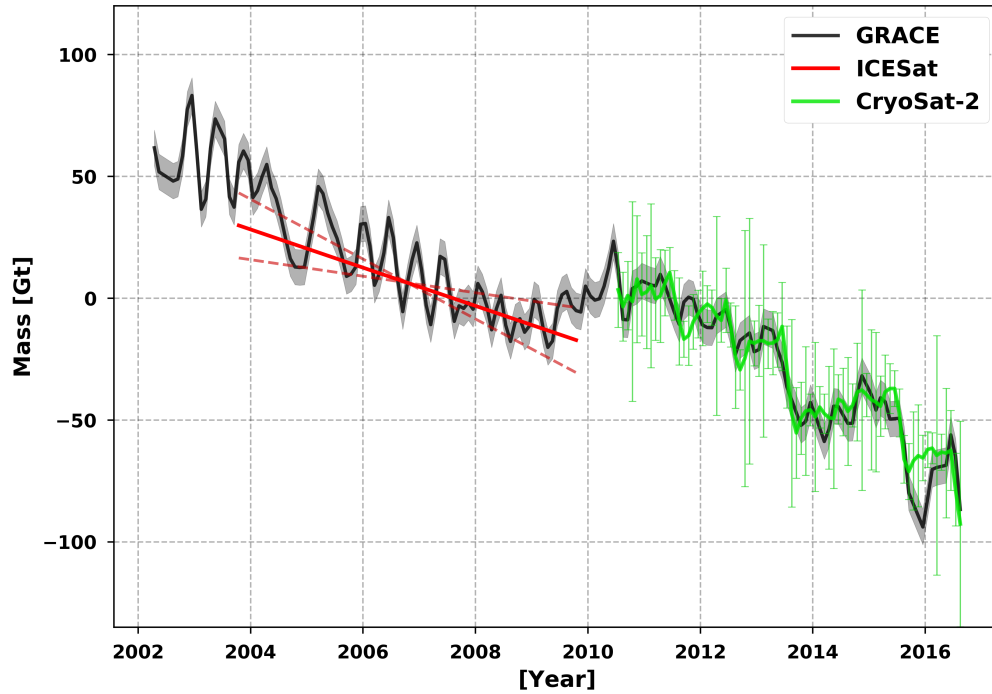


Figure 3.2: NZEM ice mass time series for the time period between April 2002 and August 2016. In black, the GRACE-derived mass change time series. The light grey band shows the monthly measurement error affecting GRACE estimates. The red line shows the ice mass loss estimated using ICESat between October 2003 and October 2009. The red-dashed lines represent the upper and the lower bounds of the estimated mass loss. In green, the mass change time series evaluated using CryoSat-2 between July 2010 and August 2016. The green error-bars correspond to estimated uncertainties in the monthly mass anomalies estimated using CryoSat-2. Time series and relative uncertainties are calculated as described in the main text.

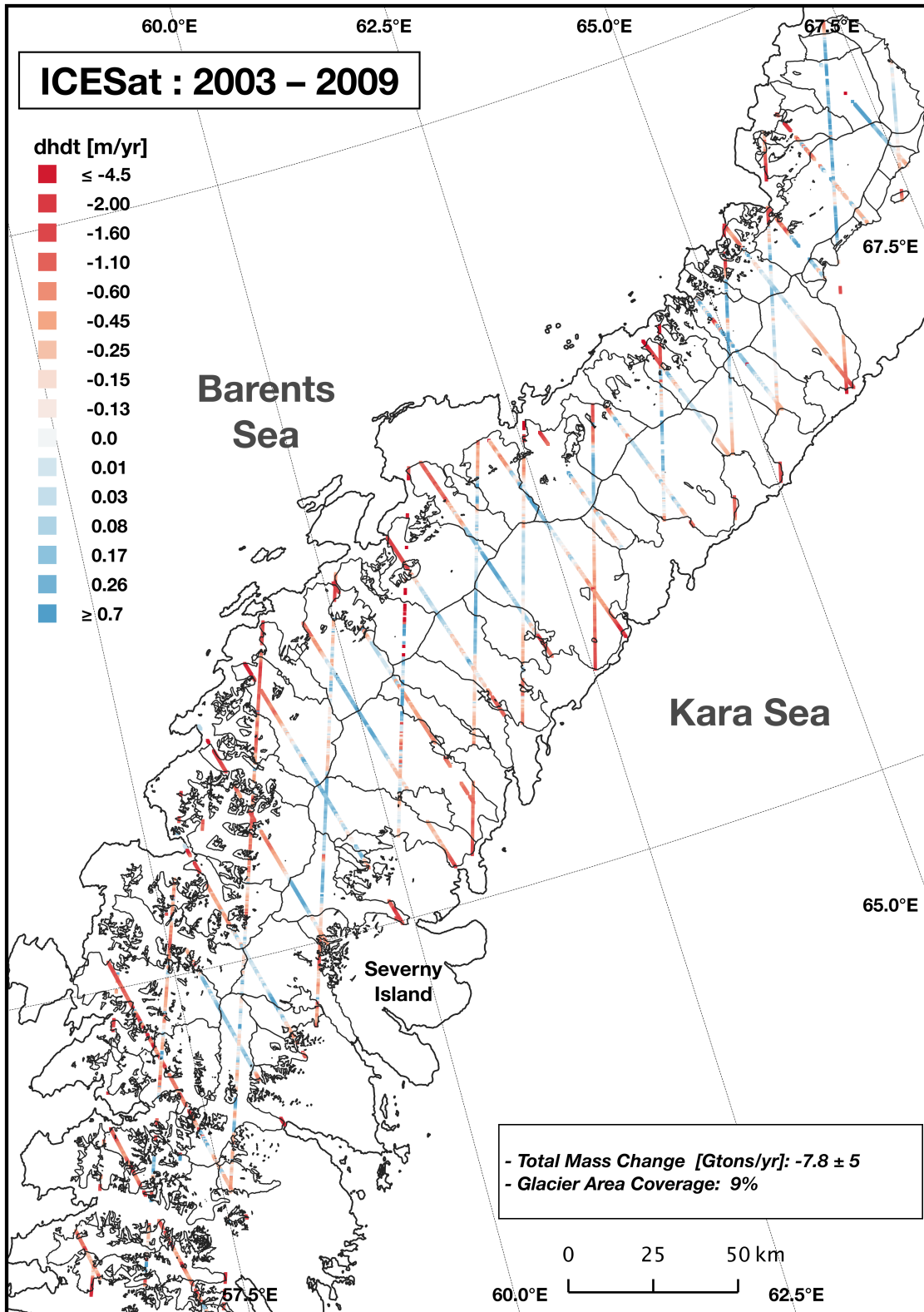


Figure 3.3: Map of Ice Elevation Change for NZEM estimated using ICESat for the time period between October 2003 and October 2009. Regional glaciers outlines are extracted from the sixth release of the Randolph Glacier Inventory [Pfeffer et al., 2014].

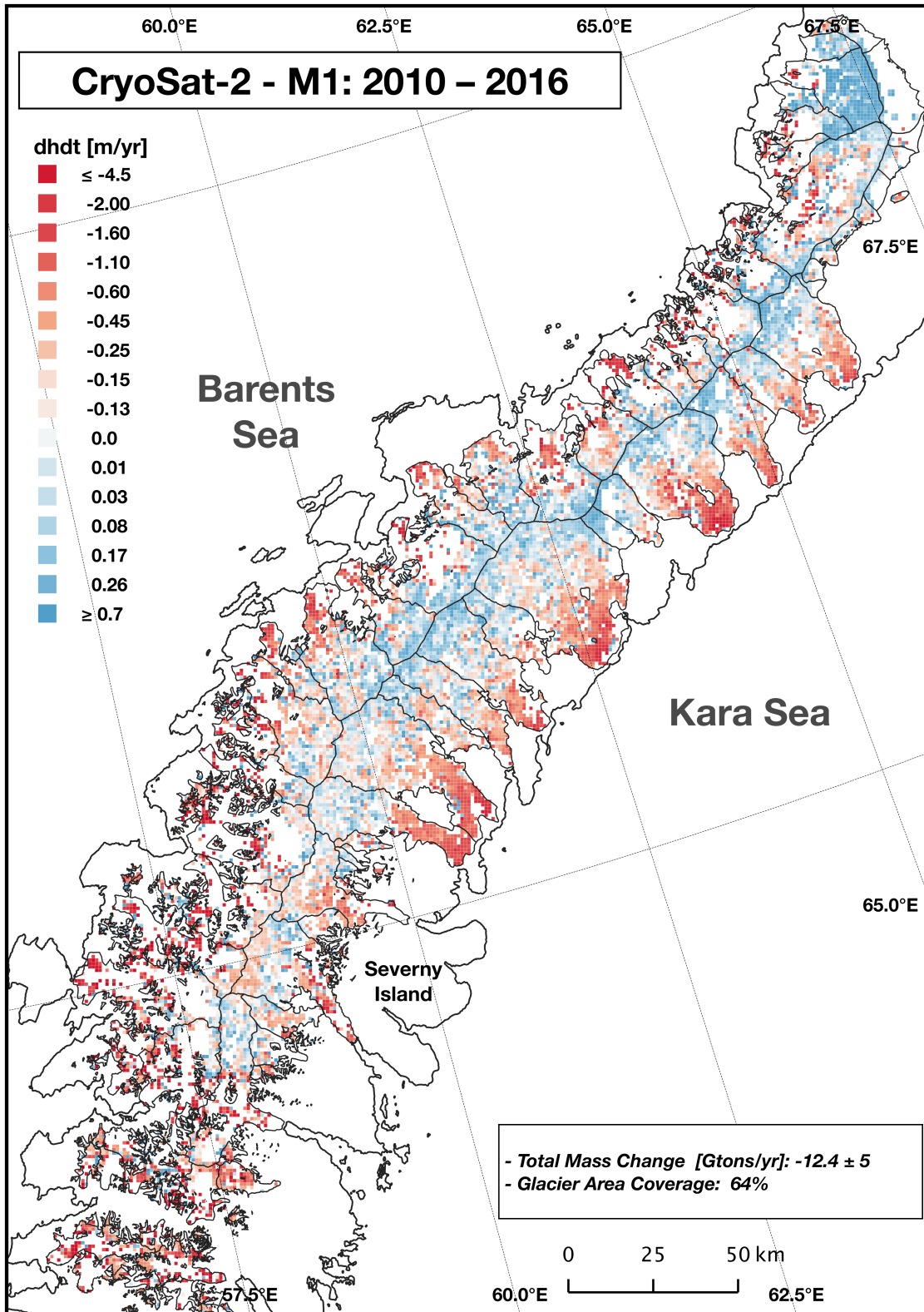


Figure 3.4: Map of Ice Elevation Change for NZEM estimated using CryoSat-2 Method 1 (CryoSat-2-M1) for the time period between July 2010 and July 2016. Regional glacier outlines are extracted from the new glacier inventory described in Rastner et al. [2017].

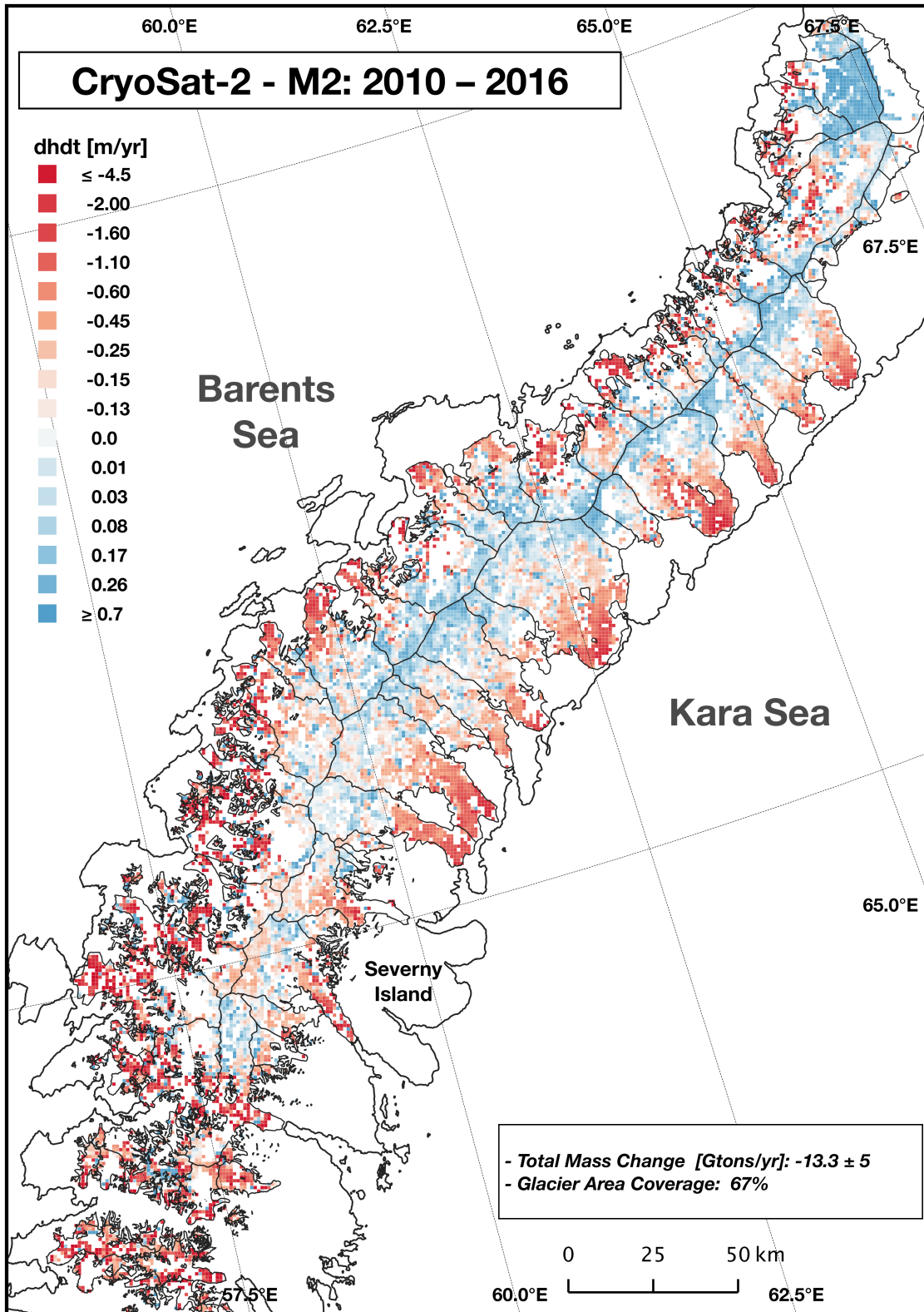


Figure 3.5: Map of Ice Elevation Change for NZEM estimated using CryoSat-2 Method 2 (CryoSat-2-M2) for the time period between July 2010 and July 2016. Regional glacier outlines are extracted from the new glacier inventory described in Rastner et al. [2017].

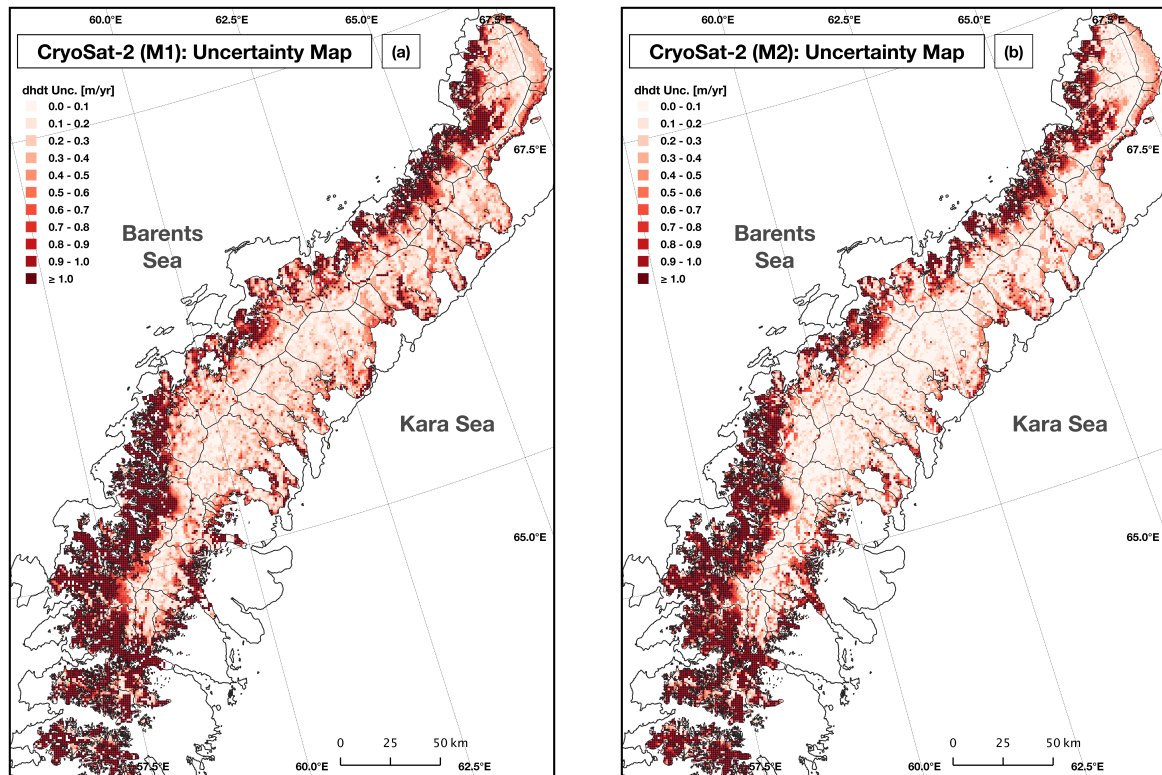


Figure 3.6: Ice Elevation Change Uncertainty Map calculated for: (a) CryoSat-2 Method 1 (CryoSat-2-M1) and (b) CryoSat-2 Method 2 (CryoSat-2-M2). Grid-points uncertainty values are calculated as described in the text and expressed in meters-per-year [m/yr]. Regional glacier outlines from Rastner et al. [2017].

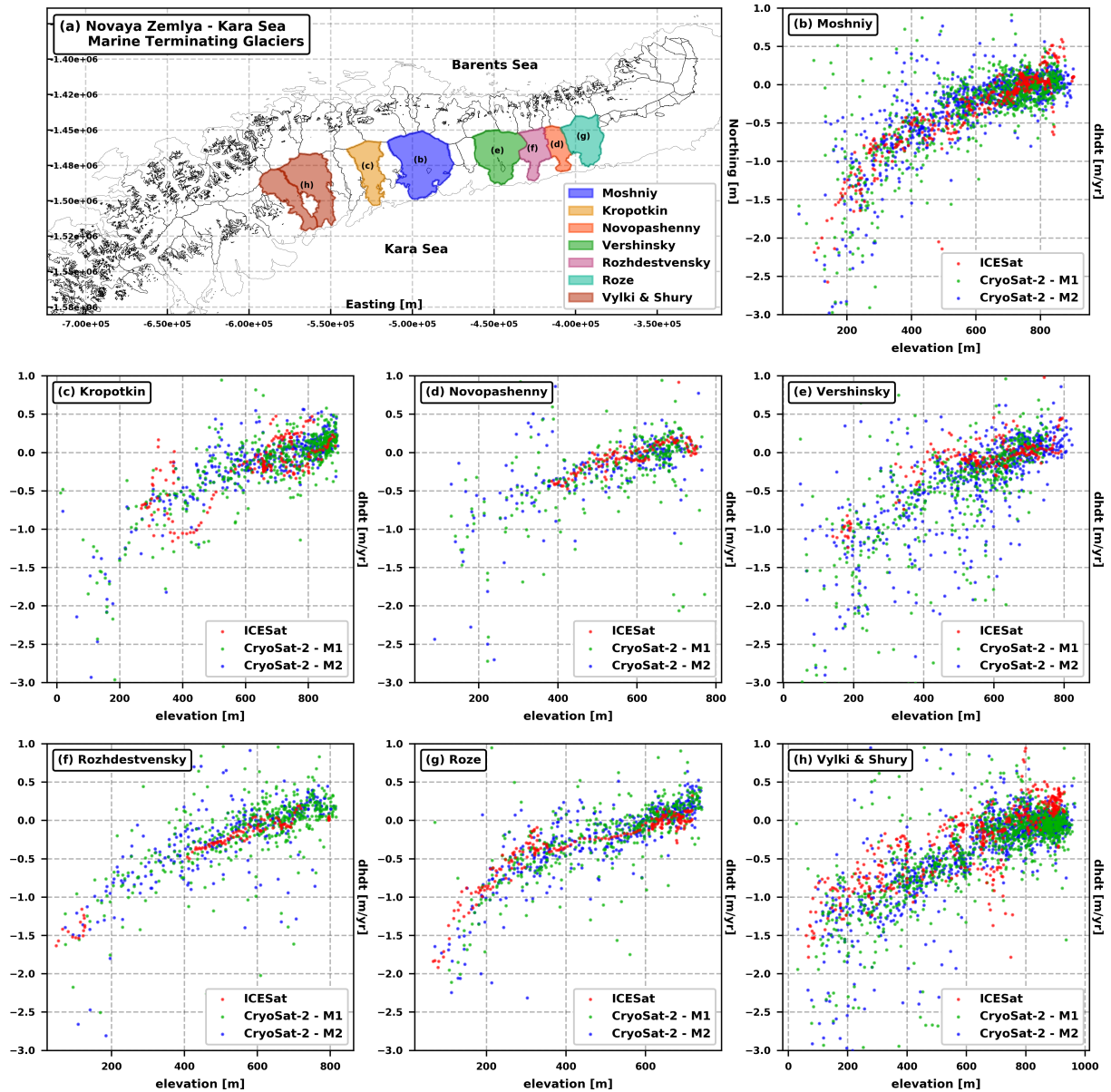


Figure 3.7: Elevation Vs Elevation Changes calculated for the major marine-terminating glaciers facing the Kara Sea calculated using ICESat, CryoSat-2 - M1, and CryoSat-2 - M2. (a) Novaya Zemlya Glaciers, (b) Moshniy Glacier, (c) Koproktin Glacier, (d) Navopashenny Glacier, (e) Vershinsky Glacier, (f) Rozhdestvensky Glacier, (g) Roze Glacier, (h) Vylki and Shury Glaciers.

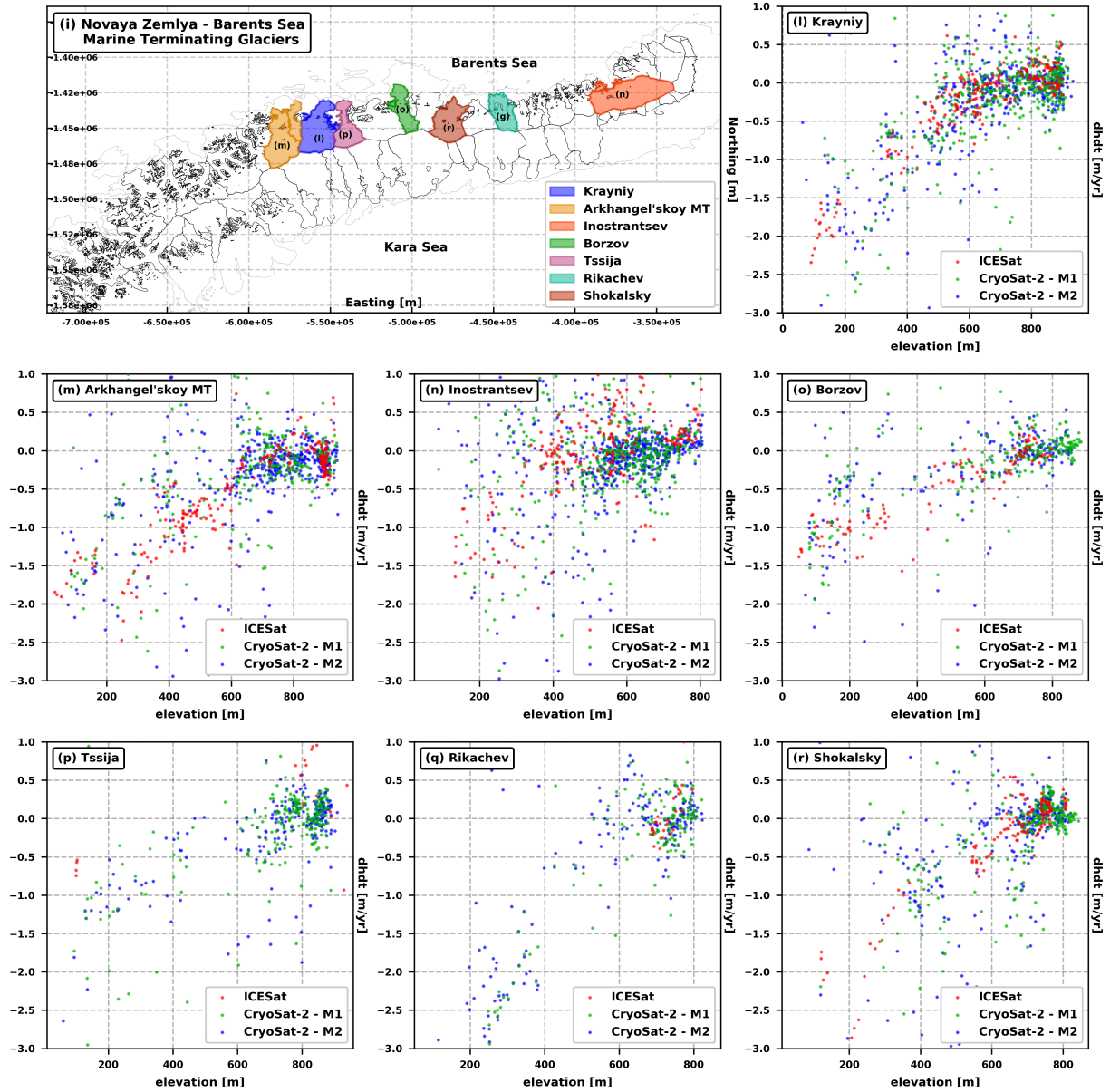


Figure 3.8: Elevation Vs Elevation Changes calculated for the major marine-terminating glaciers facing the Kara Sea calculated using ICESat, CryoSat-2 - M1, and CryoSat-2 - M2. (i) Novaya Zemlya Glaciers, (l) Krayniy Glacier, (m) Arkhangelosky Glacier, (n) Inostrntsev Glacier, (o) Borzov Glacier, (p) Tssija Glacier, (q) Rikachev Glacier, (h) Shokalsky Glacier.

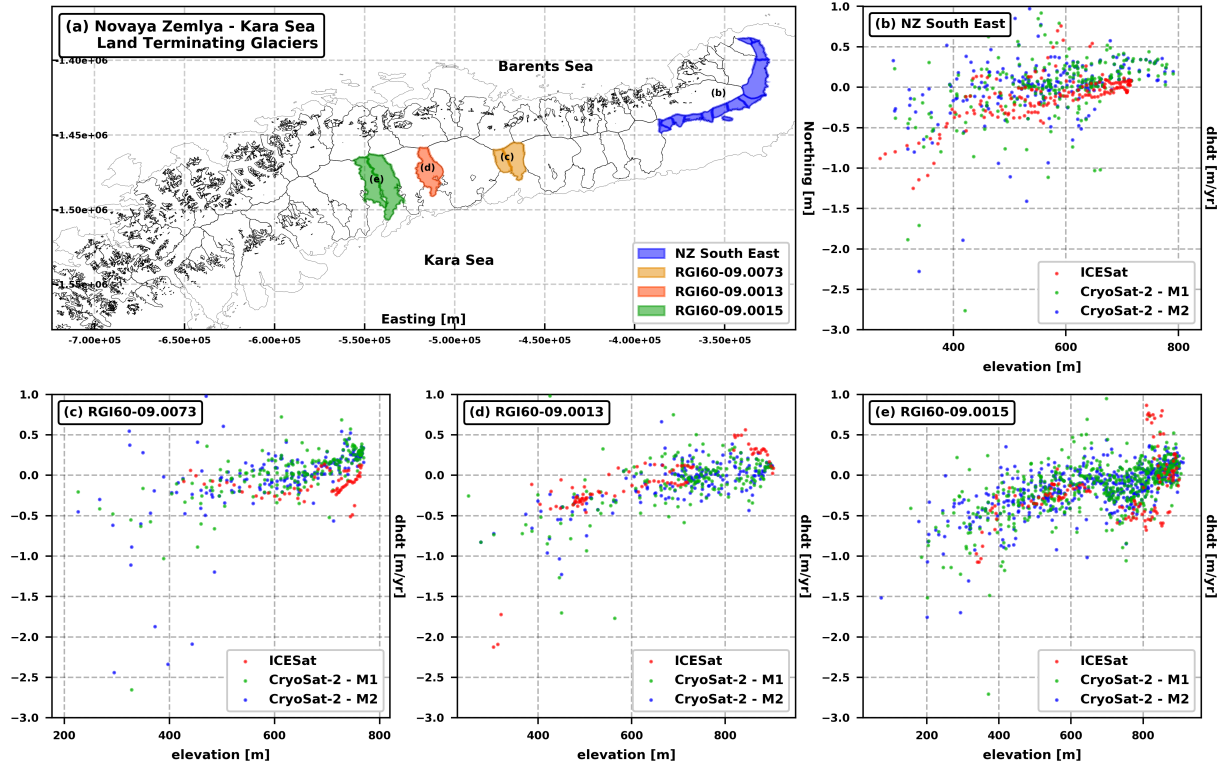


Figure 3.9: Elevation Vs Elevation Changes calculated for the major land-terminating glaciers facing the Kara Sea calculated using ICESat, CryoSat-2 - M1, and CryoSat-2 - M2. (a) Novaya Zemlya Glaciers, (b) NZ South East Glaciers, (c) RGI60-09.0073, (d) RGI60-09.0013, (e) RGI60-09.0015. Glaciers with not available name are identified using the relative Randolph Inventory ID.

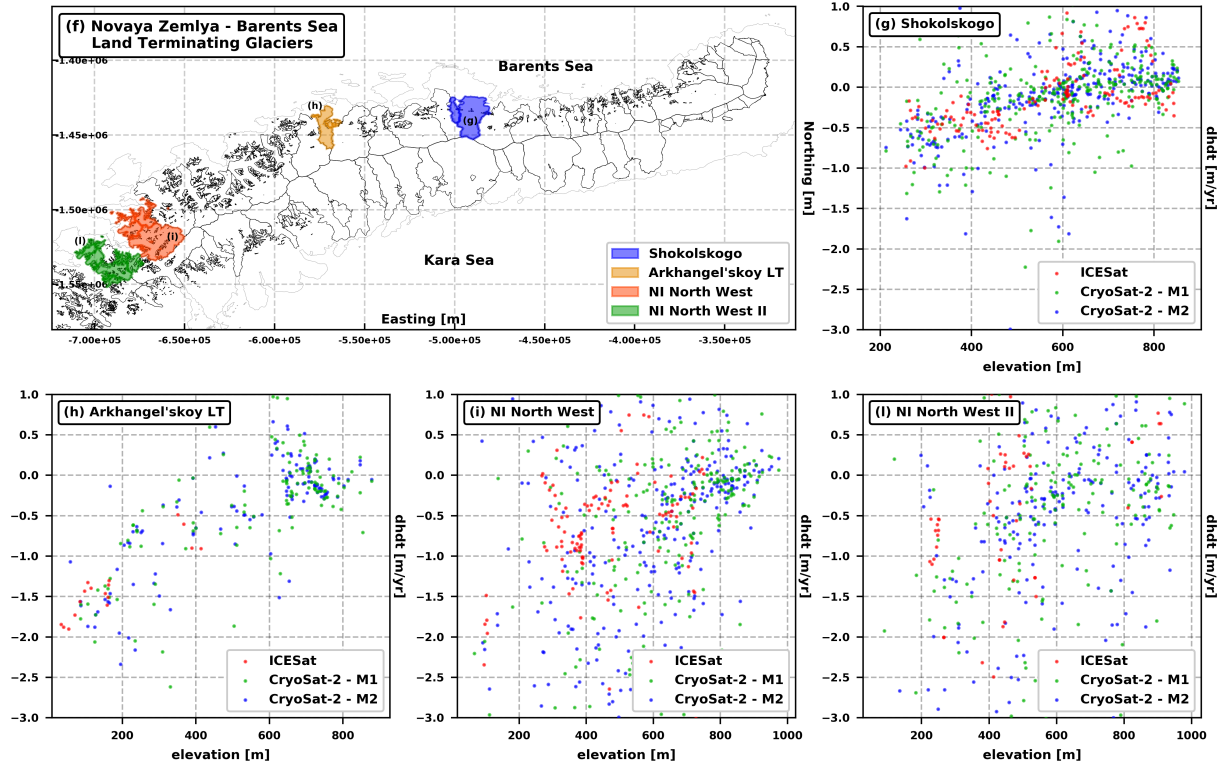


Figure 3.10: Elevation Vs Elevation Changes calculated for the major land-terminating glaciers facing the Barents Sea calculated using ICESat, CryoSat-2 - M1, and CryoSat-2 - M2. (a) Novaya Zemlya Glaciers, (b) NZ South East Glaciers, (c) RGI60-09.0073, (d) RGI60-09.0013, (e) RGI60-09.0015. Glaciers with not available name are identified using the relative Randolph Inventory ID.

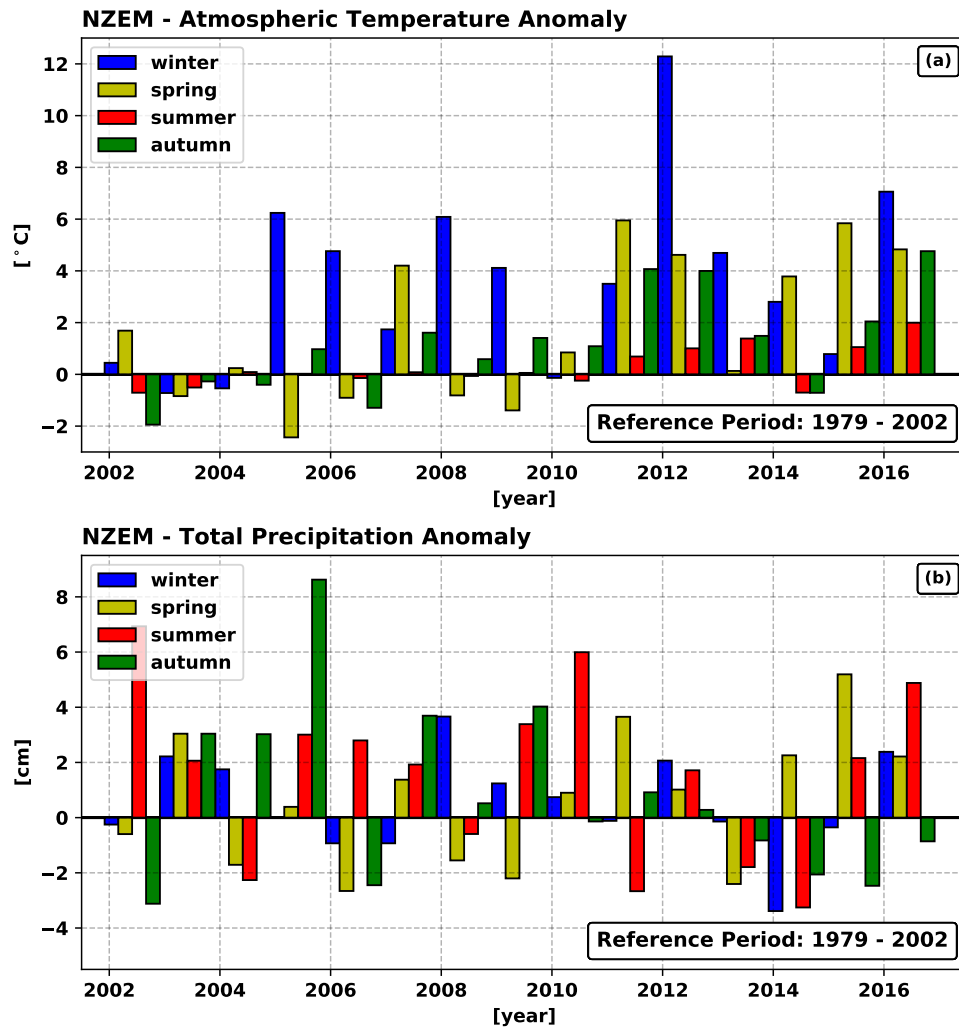


Figure 3.11: (a), Seasonal Atmospheric Temperature Anomaly (ERA/Interim - monthly means 2 meters temperature) calculate using the interval between 1979 and 2002 as a reference period. (b), Total Seasonal Precipitation (ERA/Interim - Total Precipitation Synoptic Monthly Means) Anomaly calculated using the interval between 1979 and 2002.

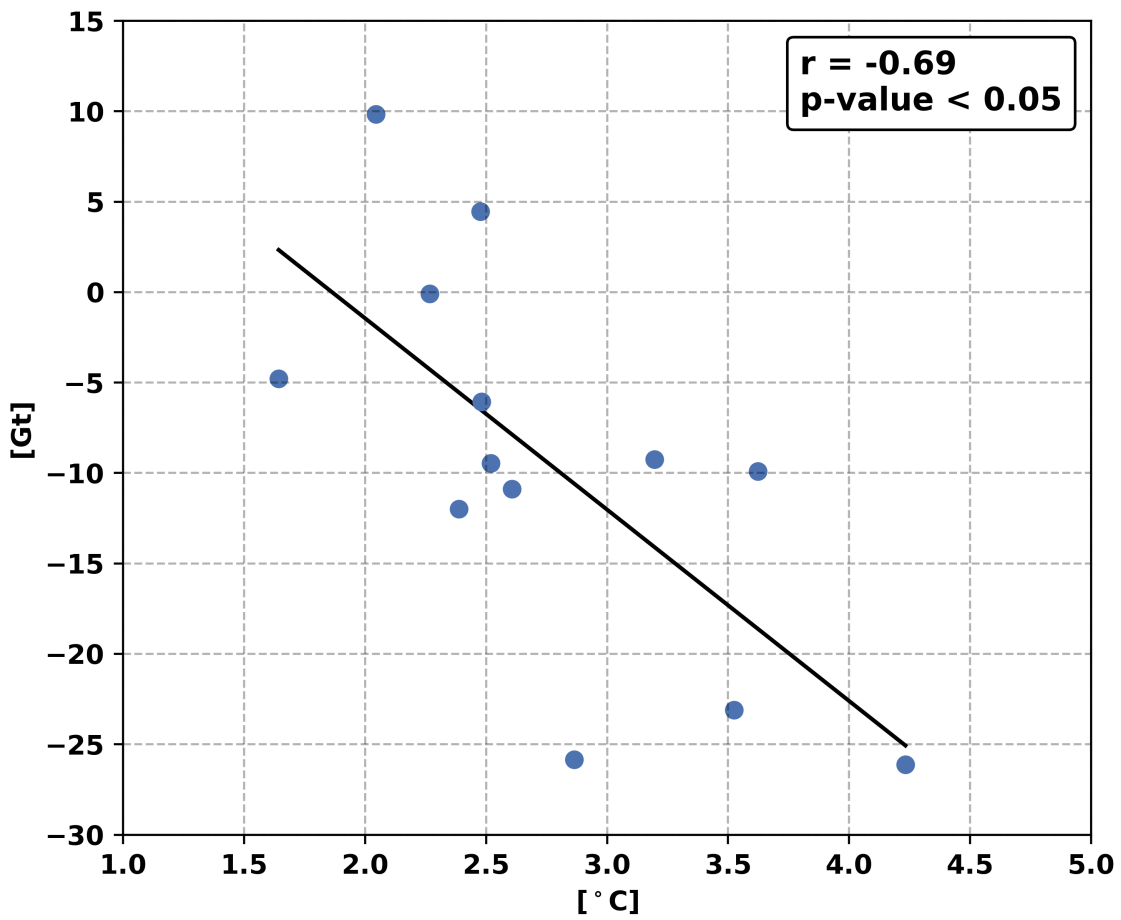


Figure 3.12: Comparison between mean summer temperature (JJA) from ERA/Interim and annual mass balance from GRACE for the time period 2002 – 2016.

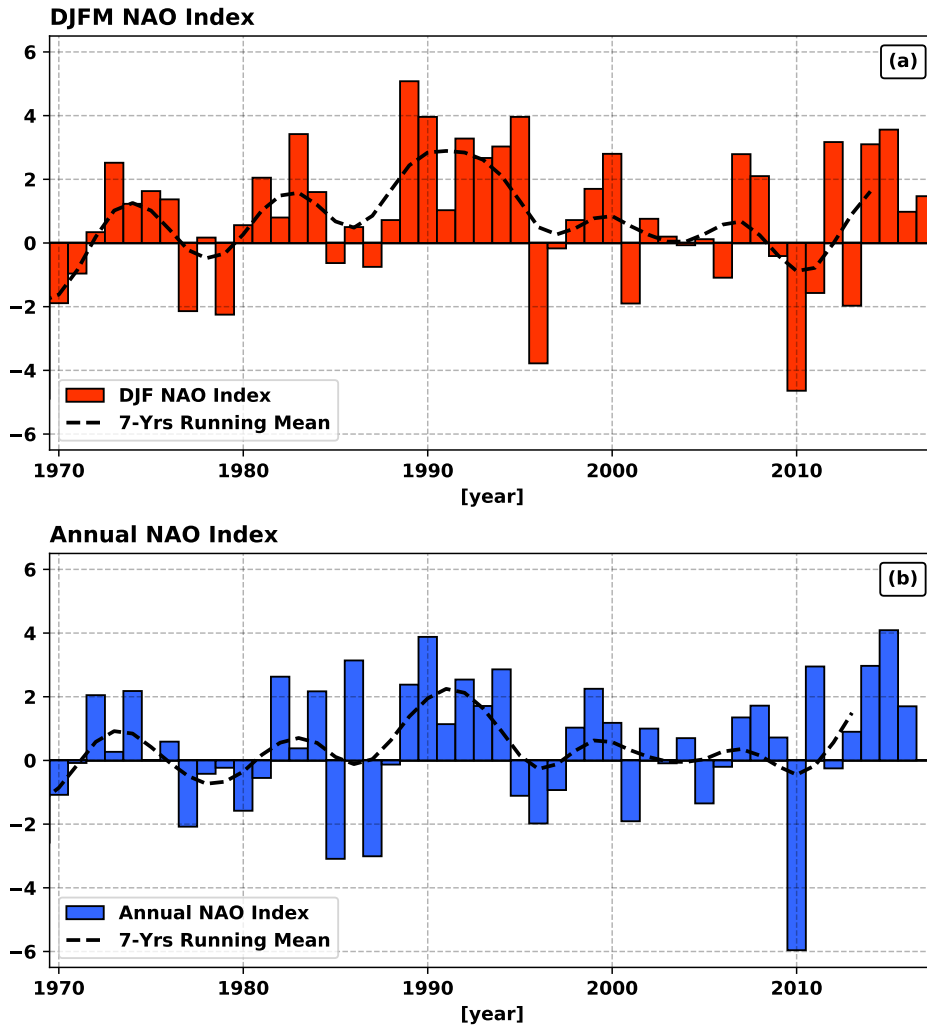


Figure 3.13: Time series of (a) winter North Atlantic Oscillation Index (DJFM NAO), and (b) Annual North Atlantic Oscillation Index (Annual NAO). The black dashed lines represents the smoothed version of the indices time series obtained using a seven-year moving average filter applied to to remove low-frequency variability and assess annual and decadal relations.

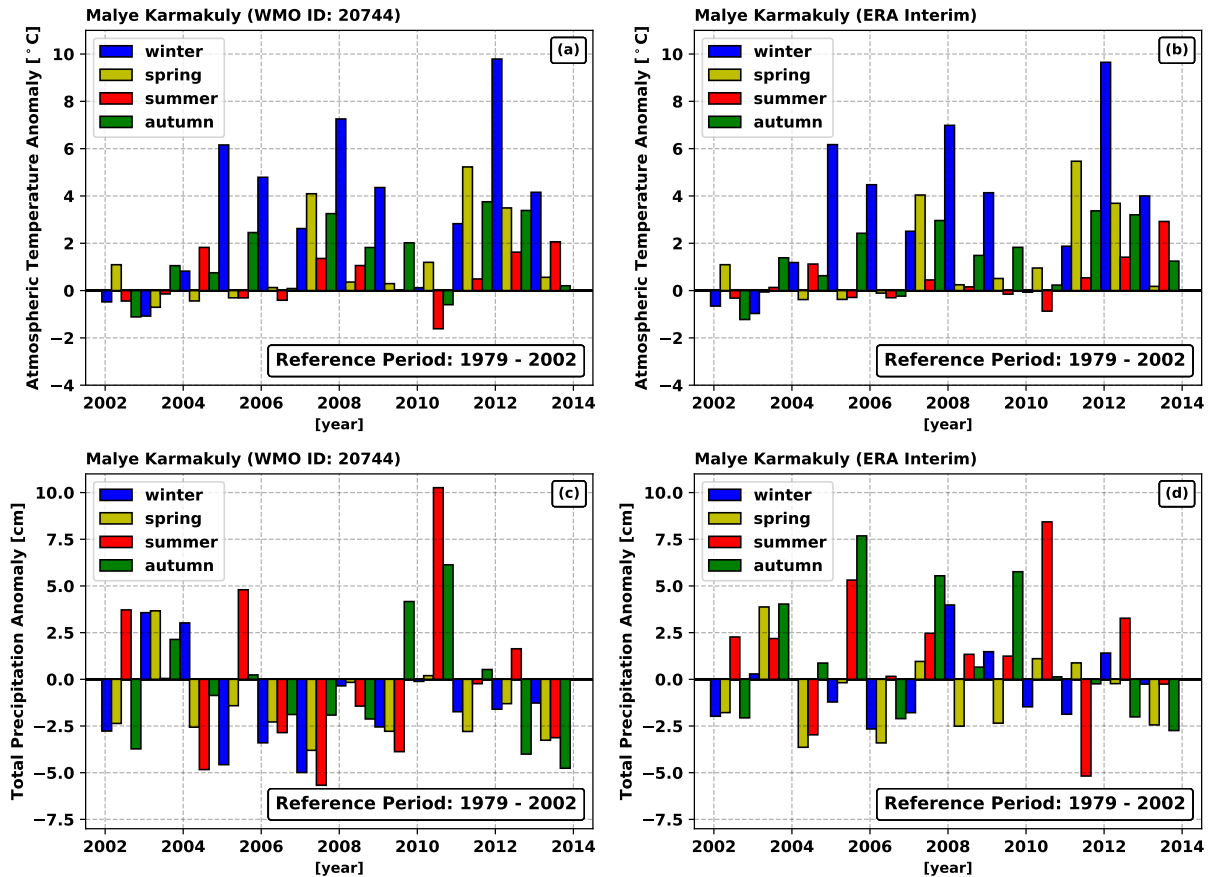


Figure 3.14: Validation of Surface Temperature and Total Precipitation calculated using ERA/Interim with direct observation from the weather station located at Malye Karmakuly (NZEM) provided by the World Data Centre Baseline Climatological Data Sets. (a, c) Atmospheric Temperature and Total Precipitation measured by the Weather Station at Malye Karmakuly. (b, d) Atmospheric Temperature and Total Precipitation employing data from ERA/Interim linearly interpolated at the Malye Karmakuly station location. ERA/Interim correctly reproduces monthly/seasonal surface temperature. Seasonal total precipitation evaluated using the two datasets show instead different patterns. This difference is probably related to the systematic underestimation of solid precipitation by the climatic station.

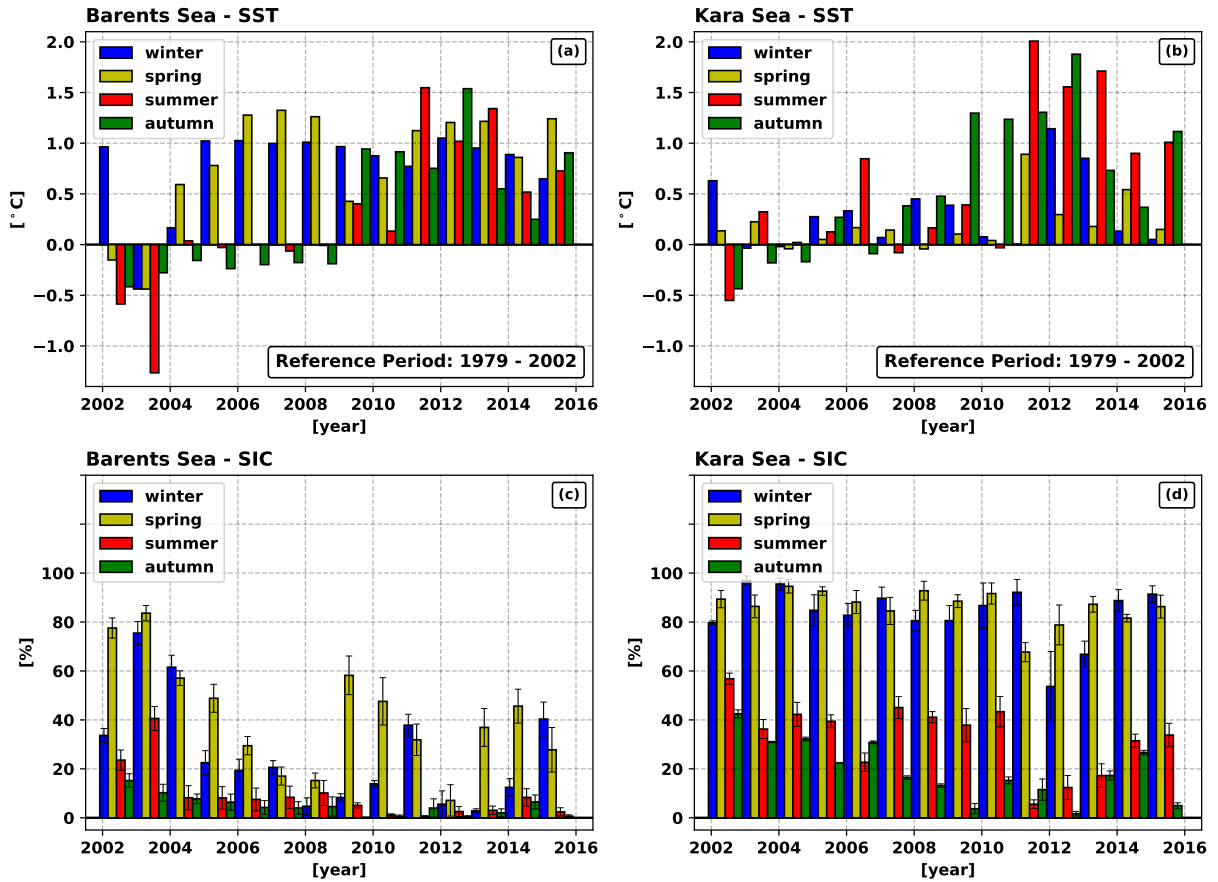


Figure 3.15: Sea Surface Temperatures (SST) and Sea Ice Concentration (SIC) calculated for the Barents Sea and the Kara Sea Coasts. (a, b) SST expressed as seasonal anomalies calculated with respect the time period 1979 - 2002. (c, d) SIC expressed as percentage of the total coastal area covered by sea ice. The black error bars are

Chapter 4

Water Balance of the Indus River Basin between 2002 and 2012

We use time series of time-variable gravity from the NASA/DLR Gravity Recovery and Climate Experiment (GRACE) mission, coupled with outputs from the Water Balance Model (WBM), to study the hydrological cycle of the Indus River Basin between April 2002 and December 2012. We evaluate the average contribution of the runoff generated upstream to the total runoff available at low elevations during summer. We find that, on average, the Upper Indus Basin provides the Lower Basin a total of 81.0 ± 11 Gt of water during the summer months. Meltwater (snowmelt plus glacier melt) is responsible for 65% of the total runoff while the remaining 35% comes from direct runoff of liquid precipitation. We compare river discharge estimates by WBM with multiple ground and remote-sensing observations. Our results show that the model captures the seasonal and inter-annual variability in the river flux signal accurately. However, the river flow during summer is either strongly underestimated or overestimated by the model depending on the climatic forcing used to constrain precipitation and surface temperature. We compare precipitation and temperatures used to force WBM with ground observations and observe large discrepancies at elevations above

2,000 m. In particular, gridded data tend to underestimate mean temperature, and to overestimate summer precipitation. These results suggest that the limited ability of gridded data products to reproduce the highly variable climatic conditions in mountainous environments constitutes the primary source of uncertainty for estimates obtained employing hydrological modeling.

4.1 Introduction

The High Mountains of Asia (HMA) glaciers play a critical role in the water cycle of Asia's main river basins. The contribution to river runoff generated upstream by meltwater from glaciers and snow is crucial to sustain the life of more than 1 billion people in the downstream regions. Water stored in snow and glaciers is the main contributor to river runoff during the summer season and extended drought periods when precipitations are scarce [Pritchard, 2017]. Glaciers of Central Asia are retreating and losing mass as a result of climate change [Bolch et al., 2012, Immerzeel et al., 2013, Jacob et al., 2012b], and water stress is expected to intensify as a result of these changes [Huss and Hock, 2018, Laghari et al., 2012, Lutz et al., 2014]. The glacier mass loss will increase during the twenty-first century [Vaughan et al., 2013, Radić et al., 2014]. A declining river discharge, together with a rising water demand caused by increasing population, will enhance the risk of water stress, producing social instability, conflicts, migrations, and state collapse [Laghari et al., 2012]. Assessing the ongoing and future hydrological impact of the glacier mass loss is crucial in order to project future availability of water resources in the region. It is thus necessary to determine the exact partitioning of the total river discharge generation between precipitation and meltwater. However, achieving this goal is hampered by the inherent difficulty of accessing high elevation areas to collect in-situ observations of glacier mass balance and river discharge. Ground observations, if available, are usually sparse and biased towards low elevations. Ex-

isting estimates, for this reason, are mainly based on model simulations that are affected by large uncertainties due to their limited ability to reproduce the physical processes driving hydrological changes in mountainous environments. The lack of understanding of the hydrological regimes in the upstream environments remains, for this reason, one of the main source of uncertainty in assessing the impact of climate change in these regions [Lutz et al., 2014].

Satellite observations provide a suitable tool to obtain a widespread characterization of regional hydrological changes, at a uniform sampling, and with a known precision over long periods of time. They can thus be used to validate and improve existing models to obtain a comprehensive assessment of the current state and future evolution of glaciers and river discharge in the region. In this study, we use time series of time-variable gravity from the Gravity Recovery and Climate Experiment (GRACE) mission to evaluate changes in total water storage (TWS) in the Indus River Basin (IB). We use a mascon approach to study the temporal TWS anomalies in the region with the aim of evaluating the contribution by the upstream areas to the entire river basin's hydrological cycle.

In order to partition the TWS anomaly between different hydrological variables, we compare monthly observations by GRACE with independent estimates of precipitation (P), evapotranspiration (ET), runoff (R), and total water storage (TWS) from the Water Balance Model (WBM) developed at the University of New Hampshire. We analyze TWS estimates obtained from WBM by using two different climatic forcings and we compare them with GRACE with the aim of determining which of the two forcings provides the most realistic reproduction of the TWS temporal variability.

Afterwards, we provide a further evaluation of the model's outputs by comparing the hydrological variables simulated by WBM with multiple datasets of remote-sensing and ground observations. Specifically, we compare the simulated river runoff with monthly river discharge measurements available in the upstream areas for the four main tributaries located in the Pakistani territory and with total river discharge measured at the river's mouth. We

also compare monthly average surface temperatures and total precipitation with ground observations available within the entire basin in order to investigate the main sources of error that limit the model's performance in the region.

4.1.1 Study Region

The Indus River Basin is the twelfth largest river in the world [Frenken, 2012]. The basin has a total area of 1.12 million km^2 , shared by four countries : Pakistan (47%), India (39%), Afghanistan (6%), and China (8%). The river originates from the Manasarovar lake in China at an elevation of 5,500 m and defines the boundary between the Great Himalaya and the Hindu Kush and Karakoram mountain ranges (HKH). The river has a total length of 3,200 km, stretching from the Himalayan region, passing through the dry alluvial plains of Pakistan and India and finally flowing into the Arabian Sea. The river has several major tributaries: the Kabul, the Indus, the Jhelum and the Chenab on the West and the Ravi, the Beas and the Sutlej on the East (see Figure 4.1). The western rivers are mainly fed by seasonal snow and glacier melt and reach their maximum flow between the spring and summer seasons. Eastern rivers reach their flow peaks in summer as well when the monsoons transport abundant liquid precipitation in their catchment areas [Lutz et al., 2014, Young and Hewitt, 1990]. The Indus River is the main tributary and controls more than half the total flow.

The basin does not exhibit a uniform climate. It varies from sub-tropical arid and semi-arid to temperate sub-humid on the plains of Sindh and Punjab provinces to alpine in the upper part of the basin. Annual precipitation originates from two main sources: the south-eastern monsoons during summer and moisture transported by the westerly jet stream during winter. Average annual precipitation ranges between 100 and 450 mm per year in the lowlands with maximum precipitation rates above 2,200 mm/yr above 2,000 meters [Frenken, 2012]. In the arid lower areas monthly mean temperatures during winter (December to

February) vary from 14°C to 20°C while temperatures above 40°C are instead registered between March and June. Slightly lower temperatures are registered in the upper plains where mean temperatures between 23°C and 49°C are registered in summer and between 2°C and 23°C in winter [Frenken, 2012].

The Upper Indus Basin (UIB) is located at elevations above 2,000 m a.s.l. and represents 40% of the total river basin area. The UIB hosts the largest glacier system of the planet outside the polar regions. According to the Randolph Glacier Inventory the basin hosts a total glaciers area equal to 29,000 km^2 that is mainly located at elevations between 4,000 and 5,500 meters [Young and Hewitt, 1990, Pfeffer et al., 2014]. Snow covers a total area one order of magnitude larger than the total glacier area [Hewitt, 2011]. The climate in the UIB is largely influenced by winter monsoons that transport abundant precipitation from the Mediterranean and the Caspian Sea [Aizen et al., 2000]. The Himalayan mountain ranges limit the intrusion of the summer monsoons, whose influence decreases toward North-West [Fowler and Archer, 2006].

The Lower Indus Basin (LIB) is one of the most densely populated regions on the planet. The current population amounts to around 237 million people with an extremely high growth rate. Available projections indicate an almost doubling of the total population by 2050 [Frenken, 2012, Laghari et al., 2012]. The local economy is largely based on the cultivation of wheat, rice, cotton and sugarcane. The major agricultural zones are located in the Pakistani and Indian provinces of Punjab and Sindh. The water demand to support agricultural activities is extremely high and not sustainable by the dry climate characterizing the region. Precipitations mainly occur in summer and are not available for crop production or recharge to groundwater because of rapid runoff and strong evapotranspiration fluxes [Frenken, 2012]. Water supply from the UIB is therefore critical to sustain agricultural activities downstream.

In the beginning of the twentieth century local governments started the construction of a complex hydraulic network of canals, barrages and dams with the aim of providing water to

the largest possible portion of potential irrigable land. With a total area of $228,694 \text{ km}^2$, the Indus Basin Irrigation System (IBIS) is, today, the largest irrigation system of the world (See Figure 4.2). The system is largely fed by runoff generated in the upper basin and regulated by the Tarbela and the Mangla dams [Frenken, 2012].

In the current climate, river runoff reaches its peak during the summer months when melting of seasonal snow and glaciers approaches its maximum [Fowler and Archer, 2005]. Immerzeel et al. [2010] used high resolution hydrological modeling to assess the contribution by runoff from the upstream areas to the total runoff available within the basin. They estimated that river runoff generated in the UIB, largely by snow and glacier melt, is on average equal to 151% of the total runoff naturally generated in the downstream areas as the difference between annual precipitation and evapotranspiration. They also found that glacier melt is on average responsible for 40% of the total meltwater and attributed the remaining 60% to snowmelt. Similar results were obtained by Bookhagen and Burbank [2012] who, using a mixture of remotely sensed observations and hydrological modeling, attributed 60% of the total annual runoff generated within the UIB to snow and glacier melt.

Increasing atmospheric temperatures are contributing to glacier shrinking globally [Gardner et al., 2013]. Available observations in the UIB indicate heterogeneous glacier changes in the region. Glaciers are in fact losing mass at high rates in the Himalayas, while stability or even mass gain is observed in the Hindu Kush and Karakoram ranges [Bolch et al., 2012, Kääb et al., 2012, Brun et al., 2017]. These contrasting glacier behaviors have been generally associated to the different climatic and meteorologic mechanisms driving the glacier mass balance in the two regions [Yao et al., 2012, Young and Hewitt, 1990]. The Himalayan glaciers accumulate mass during summer; accumulation and ablation seasons are therefore contemporary. Accumulating mass during summer, these glaciers are highly sensitive to the long-term increase in atmospheric temperatures. Warmer atmospheric conditions promote an increase in liquid precipitation. Liquid precipitation is more exposed to direct runoff and

contribute less to glacier accumulation [Young and Hewitt, 1990]. At the same time, it affects the glaciers albedo and promotes longer and more intense ablation seasons [Fujita, 2008]. The Karakoram and the Hindu Kush regions are characterized by a different climate. They receive abundant solid precipitation during winter while summers are on average dry [Archer and Fowler, 2004, Fowler and Archer, 2005, Palazzi et al., 2013]. The anomalous behavior of glaciers in these areas received increasing interest by the scientific community during the last decade. The so-called "Karakoram Anomaly" has been associated to particular climatic and meteorological conditions characterizing the region [Yao et al., 2012, Fowler and Archer, 2005, Forsythe et al., 2017, Kapnick et al., 2014]. Fowler and Archer [2005] analyzed ground observations available in the region for the time period between 1961 and 1999. They observed a significant increase in winter, summer, and annual precipitation. Temperatures increased during winter and significantly decreased during summer, indicating that stable glacier conditions might have been caused by an increasing trend in annual precipitation and cooler summers promoting shorter ablation seasons. The decrease in summer temperatures has, in general, been associated to more frequent intrusions of summer monsoons through the Himalayan ranges contributing to a significant rise in seasonal cloud coverage and more abundant precipitation [Young and Hewitt, 1990, Forsythe et al., 2017, Fowler and Archer, 2006].

Available glacier mass balance estimates are mainly based on small and sparse data samples. The assessment of the current state and future evolution of glaciers in the UIB remains, therefore, extremely challenging. The projected increase in temperatures during the next decades will have a serious impact on the runoff generation and the downstream water supply [Immerzeel et al., 2010]. Model predictions indicate that, in the short term, river runoff will rise because of glacier recession and consequent increase in meltwater production during the summer season. Annual runoff will increase up to a certain maximum beyond which it will decrease, because the reduced glacier area will no longer be able to support rising meltwater volume [Lutz et al., 2014, Huss and Hock, 2018].

The increasing water demand, together with low irrigation efficiency, make the Indus basin one of the most depleted regions in the world. Currently, almost 95% of the available water resources are employed for irrigation and hydropower generation [Frenken, 2012]. Today, 53% of irrigation water is extracted from the surface while ground water accounts for the remaining 47% [Laghari et al., 2012]. During the last decades, groundwater extraction increased at high rates contributing to the rapid decline of the water table in the region [Rodell et al., 2009]. During the next century, groundwater depletion will increase the risk of water shortages. This process, in turn, will increase the dependency of the region on runoff generated upstream and will make the local economy highly susceptible to the reduction of the river flow. Assessing the current state of water reservoirs in the UIB is therefore crucial in order to evaluate their future evolution and to help local governments to implement hydrological planning and water resource management and to reduce the risk of water stress in the entire region.

4.2 Data and Methods

4.2.1 Time Variable Gravity and Mascon Inversion

We study changes in total water storage (TWS) over the Indus River Basin using time-variable gravity from the Gravity Recovery and Climate Experiment (GRACE). GRACE was a joint operation by the National Aeronautics and Space Administration (NASA) and the German Aerospace Center (DLR) that measured changes in the Earth’s gravitational field between 2002 and 2017 [Tapley et al., 2004]. Here, we use 132 monthly GRACE Release-5 (RL05) gravity field solutions provided by the Center for Space Research at the University of Texas (CSR) for the period April 2002-December 2012 [Tapley et al., 2004, Bettadpur, 2012]. Monthly gravity field anomalies from CSR are distributed in the form of

fully-normalized spherical harmonics up to degree and order 60. We replace C_{20} coefficients with more accurate estimates from the satellite laser ranging missions (SLR) [Cheng et al., 2013]. We account for the variation of degree-1 using coefficients calculated from a combination of GRACE coefficients and ocean model outputs following Swenson et al. [2008]. We include an additional pole tide correction to remove the long-period pole tide signals not included in the standard corrections [Wahr et al., 2015]. We remove the effects from Glacial Isostatic Adjustment (GIA), i.e. the viscoelastic response by the solid Earth from changes in ice loading since the last glacial maximum (LGM), using coefficients from A et al. [2013]. We isolate the gravity signal associated to changes in water storage across each of the considered river basins by subtracting from the gravity anomaly the signal contribution generated by changes in terrestrial hydrology in the surrounding areas (i.e. groundwater, soil moisture and snow cover) using TWS estimates from the Global Land Data Assimilation System 2 (GLDAS-2) model, version NOAH-3.3 [Rodell and Beaudoing, 2016]. We calculate mass change time series employing the least squares fit mascon approach presented in Jacob et al. [2012b]. We cover the river drainage basins with one or more mascons. Each mascon is a 3.1-degree diameter equal-area spherical cap [Pollack, 1973, Farrell, 1972, Sutterley et al., 2014]. The mascon configuration employed in the calculation is presented in Figure 4.3. We use additional mascons to cover the areas surrounding the IB in order to minimize the effect of groundwater and glacier mass change in those region on our final estimates. For each mascon, we calculate a set of Stokes coefficients associated to a unitary mass equivalent to one centimeter of water uniformly distributed over the mascon surface, which we smooth with a 150 km Gaussian function [Jacob et al., 2012b]. We calculate the monthly mass anomaly associated to each mascon by simultaneously fitting the mascons Stokes coefficients to the GRACE monthly coefficients corrected for GIA and the Terrestrial Hydrology [Jacob et al., 2012b]. We express the total uncertainty affecting our mass change estimate by summing in quadrature estimates of inaccuracy terms related to: GRACE measurement errors; glacial isostatic adjustment correction; hydrology correction; leakage error caused by the

assumption that the mass changes are uniformly distributed within each mascon. We calculate GRACE measurement errors following Wahr et al. [2006]. GIA and hydrology trend uncertainties are calculated as in Jacob et al. [2012b]. In order to evaluate the leakage error, we apply the mascon inversion to a realistic synthetic mass field generated using monthly TWS from GLDAS-2. The model does not simulate regional trends, associated to the glacier mass loss in the upstream areas and to the groundwater depletion over the plains of northern India, Pakistan, and Bangladesh, detectable in the GRACE fields [Tiwari et al., 2009]. We estimate these two components as reported in Chapter 2 and we add them to the synthetic field. We use the standard deviation of the monthly mascon fit error as an estimate of the probable range for each extracted mascon value and we include it in the error budget [Sutterley et al., 2014].

4.2.2 Water Balance Model

We use precipitation (P), evapotranspiration (ET), runoff (R), and total water storage (TWS) estimates from the Water Balance Model (WBM) developed at the University of New Hampshire, Durham [Vörösmarty et al., 1998]. WBM is a variable-scale, gridded model that simulates both the vertical exchange of water between the ground and the atmosphere, and the horizontal transports of water through runoff and stream networks. In addition to the natural water cycle, WBM can simulate human use and management of water, such as irrigation withdrawals and water transfers through canals. WBM simulates the regional TWS as the sum of several variables representing a set of water reservoirs located above and below ground [Grogan et al., 2017]. One of the core components of WBM is the Water Transport Model. This algorithm drives the flux of surface runoff downstream from one grid cell to another, simulating a river network. WBM also has the capability to track the different components of river runoff categorized according to their original source: rain water, snowmelt, and glacier melt [Grogan et al., 2017]. Here, we use WBM outputs, provided at

0.1° resolution, obtained using precipitation and surface temperature from two independent sources: the ERA/Interim Reanalysis model [Dee et al., 2011] and the APHRODITE project [Yatagai et al., 2012].

In order to consistently compare the WBM estimates of TWS with GRACE, we convert the monthly gridded fields into spherical harmonics and obtain the regional time series by applying the mascon inversion to each of the obtained fields. We apply the same processing to the monthly estimates of total precipitation and evapotranspiration. We estimate the runoff generated within each of the considered basins employing the water balance equation presented below:

$$R_{out} = P - ET - \Delta TWS_{GRACE} + R_{in} \quad (4.1)$$

Where, R_{out} represents the cumulative runoff leaving the basin, P and ET are the cumulative time series of precipitation and evapotranspiration, ΔTWS_{GRACE} is the monthly water storage anomaly measured by GRACE and R_{in} is the cumulative runoff entering the basin. We compare the cumulative time series of Precipitation (P) and Evapotranspiration (ET) with monthly TWS anomalies measured by GRACE and estimate the total runoff (R) generated within the specific basin. We evaluate the Runoff estimated using equation (4.1) with the same quantity simulated by WBM employing the Water Transport Model at the interface between the UIB and the LIB (see Figure 4.2). We apply the same steps to the monthly time series relative to both the Upper and the Lower basin with the aim of quantifying the average summer contribution by the upstream regions to the total runoff available downstream.

The river discharge within the Indus River Basin has a well defined seasonal variability. The water flux is at a minimum during winter, starts rising during spring and reaches its peak at the end of summer when snow and glacier melt occur at their maximum rates. The largest exchange of water mass between the UIB and the LIB takes place, therefore, between May and November. We evaluate the average summer total contribution by the UIB to the LIB

runoff following the steps presented below:

- We remove the long-term trend from each of the variables presented in equation (4.1);
- We calculate the average monthly values (climatology) of each of the considered time series;
- We calculate the average mass change associated to each of the considered components as the difference between the average values assumed in November and in May;
- We substitute the obtained mass changes in (4.1) and calculate the mean summer runoff from the UIB to the LIB.

4.2.3 Climatic Forcing

ERA/Interim

ERA-Interim [Dee et al., 2011] is a global atmospheric reanalysis product with an atmospheric model and assimilation system, produced by the European Centre for Medium-range Weather Forecasts (ECMWF) providing data from 1979 to present. Here we use monthly mean of daily means estimates of total precipitation and 2-meters temperatures available at <http://apps.ecmwf.int/datasets/data/interim-full-moda/>. Original data are provided at a native spatial resolution of 0.75° , which are re-gridded on the 0.1° grid resolution used to run WBM.

APHRODITE

Asian Precipitation-highly Resolved Observational Data Integration Towards Evaluation of Water Resources (APHRODITE) is a high resolution dataset providing daily estimates of

total precipitation and surface temperatures for the time period extending from 1951 to 2007. The dataset was developed by a consortium between the Research Institute for Humanity and Nature (RIHN) Japan and the Meteorological Research Institute of Japan Meteorological Agency (MRI/JMA). Temperature and precipitation estimates are provided at a 0.25° latitude-longitude resolution and are the result of the interpolation of measurements by a dense network of meteorological stations using the distance-weighting interpolation algorithm described in Shepard [1968]. Further details about the dataset development are provided in Yatagai et al. [2012]. We use the Monsoon Asia dataset covering the area between 60.0E – 150.0E , 15.0 – 55.0N re-gridded on the 0.1° grid resolution used in WBM.

4.2.4 Other Datasets

Meteorological Stations

We employ ground observations from 55 meteorological stations available within the entire river basin with at least one year of data available during the time period analyzed in this study. We used data provided by three different organizations: the Pakistani Meteorological Department (PMD) (5 stations), the Pakistan Karakorum Surface Meteorology and Radiation Data Set by the EV-K2-CNR research program (2 stations) available at (<https://data.eol.ucar.edu/dataset/76.200>) [EV-K2-CNR, 2011], the Global Surface Summary of the Day (GSSOD) and the Global Historical Climate Network (GHCN) (48 stations). The last two datasets are provided by the US National Centers for Environmental Information (NCEI) and are available at (<https://gis.ncdc.noaa.gov/maps/ncei/cdo/daily>). We compare monthly time series of Precipitation and Surface Temperatures with values from ERA/Interim and APHRODITE linearly interpolated at station locations. The considered network of climatic stations provide a uniform coverage of the entire river basin (see Figure 4.2). However, only 8 of the 55 stations are available at elevations above 2000 m. The highest

station, Shiquanhe (89.0°E, 32.4°N)) is located in the North-Eastern the UIB at a elevation of 4,280 m. On the one hand, given the extremely fast variability of climatic conditions in the region, a data sample of this size is too small and too sparse to be used for extrapolation purposes. On the other hand, measurements by the 55 climatic stations can be used to validate surface temperature and monthly precipitation in ERA Interim and APHRODITE.

River Flow Data

We use monthly river flow data provided by the Water and Power Development Authority of Pakistan (WAPDA). Total monthly river discharge time series were provided for the time period between 1971 and 2009 for the four main tributaries of the Indus River flowing on the Pakistani territory: Indus, Kabul, Chenab and Jhelum (see Figure 4.2). We also use monthly discharge values measured at the Indus River delta (monthly outflow into the ocean) extracted from the Global River Flow and Continental Discharge Dataset (GR-CDD) available at (<http://www.cgd.ucar.edu/cas/catalog/surface/dai-runoff/>). This second dataset provides monthly total discharge values evaluated at the Delta of the Indus River for the time period between 1936 and 2000. A detailed description of the datasets can be found in Dai and Trenberth [2002] and in Dai [2016]. Even though the GRCDD discharge estimates are not available for the time period considered in this study, they can still provide useful information when comparing the different estimates in terms of average monthly values (When we compare the different estimates in terms of their climatology).

Satellite Altimetry

We use monthly river elevation data from the Database for Hydrological Time Series of Inland Waters (DAHITI). The DAHITI project provides water level time series of lakes, reservoirs, rivers, and wetlands derived from multi-mission satellite altimetry for hydrological

applications [Schwatke et al., 2015]. We find a total of 12 virtual stations (intersections between satellite tracks and river streams) available along the Indus River within the latitude-longitude range: 68.0°E–71.0°E, 24.0°–31.0°N. The virtual station located at the highest elevation (487 m) reports monthly estimates of water elevation change measured at the Tarbela Dam (34.0°E–72.7°E) (see Figure reffigure1b).

4.3 Results

4.3.1 Comparison with GRACE

Total water storage time series for the UIB and the LIB calculated by applying the mascon inversion are presented in Figure 4.5(a) and Figure 4.5(c). The linear long-term trends have been removed from all the time series. The comparison shows a good agreement between total water storage anomalies measured by GRACE and those simulated by WBM using ERA Interim and APHRODITE as climatic forcing. WBM correctly simulates the annual and inter-annual variability of the TWS extracted from the monthly gravity anomalies. This result is confirmed by the Neyman-Pearson correlation coefficient. In the UIB, both WBM outputs correlate well with GRACE. We find $R=0.81$ in the case of WBM/Era Interim and $R=0.78$ in the case of WBM/APHRODITE. We do not obtain the same results in the case of the LIB. Here, we observe a good correlation between GRACE and WBM/ERA Interim, $R=0.78$, while we find a significantly lower correlation value in the case of WBM/APHRODITE, $R=0.35$. In terms of the amplitude of the TWS signal, WBM/ERA Interim provides again a better match with GRACE. We find that the root mean square value of the difference between the simulated and the measured TWS time series passes from 37 to 29 Gt in the case of the UIB and from 22 to 18 in the case of the LIB. In both basins, therefore, the agreement with GRACE improves by 20% when using ERA Interim. Figure 4.5(b) and Figure 4.5(d)

show the climatology (average monthly values) calculated from the time series represented in the left column. These results show that WBM/ERA Interim captures the amplitude and the timing of the local TWS anomaly accurately especially in the case of the LIB. In the case of the UIB, the amplitude of the average signal is captured just as well, but with a one-month lag between GRACE and WBM/ERA Interim. WBM/APHRODITE performs well in the case of the UIB, in the case of the LIB, however, the simulated average annual variability does not match with GRACE with respect to amplitude and timing.

The comparison presented in Figure 4.5 reveals a different average annual variability in TWS within the UIB and the LIB. The UIB accumulates mass during the winter season and the regional mass anomaly reaches its maximum in May. From this moment, the mass anomaly starts decreasing, reaching its minimum in December. This variability is consistent with the climate of the region. The accumulation of mass between the winter and the spring seasons is related to the influx of precipitation (mainly solid precipitation) by the Westerly winter monsoons. The decline in storage, observed during summer, is instead related to the mass loss caused by snow and glacier melting and the increase in evapotranspiration fluxes observed by WBM during the same time period. The LIB shows a different temporal variability. In this case, after a short phase of mass gain between January and March, the average annual anomaly becomes negative and reaches its negative peak between May and June. The LIB mass anomaly starts rising again in June and reaches its maximum value in September, at the end of the Monsoon Season. The binomial variability detectable in the case of the LIB highlights that the mass anomaly of the lower basin is affected by both summer precipitation and influx of water from the UIB.

4.3.2 Comparison with River Gauges

Figure 4.5 shows the result of the comparison between monthly discharge measured by the river gauges provided by WAPDA and discharge estimated by WBM. The location of each station is presented in Figure 4.5(a). WBM correctly reproduces the seasonal and inter-annual variability of the river discharge. We find correlation values between river gauges and WBM above 0.75 when using both ERA Interim and APHRODITE as climatic forcing. At the same time, the comparison shows clearly that monthly discharge estimates obtained using WBM/APHRODITE significantly underestimate the discharge values measured by the river gauges. WBM/ERA Interim provides a better approximation of the measured discharge values, with monthly mean error (μ_{error}) below 1 Gt in the case of Jhelum, Chenab and Kabul. A large discrepancy is instead observed in the case of the Indus River, where WBM/ERA Interim overestimates the summer discharge by 50% between August and September.

4.3.3 Comparison with GRCDD

Figure 4.9 shows, in red, the averages of monthly discharge measured by the GRCDD project at the Indus River Delta between 1936 and 2000. WBM averages for the time period 2002–2012 are reported in blue and gold. WBM/Era Interim estimates that an average amount of water equal to 148 ± 6 Gt is discharged into the Arabian Sea every year. WBM/APHRODITE finds an unrealistic total of only 13 ± 1 Gt. GRCDD measurements indicate a total discharge equal to 94 ± 4 Gt. The datasets exhibit the largest difference between the months of September and October, when WBM/ERA Interim simulates a total discharge almost two times larger than the one reported by GRCDD while WBM/APHRODITE remains close to zero.

4.3.4 Comparison with Satellite Altimetry

Monthly water elevation changes are presented in Figure 4.7. WBM does not provide estimates of river level changes. We therefore normalize the monthly discharge and elevation data before the comparison. Figure 4.7 shows results from the comparison for 12 virtual stations located along the Indus River stream. Eleven of the twelve stations are located in the LIB, while only one station is available in the UIB. In all the considered cases, WBM seems to capture the seasonal variability of the river flux. Elevation and water flux time series are significantly correlated with correlation values ranging between 0.6 and 0.8 in all considered cases.

4.3.5 Water Budget

Figure 4.10 shows the results of the Water Budget calculation applied to the two WBM versions. As previously observed WBM/ERA Interim reproduces the total water storage anomalies observed by GRACE with high accuracy while WBM/APHRODITE is affected by large errors. This last comparison provides further confirmation of these results.

WBM/ERA Interim

We evaluate the average annual contribution by the UIB to the LIB hydrology following the steps presented in the Data and Methodology section. The results of the comparison are presented in Figure 4.9. Figure 4.9(a) shows the annual water budget for the UIB. The TWS anomalies measured by GRACE are shown in blue and in green, the average annual TWS anomaly measured by GRACE and by WBM/ERA Interim (These are the same average monthly values presented in Figure 4.5). GRACE measures an average mass loss between May and November equal to 96 ± 11 Gt while WBM/ERA Interim estimates a value equal

to 72 ± 9 Gt. The golden and the brown lines show the monthly averages of R estimated by WBM at the interface between the UIB and the LIB and the monthly averages of R calculated by subtracting from GRACE the cumulative time series of P and ET extracted from WBM. The two estimates show extremely good agreement, increasing our confidence in the obtained result. Table 4.1 contains the average summer mass changes attributed to the different water balance components. Between May and November, the UIB loses a total mass ranging between 96 ± 11 and 72 ± 9 Gt. During the same time period, the basin receives a total input of mass equal to 24.2 ± 12 Gt in form of liquid and solid precipitation. The mass loss is distributed between ET (39.1 ± 2 Gt) and R (81 ± 11 Gt). The cumulative runoff is, therefore, more than two times larger than both P and ET. During the summer season, the input of mass provided in form of precipitation is almost completely compensated by the increase in ET. The largest part of the mass loss occurs in the form of river discharge that transfers water from the UIB to the LIB. As previously discussed, WBM tracks the different river runoff components categorized according to their original source: rain water, snowmelt, and glacier melt. The model estimates that 65% (53 Gt) of the total runoff leaving the UIB during the summer season is composed of meltwater (26% by glacier melt and 39% by snowmelt) while the remaining 35% of liquid precipitation.

Figure 4.9(c) shows the annual mass budget evaluated for the LIB. The red and the green lines show again the average annual anomalies estimated by GRACE and WBM already presented in Figure 4.5. The brown line represents the average annual discharge estimated by WBM at the delta of the Indus River (This line represents therefore the amount of water annually discharged into the Arabian Sea). The golden line shows the average monthly runoff calculated by applying the water budget equation. In this case, we calculate the total amount of water leaving the LIB subtracting from P, ET, TWS from GRACE and the input of water from the UIB measured before. Also in this case, the two estimates show excellent agreement. On average, R in the LIB is low during the winter season, starts rising in July, and reaches its maximum between November and December. Precipitation

and Evapotranspiration values increase during summer. The cumulative values for these two variables are three to four times bigger than those observed in the UIB case. The influence of summer monsoons is thus significantly stronger on the lower basin.

The LIB gains mass during summer due to the contribution of water provided by precipitation and the input of water from the upstream regions. It is important to observe that given the amplitude of the ET signal (The mass lost through ET almost 20 Gt larger than the mass gain provided by P), the contribution provided by the runoff generated from the UIB becomes extremely important in order to allow the system to gain mass during the second part of the year (Without the contribution by the UIB, the LIB would lose mass during summer).

WBM/APHRODITE

Figure 4.9(b) and 4.9(d) and table 4.2 show the results of the same analysis performed using the WBM/APHRODITE version of the model. We observe large disagreements in both basins. TWS and R estimates by the model are extremely far from those obtained using GRACE and from those obtained using ERA/Interim as climatic forcing. TWS average monthly values not in agreement in terms of amplitude and phase compared with GRACE. As already observed during the comparison between WBM and river gauges, WBM/APHRODITE strongly underestimates R at all the considered locations. This result is confirmed for both basins, where we observe that R simulated by the river transport model has extremely low values.

4.3.6 Comparison with Ground Stations

Figure 4.10 and 4.11 show the results of the comparison between WBM monthly temperature and total precipitation and those measured by the 55 stations available within the basin. The

blue and red circles represent the sign and the amplitude of the mean error calculated as the mean of the monthly difference between measurements from the station and values estimated by the model at the same locations. Figure 4.10 shows the result of the comparison in the WBM/ERA Interim case. In the case of surface temperatures, we observe that Reanalysis products provide a good reproduction of surface temperature at low elevations, while large positive differences are observed in the UIB, with the model being colder than the stations. A similar error distribution can be observed in the total precipitation case in which larger negative values are observed also at low elevations in the Indian Plains. Negative errors indicate that, on average, ERA Interim estimates more precipitation than those observed by the stations.

Figure 4.11 presents the results of the same comparison applied to WBM/APHRODITE. Also in this case, surface temperatures are underestimated at elevations above 2,000 m while the agreement between gridded data and observations remains high in the LIB. APHRODITE seems to be closer to ground observations at intermediate elevations. The comparison of total precipitations shows that, also in this case, monthly precipitation above 2,000 meters tends to be higher than those measured by the climatic stations. However, in this second case, the error in precipitation is positive for the most northern stations available between the Karakoram and the Hindu Kush mountain ranges. The model, thus, becomes drier than the stations. When using WBM/ERA Interim, the temperature bias seems to be dependent on elevation and does not show any seasonal variability. Gridded datasets are in general cold with respect stations located above 1,000 m. When dealing with precipitation, the model estimate more precipitation than those measured by the climatic stations at elevations between 200 and 500 meters during the summer period, while extremely positive errors are measured during winter at elevations above 1,000 m. A similar variability is observed when using WBM/APHRODITE with both temperature and precipitation. In this case, however, we observe an inversion of the error in precipitation above 1,000 m where the gridded dataset estimates less precipitation than those measured by the stations. The difference becomes

larger during the summer period.

4.4 Discussion

We evaluated the performance of WBM when forced using ERA Interim and APHRODITE using multiple independent observations. All comparisons show that WBM/ERA Interim performs significantly better than WBM/APHRODITE. WBM/ERA Interim provides realistic estimates of the evolution of hydrological through time variables within the upstream and the downstream regions. The simulated runoff matches fairly well with the monthly river discharge values measured by river gauges and satellite altimeters. However, in the case of the Indus River, which is the main tributary of the basin, runoff is overestimated by 50% during summer. The runoff measured at the interface between the UIB and the LIB is consistent with the one estimated using the water balance equation allowing the closure of the water budget for both the UIB and the LIB.

WBM/APHRODITE strongly underestimates the runoff generated within the UIB. In this case, the runoff measured by the Water Transport Model at the interface between the UIB and the LIB remains low during the entire year and does not absolutely match with R estimated using the water balance equation. The erroneous simulation of the river discharge by the Water Transport Model affects the evolution of the TWS anomaly in the LIB, with results that are largely different from those observed by GRACE. In this second case, the LIB does not receive enough water from the upper basin to balance the mass lost through increased ET between May and September. The erroneous evaluation of R has, therefore, a strong effect on the hydrology of the LIB which starts accumulating mass only after July when precipitation transported by the monsoons enter the basin. Finally, the comparison with discharge estimates from the GRCDD project confirms that WBM/APHRODITE strongly

underestimates the runoff generated in the UIB. The model is, in fact, so dry that the water flux remains close to zero at the river's mouth during almost the entire observation time period.

We observe that winter and summer precipitation declines by 30% and 15% when using APHRODITE. A larger decrease is observed during summer in the case of ET, 23% vs 32%. WBM/APHRODITE, therefore, accumulates less mass during winter and loses proportionally less mass during summer. WBM employs the surface water available within every grid cell to recharge water reservoir available above and below ground (soil moisture, groundwater, etc.). River runoff is generated when water inputs (Precipitation, Runoff from another cell) exceed the amount of water that can be stored within the single cell or lost to evapotranspiration [Vörösmarty et al., 1998]. The reduction of winter precipitation with APHRODITE influences the amount of meltwater generated during the summer season. The model has, therefore, less water which, when available, is completely used to recharge the reservoir present below ground. There is no residual water that can be used to generate surface runoff. WBM/ERA Interim shows instead the opposite behavior. On the one hand, the good match between the available runoff observations and model outputs suggest that the model receives enough precipitation, which grants the optimal recharge of local reservoir and the correct reproduction of the storage anomaly in both the UIB and the LIB. On the other hand, the runoff values measured by river gauges available both upstream and downstream indicate that summer runoff might be overestimated by 50%. This result suggests that ERA Interim overestimates precipitation at high elevation, which produces an excessive river flux during summer.

We further investigate the possible reasons of the large discrepancies between the results obtained with the two versions of WBM comparing the simulated precipitation and temperature with measurements from 55 climatic stations within the basin. The agreement between gridded data and climatic stations is good at low elevations. At elevations above 1,000 m

WBM captures the seasonal and inter-annual variability of the two P and ET estimates. The time series of the two variables are, in general, well correlated with those derived from climatic stations. Large differences exist instead in terms of mean values and amplitude of the signals. Several studies have demonstrated that both gridded data products and ground observations can be affected by large errors in mountainous environments [Gao et al., 2014, Adam and Lettenmaier, 2003, Sevruk et al., 2009]. Climatic stations usually underestimate precipitation and overestimate atmospheric temperatures because of wind-induced undercatch of solid precipitation and because of their placement in valleys that are usually dry and warm compared to surrounding areas where most of the glacier and the snow mass is stored [Sevruk et al., 2009]. Errors in gridded data are instead largely related to their coarse resolution and the subsequent erroneous representation of the local topography. Gridded datasets, for this reason, do not capture, the highly volatile climatic conditions in these areas. Surface temperatures are in general underestimated and the estimated spatial distribution of precipitation is highly uncertain [Dahri et al., 2016]. The comparisons showed in 4.10 and 4.11 should be therefore interpreted as a proof of the large uncertainties affecting both gridded data and ground observations in the regions rather than as a real estimate of the magnitude of the errors in P and ET in ERA Interim and APHRODITE. APHRODITE is the result of the interpolation of observations from all the climatic stations available in the region. The dry bias affecting the climatic stations influences the final gridded estimates and explains why WBM performs so poorly when forced with APHRODITE. We conclude that WBM/ ERA Interim is the most reliable of the model versions and we use it for our final considerations.

The analysis of the TWS time series from GRACE reveals important characteristics of the Upper and the Lower Indus River Basin climates. The Upper Basin is characterized by a large seasonal variability with a cumulative mass variation between the end of summer and the end of the following spring above 100 Gt. This large variability is consistent with the continuous mass turnover in the region that accumulates a large amount of mass between

winter and spring in the form of solid precipitation and releases almost the same amount of water storage during summer in form of meltwater. According to WBM snowpack is largely the main contributor of the temporal changes in storage within the UIB, which on average accounts for more than 80-90% of the mass anomaly between September and May. During the summer months, snowmelt is in large part transformed in surface runoff but it also contributes to recharge of the other water pools: groundwater, soil moisture, and surface reservoirs like lakes and dams. We do not find a significant trend in mass anomaly between 2002 and 2012 (we estimate a linear trend value equal to -2.4 ± 2.5 Gt/yr). This result is consistent with the stable glacier conditions associated to the Karakoram Anomaly described in the introduction.

The LIB is instead characterized by a smaller seasonal variability, whose amplitude is 50% smaller than the one of the UIB (24 Gt). The region loses mass between February and July. During this period, the input runoff from the UIB is minimal. Given the warm climatic conditions, ET are on average always above 20 Gt/month between February and October. Maximum ET rates, above 70 Gt/month, are observed between July and August. The large ET signal during summer compensates the input of water by the monsoons. As observed in the water budget analysis, the cumulative mass lost through ET between May and November is, on average, more than the mass gained through precipitation. GRACE shows, in this case, a strong negative trend equal to -9 ± 2 Gt/yr. This mass loss in the LIB has been already discussed by Rodell et al. [2009] and is attributed to unsustainable groundwater extraction during the last decade.

4.5 Conclusions

We compare TWS anomalies for the Upper and the Lower Indus River basin obtained using time-variable gravity from GRACE and advanced hydrological modeling from WBM in order

to assess the average summer contribution by surface runoff generated at elevations above 2,000 m to the total runoff available downstream. We analyze two sets of model outputs obtained using different climatic forcing and we identify the best model set-up through direct comparison with GRACE and multiple sets of ground-based and remote sensed observations. We observe that, despite its coarser resolution, ERA Interim allows the model to obtain the best match with all the observations available for the comparison. With this configuration, runoff estimates obtained using the water balance equation match extremely well those simulated by the model at the interface between the Upper and the Lower basin. We find that, on average, every summer the Upper Indus provides 81 Gt of water to the lower basin with meltwater accounting for 65% of the total. This result confirms that water stored in the form of glaciers and snow constitutes the primary source of water to sustain agricultural activities in the Lower Indus during summer, as water gain due to precipitation transported by the monsoons is largely compensated by loss due to evapotranspiration. GRACE does not see a significant long term-trend in the Upper Basin's water storage confirming stable snow and glacier conditions during the last decade. However, given the importance attributed to meltwater, the predicted increase in global temperature will likely have significant impact on the region in the future. We provide, for the first time, a comprehensive evaluation of the hydrological cycle of the Indus River Basin improving previous assessments that were either based on pure modeling approaches or on the extrapolation based on limited data samples. We also prove that time-variable gravity from GRACE constitutes an excellent tool to test and improve hydrological models in mountainous environments. We finally identify the development of high resolution climate datasets as the primary requirement to be met in order to obtain reliable estimates of the current state and future evolution of the regional hydrology.

	UIB	LIB
GRACE (TWS)	-96.0 ± 11	42.7 ± 12
WBM (TWS)	-72.0 ± 4	40.0 ± 4
P	24.2 ± 12	115.2 ± 18
ET	39.1 ± 2	132.1 ± 13
R_{in}	0	81.0 ± 11
R_{out}	81.0 ± 11	21.5 ± 14

Table 4.1: Mass Budget components calculated using WBM/ERA Interim

	UIB	LIB
GRACE (TWS)	-110.5 ± 16	27.2 ± 12
WBM (TWS)	-55.5 ± 9	22.5 ± 6
P	6.9 ± 9	50.7 ± 16
ET	6.4 ± 1	92.6 ± 12
R_{in}	0	110.9 ± 12
R_{out}	110.9 ± 12	41.8 ± 15

Table 4.2: Mass Budget components calculated using WBM/APHRODITE

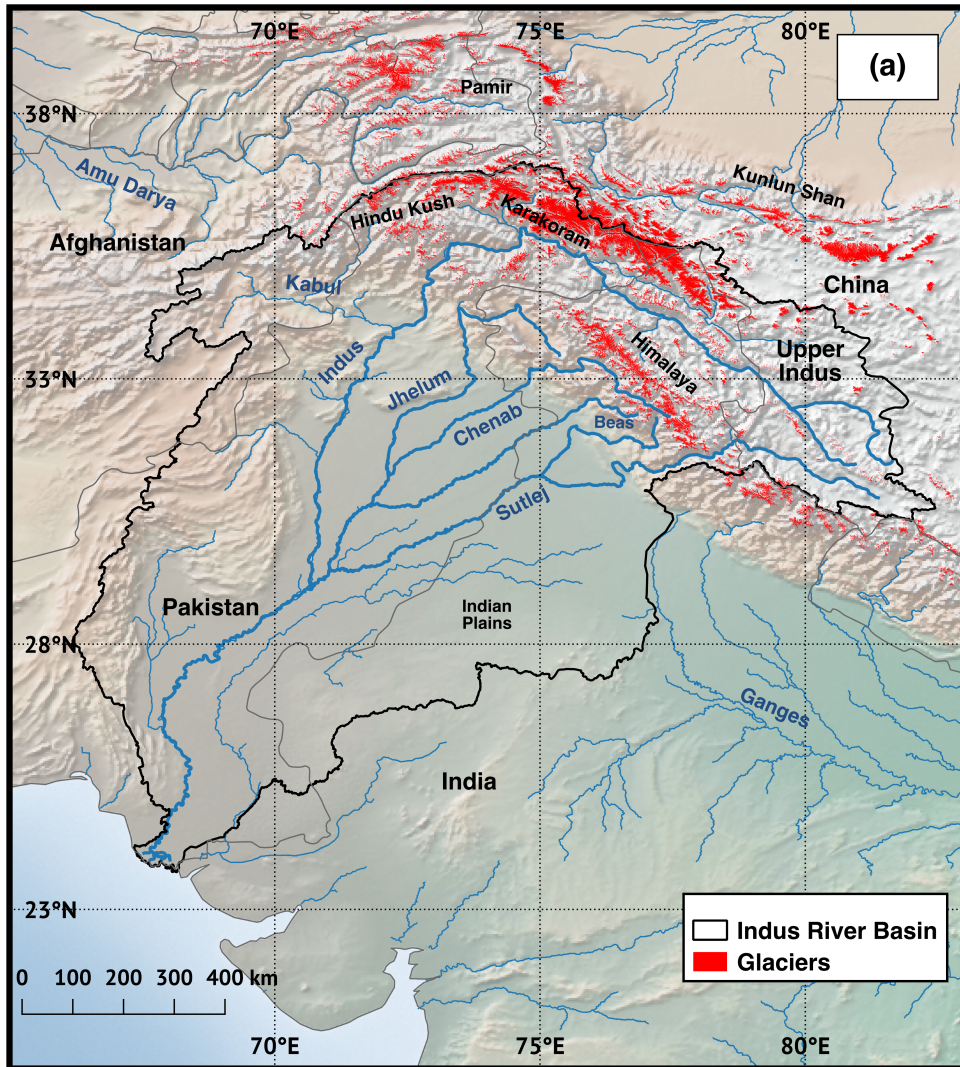


Figure 4.1: Indus River Basin. The Upper Indus Basin (UIB) is defined as the part of the region located above 2,000 meters. In Red the ice covered regions according to the sixth release of the Randolph Glacier Inventory [Pfeffer et al., 2014].

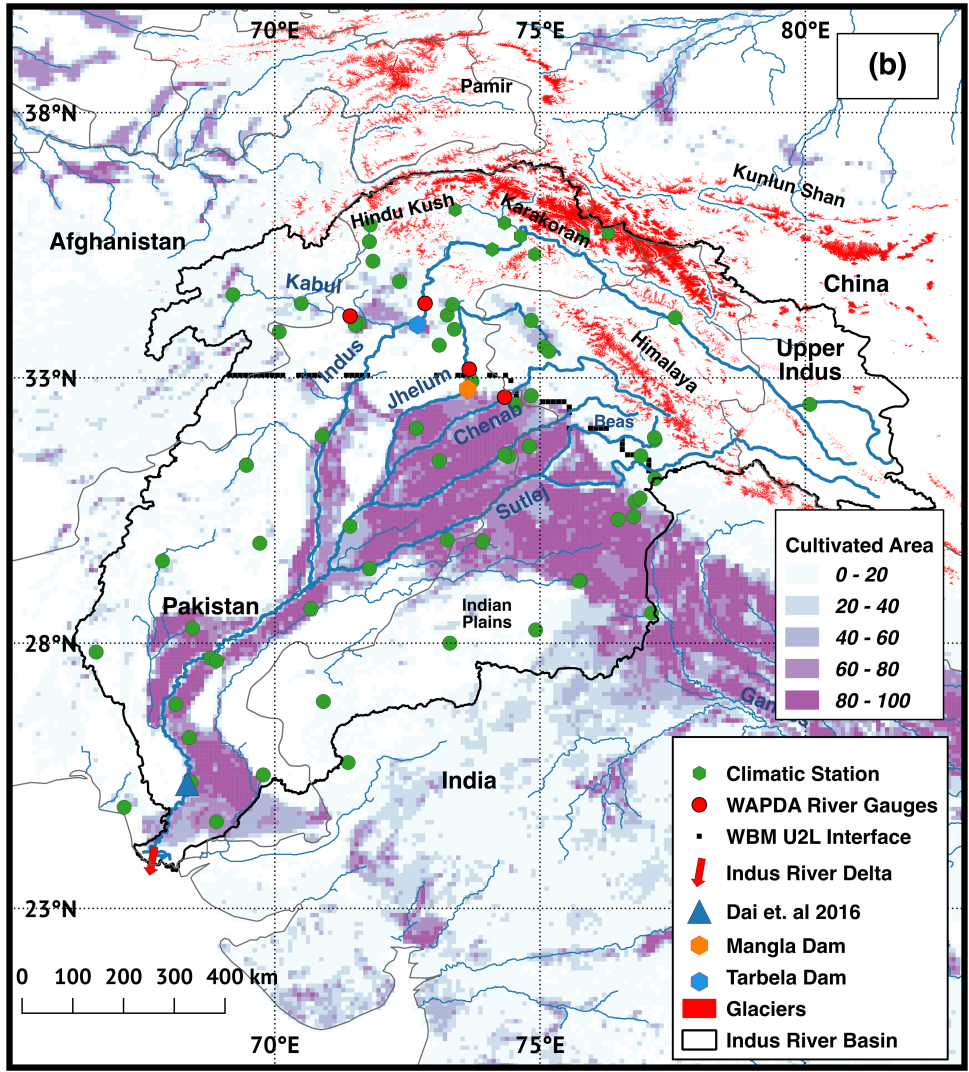


Figure 4.2: Indus Basin Irrigation System (IBIS). Red dots indicate the location of the four river gauges provided by the Water and Power Development Authority (WAPDA). Green dots indicate the position of all the climatic stations used to validate precipitation and temperature from WBM. The background of the figure shows the percentage of the total area equipped for irrigation on a 5 arc-minute grid extracted by the version 5.0 of the Global Map of Irrigation Areas distributed by the Food and Agriculture Organization of United Nations (FAO) and available at (<http://www.fao.org>).

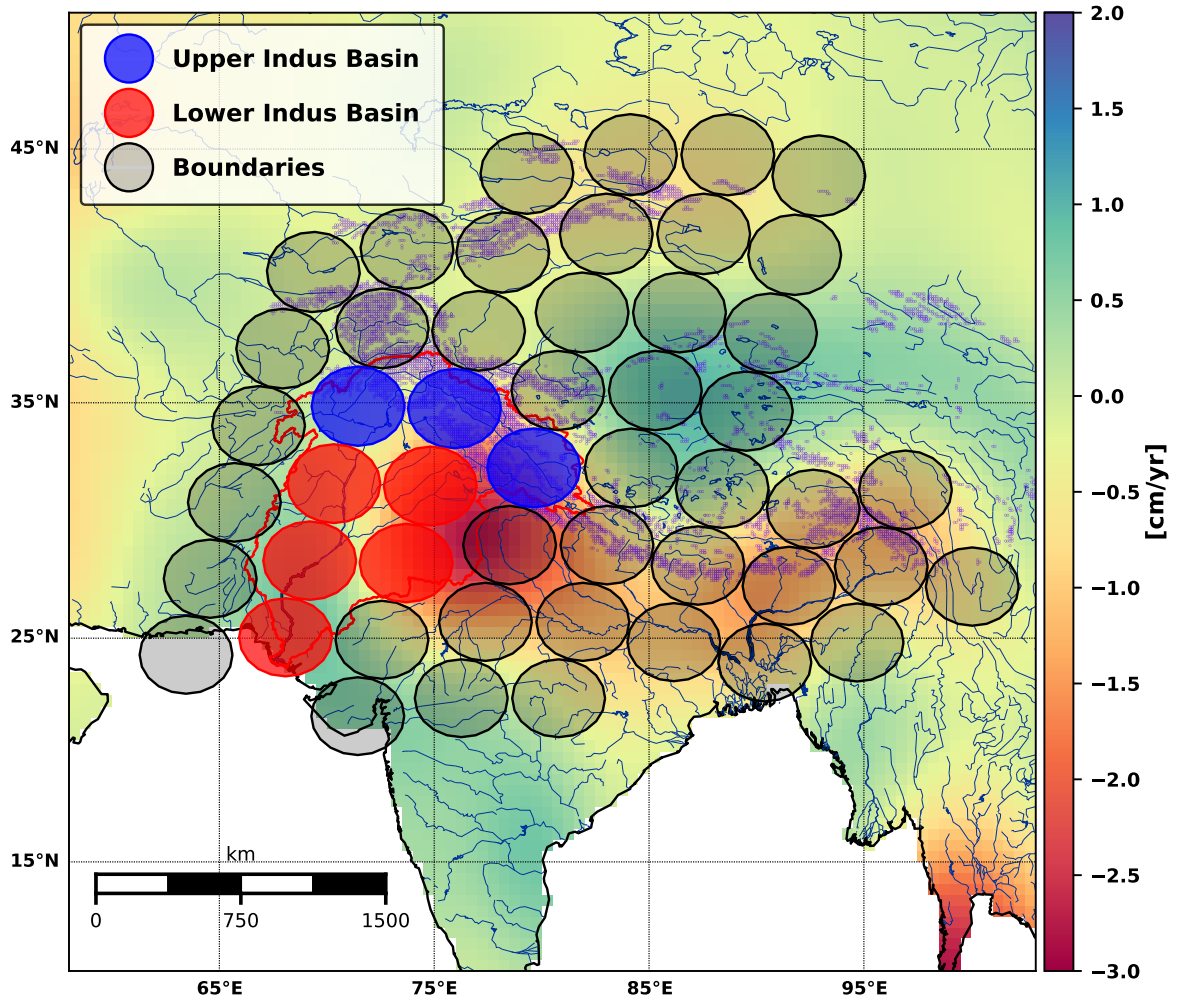


Figure 4.3: Mascon Configuration used to evaluate monthly gravity anomalies over the Indus River Basin. Each mascon is designed as 3.1 a degrees spherical cap. Spherical Caps used to extract the gravity signal relative to the Upper Indus Basin (UIB) are reported in blue, those used for the Lower Indus Basin (LIB) are reported in red. The gray spherical caps are used to cover regions surrounding the Indus River Basin in order to minimize the effect of their gravity signal on our final estimates. The background of the figure represents the total water storage (TWS) trend map extracted from GRACE for the time period between April 2002 and December 2012. The trend map was smoothed using a 350 km radius Gaussian smoothing filter. The purple dots indicate the location of the High Mountains of Asia glaciers.

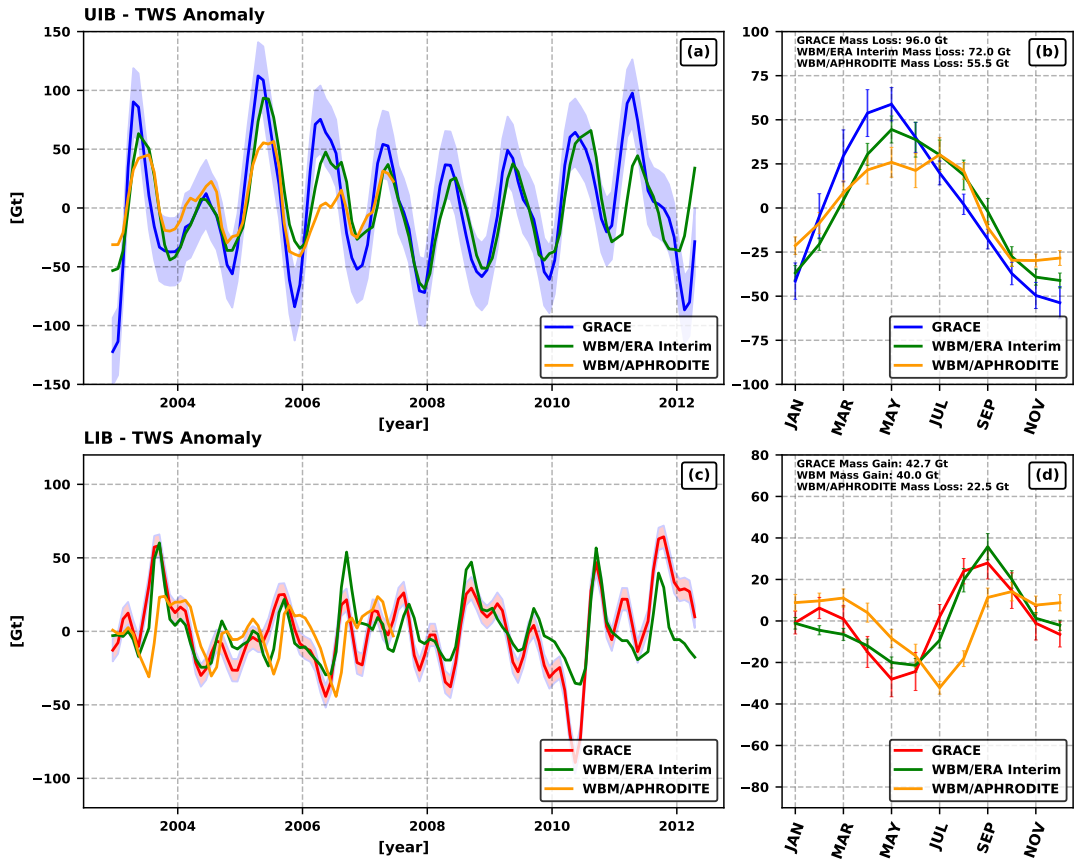


Figure 4.4: (a): Upper Indus River Basin (UIB): TWS anomaly for the time period between December 2002 and April 2012 from GRACE (in blue), WBM/Era Interim (in green) and WBM/APHRODITE. (b): Average annual TWS anomaly calculated from the time series presented in (a). (c): Lower Indus River Basin (LIB): TWS anomaly for the time period between December 2002 and April 2012 from GRACE (in red), WBM/Era Interim (in green) and WBM/APHRODITE (in gold). (d): Average annual TWS anomaly calculated from the time series presented in (c). Monthly mass anomaly values are expressed in giga-tonnes. Linear trend have been removed from the original time series.

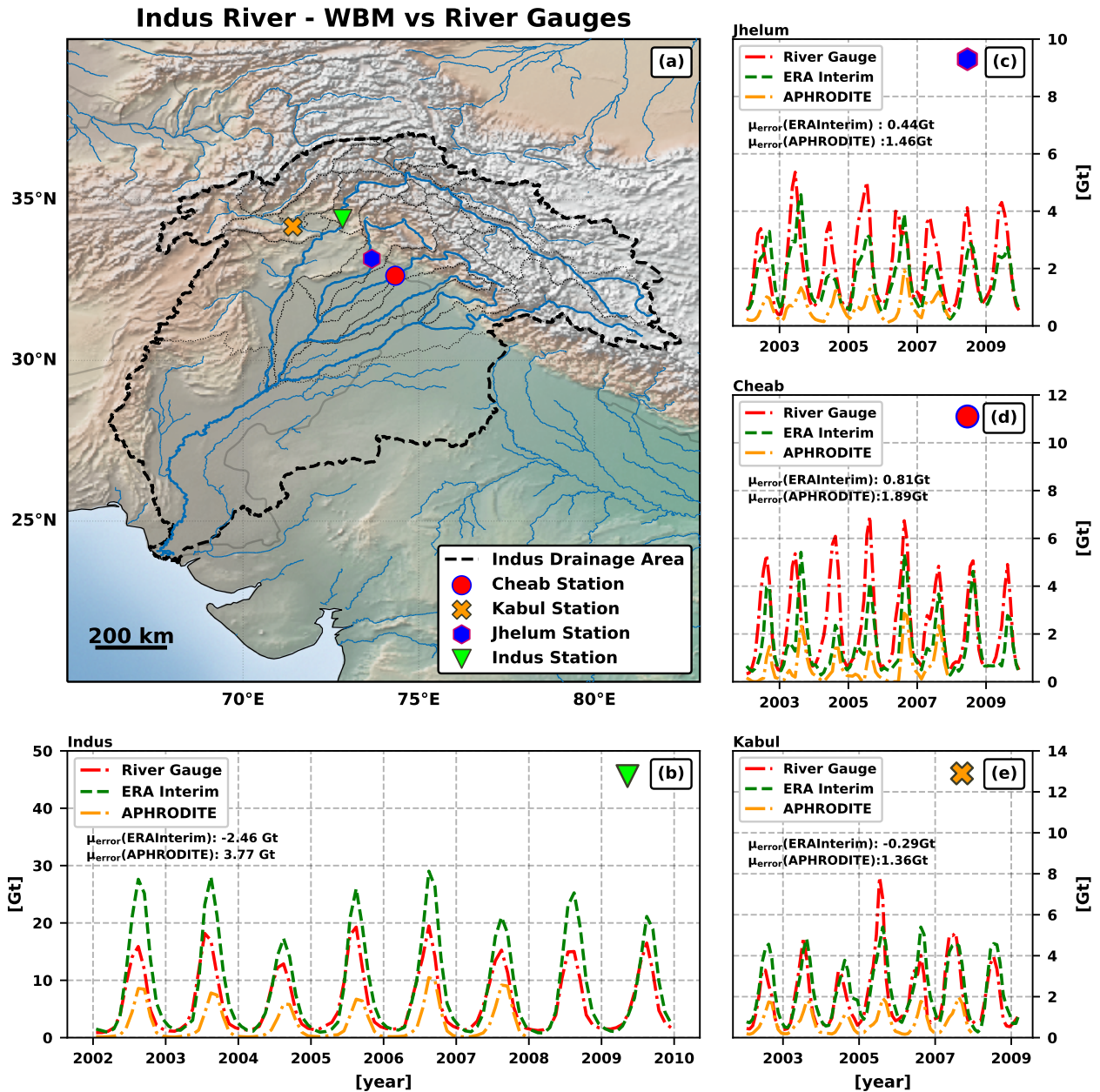


Figure 4.5: (a): Indus River Basin, with location of the considered river gauges. (b, c, d, e): Monthly river discharge time series measured at the interface between the UIB and the LIB for the main Indus River tributaries within the Pakistani territory. Monthly discharge measured by WAPDA river gauges are in red. Discharge time series simulated by WBM/ERA Interim and WBM/Aphrodite are in green and gold. Discharge time series are expressed in giga-tonnes. Mean error values are calculated as the average difference between river gauges measurements and WBM estimates.

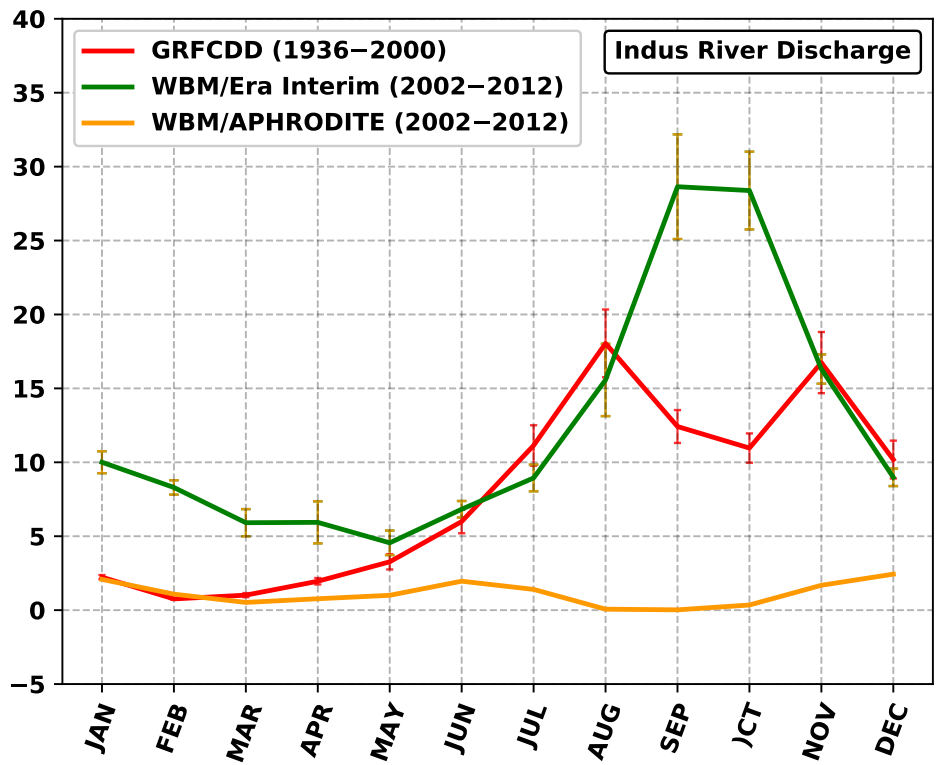


Figure 4.6: Average monthly discharge evaluated at the Indus River Delta. In red, estimates by the GRFCDD project; in blue and gold, estimates by WBM/ERA Interim and WBM/APHRODITE.

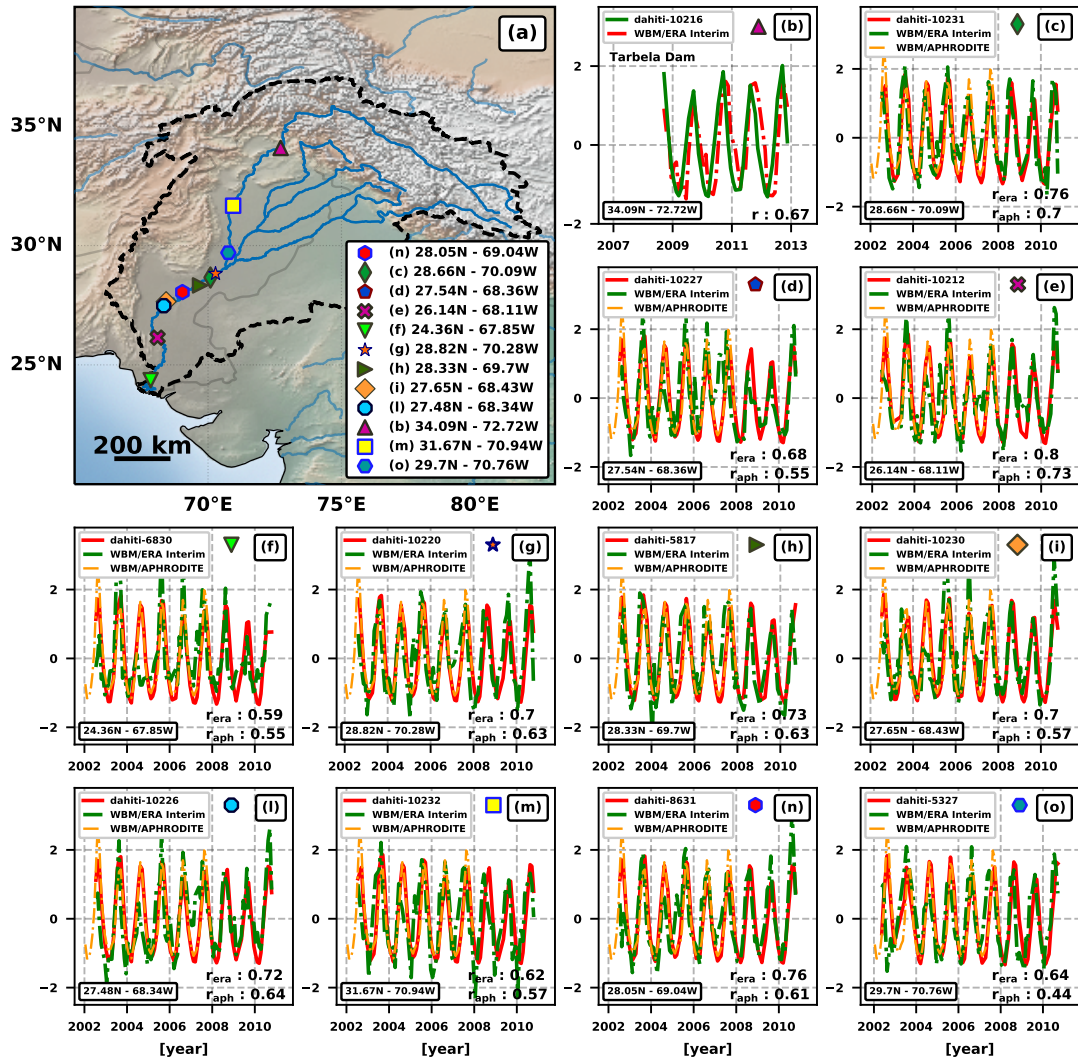


Figure 4.7: (a): Indus River Basin, with location of the considered altimetric virtual stations from the DAHITI project. (b-o): comparison between normalized river elevation time series and normalized river flux estimates from WBM. Altimetry time series are in red. Normalized discharge time series simulated by WBM/Era Interim and WBM/Aphrodite are in green and gold

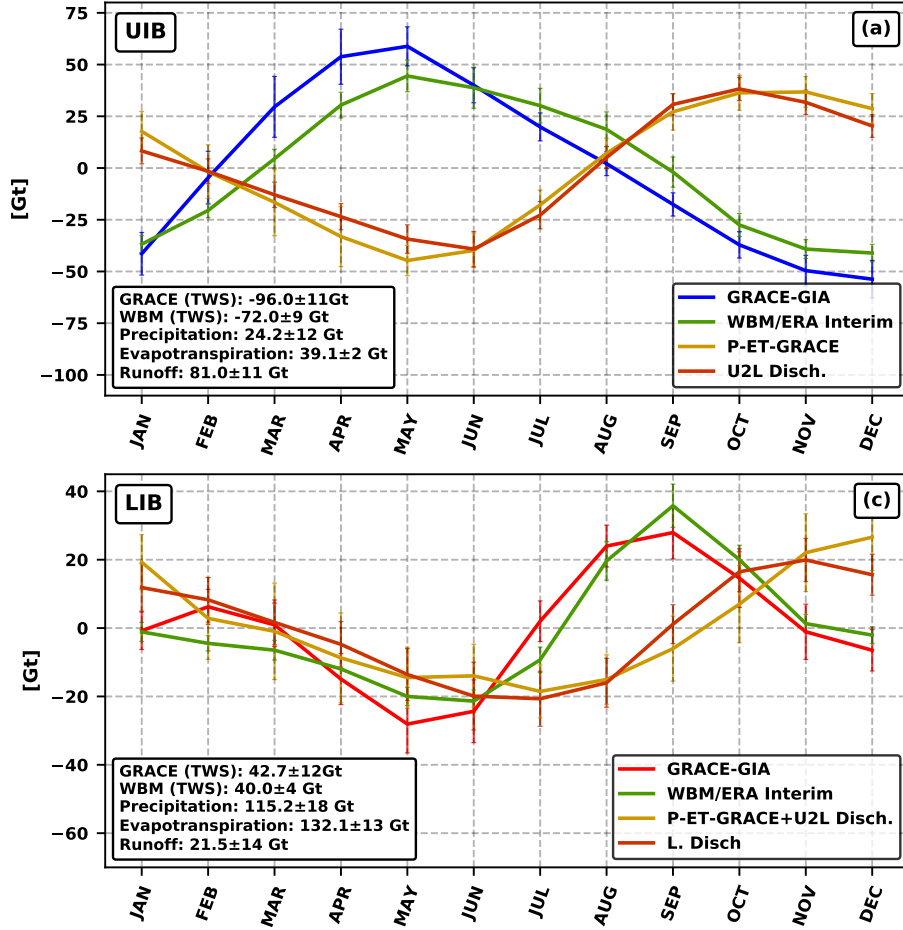


Figure 4.8: Water Budget: (a) Upper Indus River Basin (UIB): In blue, TWS average annual climatology from GRACE; in green, TWS average annual climatology from WBM; in brown, (U2L - Disch) average monthly discharge simulated by WBM at the interface between UIB and LIB; in yellow, average monthly runoff calculated as $R = P - ET - TWS$, where P and ET are extracted from WBM and TWS is measured by GRACE. (b) Lower Indus Basin (LIB): In blue, TWS average annual climatology from GRACE; in green, TWS average annual climatology from WBM; in brown, (U2L - Disch) average monthly discharge simulated by WBM at the Delta of the Indus River Basin; in yellow, average monthly runoff calculated as $R = P - ET - TWS + U2L - Disch$, where P and ET are extracted from WBM and TWS is measured by GRACE. Monthly mass anomaly values are expressed in giga-tonnes. The values reported in the boxes on the lower-left of each subfigure represents the summer mass loss/gain calculated for each climatology as the difference between values assumed between November and May.

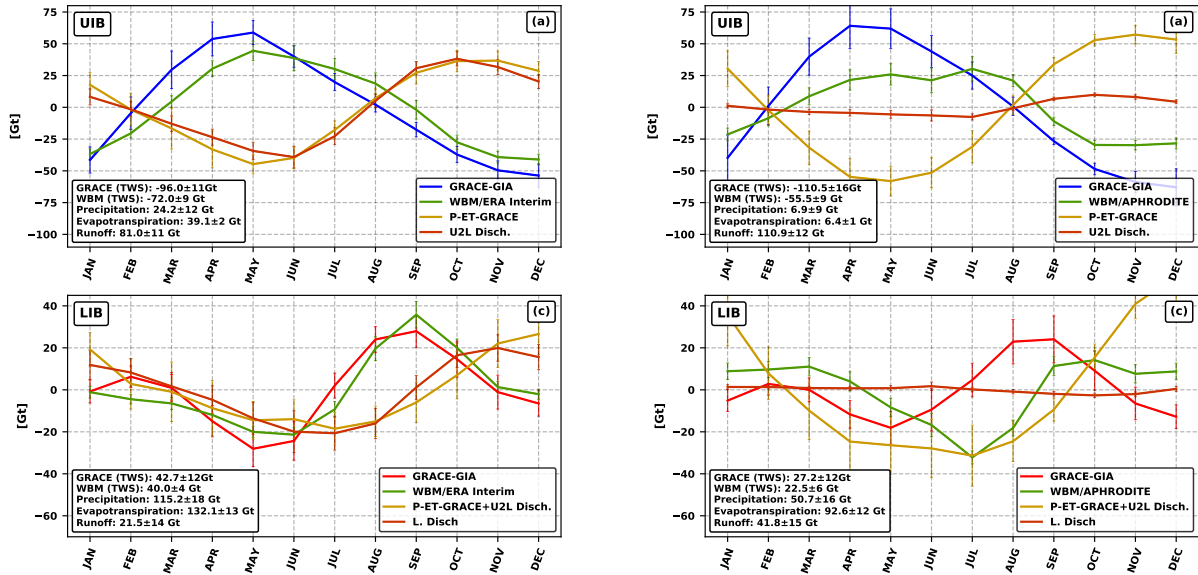


Figure 4.9: (a-b) Upper Indus River Basin Water Budget: In blue, TWS average annual climatology from GRACE; in green, TWS average annual climatology from WBM; in brown, (U2L - Disch.) average monthly discharge simulated by WBM at the interface between the UIB and the LIB; in yellow, average monthly runoff calculated as $R = P - ET - TWS$, where P and ET are extracted from WBM and TWS is measured by GRACE. (c-d) Lower Indus Basin Water Budget: In blue, TWS average annual climatology from GRACE; in green, TWS average annual climatology from WBM; in brown, (U2L - Disch.) average monthly discharge simulated by WBM at the Delta of the Indus River Basin; in yellow, average monthly runoff calculated as $R = P - ET - TWS + U2L - Disch.$, where P and ET are extracted from WBM and TWS is measured by GRACE.

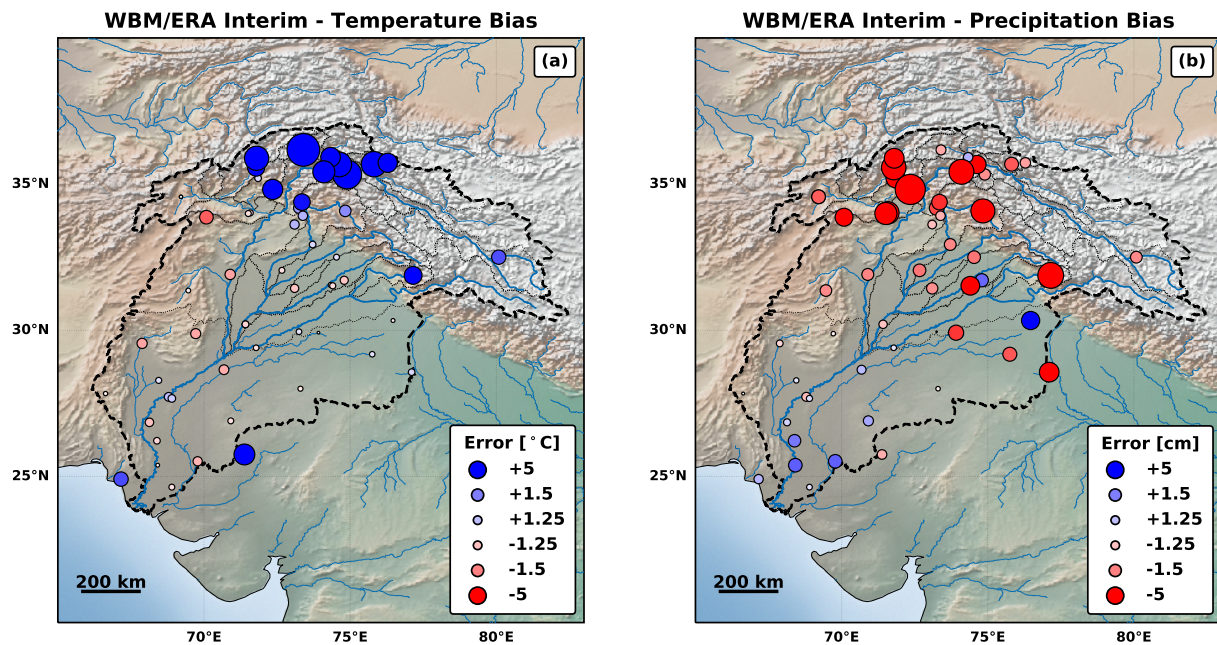


Figure 4.10: (a): comparison between monthly temperatures from WBM/ERA Interim and temperatures measured by the 55 stations available within the Indus River Basin. (b): comparison between monthly temperatures from WBM/APHRODITE and temperatures measured by the 55 stations available within the Indus River Basin. The blue and red circles represent the sign and the amplitude of the mean error calculated as the mean of the monthly difference between measurements from the station and values estimated by the model at the same locations.

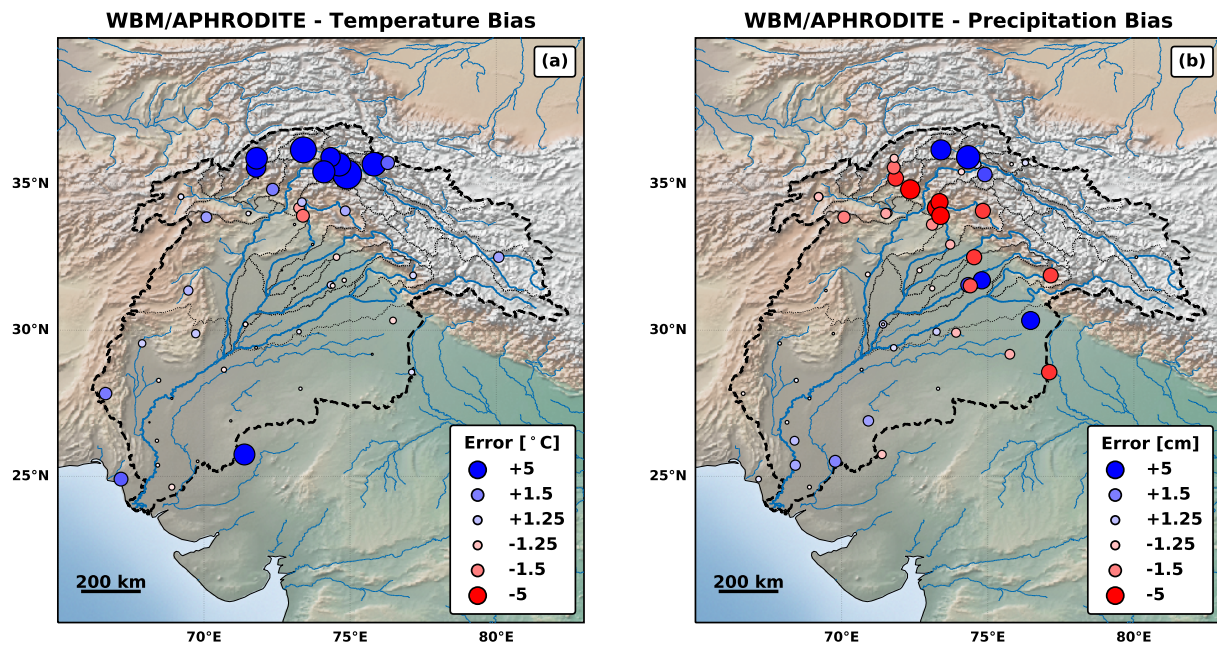


Figure 4.11: (a): comparison between monthly total precipitations from WBM/ERA Interim and precipitations measured by the 55 stations available within the Indus River Basin. (b): comparison between monthly total precipitation from WBM/APHRODITE and those measured by the 55 stations available within the Indus River Basin. The blue and red circles represent the sign and the amplitude of the mean error calculated as the mean of the monthly difference between measurements from the station and values estimated by the model at the same locations.

Chapter 5

Conclusions

The main goal of this dissertation is to improve our understanding about the changes in the Earth's Glaciers and Ice Caps (GIC) in the present-day climate by using a combination of satellite observations and hydrological model outputs.

In the first study presented in this dissertation, we conduct a global analysis of the GIC mass balance, for the time period between 2002 and 2017, by using time-variable gravity from the NASA/DLR Gravity Recovery and Climate Experiment (GRACE). We employ a rigorous statistical approach to detect significant acceleration in mass loss and to examine inter-annual variations in regional mass balance. The second study focuses on the glaciers of the Novaya Zemlya Archipelago. We compare the regional mass balance time series from the previous study, with independent estimates obtained using satellite altimetry data from the NASA Ice, Cloud, and land Elevation Satellite (ICESat) and from the ESA CryoSat-2 missions. In the third and final study, we combine terrestrial water storage (TWS) estimates from GRACE with outputs from the Water Balance Model (WBM) to study the water cycle of the Indus River Basin and to evaluate the contribution by meltwater to the total river runoff.

5.1 Summary of Results

In the first study within this dissertation (Chapter 2), we analyze the mass balance of the GIC, for the time period between April 2002 and August 2016. We obtain regional glacier mass change time series by employing a least squares mascon approach. We present a new mascon configuration based on the most recent release of the Randolph Glacier Inventory and optimized for the recovery of the glacier signal. During the fourteen-year period under analysis, the GIC lost mass at a rate equal to 209.7 ± 39.0 Gt/yr, equivalent to 0.6 ± 0.1 mm/yr of sea level rise (SLR). Seven regions covering 94% of the total GIC area account for 98% of the total mass loss: Canadian Arctic Archipelago (68.1 ± 9.7 Gt/yr), Alaska (57.1 ± 10.5 Gt/yr), Southern Andes (35.1 ± 19.2 Gt/yr), Iceland (15.2 ± 4.5 Gt/yr), Russian Arctic (14.5 ± 6.5 Gt/yr), High Mountain Asia (14.3 ± 12.7 Gt/yr), and Svalbard (9.0 ± 2.8 Gt/yr). This study significantly extends the mass balance time frame compared to previous studies. Longer mass balance time series allow us to perform a robust investigation to detect any acceleration in the regional mass loss. We find that the GIC mass loss increased between 2002 and 2016 at a rate equal to 6.7 ± 2.5 Gt/yr², with the Canadian Arctic Archipelago being the main contributor to the total acceleration (3.5 ± 0.6 Gt/yr²). The mass balance of the High Mountains of Asia is characterized by a large inter-annual variability which explains the large discrepancies between estimates from previous studies. The analysis of the extended time series unequivocally shows a significant negative trend in the region. At a sub-regional scale, different climatic conditions determine heterogeneous glacier reactions to increasing atmospheric temperatures. The mass loss, observed by GRACE, takes place almost completely in the South-East and in the North, where the glacier mass balance is strongly influenced by summer monsoons. More stable conditions are observed in the South-West where glacier accumulation is dominated by winter precipitation. Within this research, I processed the GRACE data, developed the new mascon configuration and performed the statistical analysis of the regional time series.

The second study within this dissertation (Chapter 3), focuses on the Novaya Zemlya Archipelago (NZEM). We compare estimates from the least squares mascon approach presented in Chapter 2 with independent estimates obtained using satellite altimetry data from ICESat and CryoSat-2. We introduce a new algorithm developed to evaluate spatial and temporal characteristics of the evolution of ice elevation over GIC. Results from the Gravitimetric and the Altimetric methods show excellent agreement. Between 2002 and 2016 NZEM lost mass at a rate of -8 ± 4 Gt/yr corresponding to a sea level contribution of 0.021 mm/yr. We observe that the mass loss increased after 2010, following a period of stable mass balance, reaching a maximum rate of -14.3 ± 4 Gt/yr between 2010 and 2016. We assess the impact of coast and terminus type in glacier thinning rates. We find that marine-terminating glaciers thinned significantly faster than those terminating on land. These results suggest that glaciers in the region are sensitive to variations in both surface mass balance and ice discharge. Within this research, I processed the GRACE data and the altimetry datasets, developed the new algorithms for the derivation of maps and time series of elevation change and performed the analysis of the obtained results.

The third study within this dissertation (Chapter 4), focuses on the hydrological cycle of the Indus River Basin. We develop an ad-hoc mascon configuration designed to evaluate TWS anomalies for the Upper Indus River Basin (UIB) and to the Lower Indus River Basin (LIB) and quantify the relative contribution to the total hydrological budget. We combine TWS estimates from GRACE with outputs from the Water Balance Model (WBM) in order to evaluate the average contribution by the runoff generated upstream to the total runoff available at low elevations during summer. We find that, on average, every summer the Upper Indus provides 81.0 ± 11 Gt of water to the lower basin with meltwater accounting for 65% of the total. This result suggests that water stored in the form of glaciers and snow constitutes the primary source of water to sustain agricultural activities in the Lower Indus during the summer, as water gain due to precipitation transported by the monsoons is largely compensated by loss due to evapotranspiration. GRACE does not measure a

significant long term-trend in the Upper Basin’s water storage. This result is consistent with the stable glacier conditions observed in the region by multiple studies. However, given the importance attributed to meltwater, the predicted increase in global temperatures will likely have a significant impact on the regional hydrology in the future. We test different model configurations and we observe that the obtained results are highly dependent on the climate forcing used to constrain the model. Further comparisons with independent satellite and ground observations suggest that large errors in precipitation and surface temperature at high elevations in the climate forcings constitute the largest source of uncertainty for the runoff and total water storage anomalies simulated by the model. Within this research, I processed the GRACE and WBM data, developed the new mascon configuration and performed the statistical analysis of the regional time series.

5.2 Implications and Future Directions

Within this dissertation, we provide a complete evaluation of the mass balance of the Earth’s Glaciers and Ice Caps during the first two decades of the 21st century. Our results demonstrate that glaciers outside the Antarctic and the Greenland Ice Sheets will continue being a dominant contributor to Sea Level Rise during the next decades. If we assume that the mass loss rate and acceleration measured by GRACE (209.7 ± 39.0 Gt/y, 6.7 ± 2.5 Gt/yr² over 2002 – 2016) will continue into the future, Glaciers and Ice caps will rise global sea level by 150 ± 12 mm by 2010, thus, contributing to one fourth of the total projected change in eustatic sea level [Velicogna et al., 2014a]. These results are critical not only to improve our understanding about the current state and future evolution of glaciers in a warming climate but they are also extremely important to inform policy makers and to urge the development of effective adaptation policies to reduce the impact of the projected increase in sea level.

The GRACE method, presented here, can be used to evaluate climate models over a range of

latitude and climatic regimes, for instance across the Arctic. The produced data record provides a unique opportunity to test the phasing and magnitude of the changes in precipitation and melt reconstructed by these models, which for the most part are still in development for the GIC.

Our observations demonstrate that the mass balance of the GIC regions can be subject to large inter-annual variations and the 15 years temporal interval analyzed here is short compared to the observed natural variability. The future evolution the GIC mass balance remains, therefore, uncertain. More observations are needed in order to extend the time period analyzed here and to obtain a better partitioning between the GIC mass loss acceleration and its natural variability. Several new generation satellite missions, in combination with the methodologies introduced in this work, will help to achieve these goals.

The GRACE follow-on (GRACE-FO) was launched in May 2018 and it is currently in its validation phase. GRACE-FO will provide improved data quality compared to GRACE. New gravity data available starting from late 2018 will be used to extend the GIC mass balance time series presented in Chapter 2. Longer time series will allow to further reduce the uncertainties affecting the estimated long-term changes in regions characterized by strong inter-annual variability like the High Mountains of Asia. The data gap between August 2016 and the GRACE follow-on data could be filled using reconstructions of surface mass balance from regional atmospheric climate models or using mass balance time series obtained from satellite altimetry by applying the algorithms presented in Chapter 3 to all the GIC regions..

The legacy of the ICESat and the CryoSat-2 missions will be continued by the NASA ICESat-2 mission which launch is scheduled in September 2018. The main instrument carried by this new system is the Advanced Topographic Laser Altimeter System (ATLAS) [Abdalati et al., 2010]. ATLAS is a 6-beam photon counting laser altimeter that will provide highly increased spatial resolution and accuracy compared to the first ICESat mission. The use of a 6-beam altimeters will allow the sensor to detect not only the surface elevation but also

the cross-track slope at each nadir point. The mission will operate in continuous mode, and with an incredibly high pulse rate. The altimeter will in fact send 10,000 pulses per second taking measurements every 2.3 feet along the satellite's track. This unprecedented spatial resolution, together with the continuous coverage, will allow to extend the application of multi-sensor comparisons like the one presented in Chapter 3 not only to other arctic ice caps but also to mountain glaciers.

Results presented in Chapter 3 show that glaciers of the Novaya Zemlya Archipelago are sensitive to both surface mass balance and ice dynamical discharge. However, altimetric and gravimetric observations alone do not allow us to determine the weight of the two components in the total ice mass loss. In order to evaluate the exact partitioning of the total mass loss, our observations must be complemented with independent estimates of at least one of the two components. Surface mass balance processes can be estimated using regional climate models while dynamical discharge will require the evaluation of glacier velocities and thickness using satellite observations (see Chapter 1). Our analysis indicates that the inter-annual variability observed in the regional glacier mass balance correlates well with temporal variations of summer temperatures. At the same time, the acceleration in mass loss observed after 2010 took place with simultaneous increase in surface ocean temperatures and decrease in sea ice coverage. The effect of changes in ocean conditions, therefore, needs to be further investigated in order to obtain a conclusive glaciological interpretation of the physical processes driving the glacier shrinkage in the region and subsequently improve our capability to predict the total glacier contribution to sea level rise during the next decades.

The High Mountains of Asia are among the most unexplored regions on the planet. The lack of observations makes the validation of existing hydrological and glacier mass balance models extremely difficult. Available projections about glacier evolution and the relative impact on the regional hydrology remain, therefore, highly uncertain. The GRACE method presented in Chapter 4 can be used to evaluate outputs from these models and help to isolate potential

sources of error. As reported in Chapter 2, we observe that glaciers of Central Asia are not reacting uniformly to rising atmospheric temperatures. Therefore, glacier changes within the different sub-regions will have variable impact on the hydrology of the downstream regions. Extending the analysis presented in Chapter 4 to the other major river basins of the Central Asia will provide local governments with critical information to assess the impact of climate change on water resources. These results will facilitate the implementation of hydrological planning and water resource management reducing, in this way, the risk of water stress and social instability in the entire region.

Bibliography

- G. A. J. Wahr, and S. Zhong. Computations of the viscoelastic response of a 3-D compressible Earth to surface loading: an application to Glacial Isostatic Adjustment in Antarctica and Canada. *Geophysical Journal International*, 192(2):557–572, Feb. 2013. ISSN 0956-540X. doi: 10.1093/gji/ggs030. URL <https://academic.oup.com/gji/article/192/2/557/2889898/Computations-of-the-viscoelastic-response-of-a-3-D>.
- W. Abdalati, H. J. Zwally, R. Bindenschadler, B. Csatho, S. L. Farrell, H. A. Fricker, D. Harding, R. Kwok, M. Lefsky, T. Markus, et al. The icesat-2 laser altimetry mission. *Proceedings of the IEEE*, 98(5):735–751, 2010.
- J. B. Abshire, X. Sun, H. Riris, J. M. Sirota, J. F. McGarry, S. Palm, D. Yi, and P. Liiva. Geoscience Laser Altimeter System (GLAS) on the ICESat Mission: On-orbit measurement performance. *Geophysical Research Letters*, 32(21), 2005. doi: 10.1029/2005GL024028. URL <https://agupubs.onlinelibrary.wiley.com/doi/abs/10.1029/2005GL024028>.
- J. C. Adam and D. P. Lettenmaier. Adjustment of global gridded precipitation for systematic bias. *Journal of Geophysical Research: Atmospheres*, 108(D9), 2003.
- G. Aðalgeirsdóttir, T. Jóhannesson, H. Björnsson, F. Pálsson, and O. Sigurðsson. Response of Hofsjökull and southern Vatnajökull, Iceland, to climate change. *Journal of Geophysical Research: Earth Surface*, 111(F3):F03001, Sept. 2006. ISSN 2156-2202. doi: 10.1029/2005JF000388.
- E. M. Aizen, V. B. Aizen, J. M. Melack, T. Nakamura, and T. Ohta. Precipitation and atmospheric circulation patterns at mid-latitudes of Asia. *International Journal of Climatology*, 21(5):535–556, 2000. doi: 10.1002/joc.626. URL <https://rmets.onlinelibrary.wiley.com/doi/abs/10.1002/joc.626>.
- R. B. Alley, M. K. Spencer, and S. Anandakrishnan. Ice-sheet mass balance : assessment , attribution and prognosis. (2001):1–7, 2007.
- D. Archer and H. Fowler. Spatial and temporal variations in precipitation in the Upper Indus Basin, global teleconnections and hydrological implications. *Hydrology and Earth System Sciences Discussions*, 8(1):47–61, 2004. URL <https://hal.archives-ouvertes.fr/hal-00304788>.
- S. Bettadpur. *UTCSR Level-2 Processing Standards Document, Technical Report GRACE*. Number 327-742. Center for Space Researchh, University of Texas, Austin, Texas, 2012.

- H. Björnsson, F. Pólsson, S. Gudmundsson, E. Magnússon, G. Adalgeirsdóttir, T. Jóhannesson, E. Berthier, O. Sigurdsson, and T. Thorsteinsson. Contribution of Icelandic ice caps to sea level rise: Trends and variability since the Little Ice Age. *Geophysical Research Letters*, 40(8):1546–1550, Apr. 2013. ISSN 1944-8007. doi: 10.1002/grl.50278. URL <http://onlinelibrary.wiley.com/doi/10.1002/grl.50278/abstract>.
- T. Bolch, A. Kulkarni, A. Kääh, C. Huggel, F. Paul, J. G. Cogley, H. Frey, J. S. Kargel, K. Fujita, M. Scheel, S. Bajracharya, and M. Stoffel. The State and Fate of Himalayan Glaciers. *Science*, 336(6079):310–314, 2012. ISSN 0036-8075. doi: 10.1126/science.1215828. URL <http://science.sciencemag.org/content/336/6079/310>.
- B. Bookhagen and D. W. Burbank. Toward a complete Himalayan hydrological budget: Spatiotemporal distribution of snowmelt and rainfall and their impact on river discharge. *Journal of Geophysical Research: Earth Surface*, 115(F3), 2012. doi: 10.1029/2009JF001426. URL <https://agupubs.onlinelibrary.wiley.com/doi/abs/10.1029/2009JF001426>.
- A. A. Borsa, G. Moholdt, H. A. Fricker, and K. M. Brunt. A range correction for ICESat and its potential impact on ice-sheet mass balance studies. *The Cryosphere*, 8(2):345–357, 2014/03 2014. doi: 10.5194/tc-8-345-2014. URL <http://www.the-cryosphere.net/8/345/2014/>. n/a.
- J. Bouffard, E. Webb, M. Scagliola, A. Garcia-Mondéjar, S. Baker, D. Brockley, J. Gaudelli, A. Muir, A. Hall, R. Mannan, M. Roca, M. Fornari, F. P., and P. T. CryoSat instrument performance and ice product quality status. *Advances in Space Research*, 2017. ISSN 0273-1177. doi: <https://doi.org/10.1016/j.asr.2017.11.024>. URL <http://www.sciencedirect.com/science/article/pii/S0273117717308359>.
- A. C. Brenner, J. P. DiMarzio, and H. J. Zwally. Precision and Accuracy of Satellite Radar and Laser Altimeter Data Over the Continental Ice Sheets. *IEEE Transactions on Geoscience and Remote Sensing*, 45(2):321–331, Feb 2007. ISSN 0196-2892. doi: 10.1109/TGRS.2006.887172.
- F. Brun, E. Berthier, P. Wagnon, A. Kääh, and D. Treichler. A spatially resolved estimate of High Mountain Asia glacier mass balances from 2000 to 2016. *Nature Geoscience*, 10: 668–674, 2017. doi: 10.1038/ngeo2999. URL <http://dx.doi.org/10.1038/ngeo2999>.
- K. P. Burnham and D. R. Anderson. *Model Selection and Multimodel Inference*. Springer-Verlag, New York, 175 Fifth Avenue, New York, NY., second edition, 2002.
- J. R. Carr, H. Bell, R. Killick, and T. Holt. Exceptional retreat of Novaya Zemlya’s marine-terminating outlet glaciers between 2000 and 2013. *The Cryosphere*, 11(5):2149–2174, 2017. doi: 10.5194/tc-11-2149-2017. URL <https://www.the-cryosphere.net/11/2149/2017/>.
- R. Carr, C. R Stokes, and A. Vieli. Recent retreat of major outlet glaciers on Novaya Zemlya, Russian Arctic, influenced by fjord geometry and sea-ice conditions. *Journal of Glaciology*, 60, 11 2013.

- B. F. Chao and R. S. Gross. Changes in the Earth's rotation and low-degree gravitational field induced by earthquakes. *Geophysical Journal of the Royal Astronomical Society*, 91(3):569–596, 1987.
- M. Cheng, B. D. Tapley, and J. C. Ries. Deceleration in the Earth's oblateness. *Journal of Geophysical Research: Solid Earth*, 118(2):740–747, Feb. 2013. ISSN 2169-9356. doi: 10.1002/jgrb.50058. URL <http://onlinelibrary.wiley.com/doi/10.1002/jgrb.50058/abstract>.
- J. A. Church, N. J. White, L. F. Konikow, C. M. Domingues, J. G. Cogley, E. Rignot, J. M. Gregory, M. R. van den Broeke, A. J. Monaghan, and I. Velicogna. Revisiting the Earth's sea-level and energy budgets from 1961 to 2008. *Geophysical Research Letters*, 38(18), 2011.
- J. G. Cogley. Geodetic and direct mass-balance measurements: comparison and joint analysis. *Annals of Glaciology*, 50(50):96–100, 2009.
- K. M. Cuffey and W. S. B. Paterson. *The physics of glaciers*. Academic Press, 2010.
- Z. H. Dahri, F. Ludwig, E. Moors, B. Ahmad, A. Khan, and P. Kabat. An appraisal of precipitation distribution in the high-altitude catchments of the Indus basin. *Science of the Total Environment*, 548:289–306, 2016.
- A. Dai. *Historical and Future Changes in Streamflow and Continental Runoff*, chapter 2, pages 17–37. American Geophysical Union (AGU), 2016. ISBN 9781118971772. doi: 10.1002/9781118971772.ch2. URL <https://agupubs.onlinelibrary.wiley.com/doi/abs/10.1002/9781118971772.ch2>.
- A. Dai and K. E. Trenberth. Estimates of freshwater discharge from continents: Latitudinal and seasonal variations. *Journal of hydrometeorology*, 3(6):660–687, 2002.
- C. H. Davis. Satellite radar altimetry. *IEEE Transactions on Microwave Theory and Techniques*, 40(6):1070–1076, Jun 1992. ISSN 0018-9480. doi: 10.1109/22.141337.
- M. De Woul and R. Hock. Static mass-balance sensitivity of Arctic glaciers and ice caps using a degree-day approach. *Ann. Glaciol.*, 42(Table 1):217–224, 2005. ISSN 02603055. doi: 10.3189/172756405781813096.
- D. P. Dee, S. M. Uppala, A. J. Simmons, P. Berrisford, P. Poli, S. Kobayashi, U. Andrae, M. A. Balmaseda, G. Balsamo, P. Bauer, P. Bechtold, A. C. M. Beljaars, L. van de Berg, J. Bidlot, N. Bormann, C. Delsol, R. Dragani, M. Fuentes, A. J. Geer, L. Haimberger, S. B. Healy, H. Hersbach, E. V. Hólm, L. Isaksen, P. Kållberg, M. Köhler, M. Matricardi, A. P. McNally, B. M. Monge-Sanz, J.-J. Morcrette, B.-K. Park, C. Peubey, P. de Rosnay, C. Tavolato, J.-N. Thépaut, and F. Vitart. The ERA-Interim reanalysis: configuration and performance of the data assimilation system. *Quarterly Journal of the Royal Meteorological Society*, 137(656):553–597, 2011. doi: 10.1002/qj.828.

- R. R. Dickson, T. J. Osborn, J. W. Hurrell, J. Meincke, J. Blindheim, B. Adlandsvik, T. Vinje, G. Alekseev, and W. Maslowski. The Arctic Ocean Response to the North Atlantic Oscillation. *Journal of Climate*, 13(15):2671–2696, 2000. doi: 10.1175/1520-0442(2000)013<2671:TAORTT>2.0.CO;2. URL [https://doi.org/10.1175/1520-0442\(2000\)013<2671:TAORTT>2.0.CO;2](https://doi.org/10.1175/1520-0442(2000)013<2671:TAORTT>2.0.CO;2).
- H. Dobslaw, F. Flechtner, I. Bergmann-Wolf, C. Dahle, R. Dill, S. Esselborn, I. Sasgen, and M. Thomas. Simulating high-frequency atmosphere-ocean mass variability for dealiasing of satellite gravity observations: AOD1B RL05. *Journal of Geophysical Research: Oceans*, 118(7):3704–3711, 2013. ISSN 2169-9291. doi: 10.1002/jgrc.20271. URL <http://dx.doi.org/10.1002/jgrc.20271>.
- J. A. Dowdeswell, J. O. Hagen, H. Björnsson, A. F. Glazovsky, W. D. Harrison, P. Holmlund, J. Jania, R. M. Koerner, B. Lefauconnier, C. L. Ommanney, and R. H. Thomas. The Mass Balance of Circum-Arctic Glaciers and Recent Climate Change. *Quaternary Research*, 48(1):1 – 14, 1997. ISSN 0033-5894. doi: <https://doi.org/10.1006/qres.1997.1900>. URL <http://www.sciencedirect.com/science/article/pii/S0033589497919001>.
- T. Dunse, T. Schellenberger, J. O. Hagen, A. Kääh, T. V. Schuler, and C. H. Reijmer. Glacier-surge mechanisms promoted by a hydro-thermodynamic feedback to summer melt. *The Cryosphere*, 9(1):197–215, Feb. 2015. ISSN 1994-0424. doi: 10.5194/tc-9-197-2015. URL <https://www.the-cryosphere.net/9/197/2015/>.
- EV-K2-CNR. UCAR/NCAR - Earth Observing Laboratory CEOP_AP Pakistan Karakorum Surface Meteorology and Radiation Data Set. Version 1.0. UCAR/NCAR - Earth Observing Laboratory. <https://data.eol.ucar.edu/dataset/76.200.>, 2011. Accessed: 2018-08-10.
- W. E. Farrell. Deformation of the Earth by surface loads. *Reviews of Geophysics*, 10(3): 761–797, 1972. doi: 10.1029/RG010i003p00761. URL <https://agupubs.onlinelibrary.wiley.com/doi/abs/10.1029/RG010i003p00761>.
- L. Foresta, N. Gourmelen, F. Pálsson, P. Nienow, H. Björnsson, and A. Shepherd. Surface elevation change and mass balance of Icelandic ice caps derived from swath mode CryoSat-2 altimetry. *Geophysical Research Letters*, 43(23):2016GL071485, Dec. 2016. ISSN 1944-8007. doi: 10.1002/2016GL071485. URL <http://onlinelibrary.wiley.com/doi/10.1002/2016GL071485/abstract>.
- N. Forsythe, H. J. Fowler, X.-F. Li, S. Blenkinsop, and D. Pritchard. Karakoram temperature and glacial melt driven by regional atmospheric circulation variability. *Nature Climate Change*, 7(9):664, 2017.
- H. Fowler and D. Archer. Hydro-climatological variability in the Upper Indus Basin and implications for water resources. 01 2005.
- H. J. Fowler and D. R. Archer. Conflicting signals of climatic change in the upper indus basin. *Journal of Climate*, 19(17):4276–4293, 2006. doi: 10.1175/JCLI3860.1. URL <https://doi.org/10.1175/JCLI3860.1>.

- K. Frenken. *Irrigation in Southern and Eastern Asia in figures - AQUASTAT Survey 2011*. 01 2012. ISBN 978-92-5-107282-0.
- H. A. Fricker, A. Borsa, B. Minster, C. Carabajal, K. Quinn, and B. Bills. Assessment of ICESat performance at the salar de Uyuni, Bolivia. *Geophysical Research Letters*, 32(21), 2005. doi: 10.1029/2005GL023423. URL <https://agupubs.onlinelibrary.wiley.com/doi/abs/10.1029/2005GL023423>.
- K. Fujita. Influence of precipitation seasonality on glacier mass balance and its sensitivity to climate change. *Annals of Glaciology*, 48:88–92, 2008.
- L. Gao, L. Hao, and X.-w. Chen. Evaluation of ERA-interim monthly temperature data over the Tibetan Plateau. *Journal of Mountain Science*, 11(5):1154–1168, 2014.
- A. S. Gardner, G. Moholdt, B. Wouters, G. J. Wolken, D. O. Burgess, M. J. Sharp, J. G. Cogley, C. Braun, and C. Labine. Sharply increased mass loss from glaciers and ice caps in the Canadian Arctic Archipelago. *Nature*, 473(7347):357–360, May 2011. ISSN 0028-0836. doi: 10.1038/nature10089. URL <https://www.nature.com/nature/journal/v473/n7347/abs/nature10089.html>.
- A. S. Gardner, G. Moholdt, J. G. Cogley, B. Wouters, A. A. Arendt, J. Wahr, E. Berthier, R. Hock, W. T. Pfeffer, G. Kaser, S. R. M. Ligtenberg, T. Bolch, M. J. Sharp, J. O. Hagen, M. R. v. d. Broeke, and F. Paul. A Reconciled Estimate of Glacier Contributions to Sea Level Rise: 2003 to 2009. *Science*, 340(6134):852–857, May 2013. ISSN 0036-8075, 1095-9203. doi: 10.1126/science.1234532. URL <http://www.sciencemag.org/content/340/6134/852>.
- K. L. Grant, C. R. Stokes, and I. S. Evans. Identification and characteristics of surge-type glaciers on Novaya Zemlya, Russian Arctic. *Journal of Glaciology*, 55(194):960–972, 2009. doi: 10.3189/002214309790794940.
- L. Gray, D. Burgess, L. Copland, M. N. Demuth, T. Dunse, K. Langley, and T. V. Schuler. CryoSat-2 delivers monthly and inter-annual surface elevation change for Arctic ice caps. *The Cryosphere*, 9(5):1895–1913, 2015. doi: 10.5194/tc-9-1895-2015. URL <https://www.the-cryosphere.net/9/1895/2015/>.
- D. S. Grogan, D. Wisser, A. Prusevich, R. B. Lammers, and S. Frolking. The use and re-use of unsustainable groundwater for irrigation: a global budget. *Environmental Research Letters*, 12(3):034017, 2017. URL <http://stacks.iop.org/1748-9326/12/i=3/a=034017>.
- M. G. Grosval'd and V. M. Kotlyakov. Present-Day Glaciers in the U.S.S.R. and Some Data on their Mass Balance. *Journal of Glaciology*, 8(52), 1969. doi: 10.3189/S0022143000020748.
- C. Harig and F. J. Simons. Ice mass loss in Greenland, the Gulf of Alaska, and the Canadian Archipelago: Seasonal cycles and decadal trends. *Geophysical Research Letters*, 43(7): 3150–3159, 2016. doi: 10.1002/2016GL067759. URL <https://agupubs.onlinelibrary.wiley.com/doi/abs/10.1002/2016GL067759>.

- I. Harris, P. Jones, T. Osborn, and D. Lister. Updated high-resolution grids of monthly climatic observations—the CRU TS3.10 Dataset. *International Journal of Climatology*, 34(3):623–642, 2014.
- K. Hewitt. Glacier Change, Concentration, and Elevation Effects in the Karakoram Himalaya, Upper Indus Basin. *Mountain Research and Development*, 31(3):188 – 200, 2011. ISSN 0276-4741. doi: doi:10.1659/MRD-JOURNAL-D-11-00020.1. URL <http://www.bioone.org/doi/abs/10.1659/MRD-JOURNAL-D-11-00020.1>.
- Y. Hirabayashi, P. Döll, and S. Kanae. Global-scale modeling of glacier mass balances for water resources assessments: Glacier mass changes between 1948 and 2006. *Journal of Hydrology*, 390(3):245–256, Sept. 2010. ISSN 0022-1694. doi: 10.1016/j.jhydrol.2010.07.001. URL <http://www.sciencedirect.com/science/article/pii/S0022169410004142>.
- B. Hofmann-Wellenhof and H. Moritz. *Physical geodesy*. Springer Science & Business Media, 2006.
- J. W. Hurrell. Influence of variations in extratropical wintertime teleconnections on northern hemisphere temperature. *Geophysical Research Letters*, 23(6):665–668, 1996. doi: 10.1029/96GL00459. URL <https://agupubs.onlinelibrary.wiley.com/doi/abs/10.1029/96GL00459>.
- J. W. Hurrell. The Climate Data Guide: Hurrell North Atlantic Oscillation (NAO) Index (station-based). <https://climatedataguide.ucar.edu/climate-datahurrell-north-atlantic-oscillation-nao-index-station-based>, 2017. [Online; accessed 8-July-2018].
- M. Huss and R. Hock. Global-scale hydrological response to future glacier mass loss. *Nature Climate Change*, 8(2):51758–6798, 2018. doi: 10.1038/s41558-017-0049-x. URL <https://doi.org/10.1038/s41558-017-0049-x>.
- W. W. Immerzeel, L. P. H. van Beek, and M. F. P. Bierkens. Climate Change Will Affect the Asian Water Towers. *Science*, 328(5984):1382–1385, 2010. ISSN 0036-8075. doi: 10.1126/science.1183188. URL <http://science.sciencemag.org/content/328/5984/1382>.
- W. W. Immerzeel, F. Pellicciotti, and M. F. P. Bierkens. Rising river flows throughout the twenty-first century in two Himalayan glacierized watersheds. *Nature Geoscience*, 6(724), 2013. doi: 10.1038/ngeo1896. URL <http://dx.doi.org/10.1038/ngeo1896>.
- T. Jacob, J. Wahr, R. Gross, S. Swenson, and A. Geruo. Estimating geoid height change in North America: past, present and future. *Journal of Geodesy*, 86(5):337–358, 2012a.
- T. Jacob, J. Wahr, W. T. Pfeffer, and S. Swenson. Recent contributions of glaciers and ice caps to sea level rise. *Nature*, 482(7386):514–518, Feb. 2012b. ISSN 0028-0836. doi: 10.1038/nature10847. URL <http://www.nature.com/nature/journal/v482/n7386/full/nature10847.html>.
- J. R. Jensen. Angle measurement with a phase monopulse radar altimeter. *IEEE Transactions on Antennas and Propagation*, 47:715–724, Apr. 1999. doi: 10.1109/8.768812.

- J. R. Jensen and R. K. Raney. Multi-mission radar altimeter: concept and performance. In *Geoscience and Remote Sensing Symposium, 1996. IGARSS '96. 'Remote Sensing for a Sustainable Future.'*, International, volume 4, pages 2279–2281 vol.4, May 1996. doi: 10.1109/IGARSS.1996.516961.
- A. Kääb, E. Berthier, C. Nuth, J. Gardelle, and Y. Arnaud. Contrasting patterns of early twenty-first-century glacier mass change in the Himalayas. *Nature*, 488:495, 2012. doi: 10.1038/nature11324. URL <http://dx.doi.org/10.1038/nature11324>.
- S. B. Kapnick, T. L. Belworth, M. Ashfaq, S. Malyshev, and P. C. D. Milly. Snowfall less sensitive to warming in Karakoram than in Himalayas due to a unique seasonal cycle. *Nature Geoscience*, 7:834, 10 2014. doi: 10.1038/ngeo2269. URL <http://dx.doi.org/10.1038/ngeo2269>.
- K. Katsaros and R. Brown. *Legacy of the Seasat Mission for Studies of the Atmosphere and Air-Sea-Ice Interactions*, volume 72. 1991. doi: 10.1175/1520-0477(1991)072<0967:LOTSMF>2.0.CO;2.
- W. M. Kaula. *Theory of satellite geodesy: applications of satellites to geodesy*. Courier Corporation, 2013.
- M. G. Kendall. Further Contributions to the Theory of Paired Comparisons. *Biometrics*, 11(1):43–62, 1955. ISSN 0006341X, 15410420. URL <http://www.jstor.org/stable/3001479>.
- M. Koppes, S. Rupper, M. Asay, and A. Winter-Billington. Sensitivity of glacier runoff projections to baseline climate data in the Indus River basin. *Frontiers in Earth Science*, 3, 2015. ISSN 2296-6463. doi: 10.3389/feart.2015.00059. URL <http://journal.frontiersin.org/article/10.3389/feart.2015.00059/full>.
- V. M. Kotlyakov, A. F. Glazovskii, and I. E. Frolov. Glaciation in the arctic. *Herald of the Russian Academy of Sciences*, 80(2):155–164, Apr 2010. ISSN 1555-6492. doi: 10.1134/S1019331610020073. URL <https://doi.org/10.1134/S1019331610020073>.
- H. Kruskal, William and W. A. Wallis. Use of Ranks in One-Criterion Variance Analysis. *Journal of the American Statistical Association*, 47(260):583–621, 1952. ISSN 01621459. URL <http://www.jstor.org/stable/2280779>.
- A. N. Laghari, D. Vanham, and W. Rauch. The Indus basin in the framework of current and future water resources management. *Hydrology and Earth System Sciences*, 16(4):1063–1083, 2012. doi: 10.5194/hess-16-1063-2012. URL <https://www.hydrol-earth-syst-sci.net/16/1063/2012/>.
- F. W. Landerer and S. Swenson. Accuracy of scaled GRACE terrestrial water storage estimates. *Water resources research*, 48(4), 2012.
- C. Lang, X. Fettweis, and M. Erpicum. Stable climate and surface mass balance in Svalbard over 1979-2013 despite the Arctic warming. *The Cryosphere*, 9(1):83–101, Jan. 2015.

ISSN 1994-0424. doi: 10.5194/tc-9-83-2015. URL <http://www.the-cryosphere.net/9/83/2015/>.

- C. F. Larsen, E. Burgess, A. A. Arendt, S. O’Neel, A. J. Johnson, and C. Kienholz. Surface melt dominates Alaska glacier mass balance. *Geophysical Research Letters*, 42(14):2015GL064349, July 2015. ISSN 1944-8007. doi: 10.1002/2015GL064349. URL <http://onlinelibrary.wiley.com/doi/10.1002/2015GL064349/abstract>.
- J. T. M. Lenaerts, J. H. van Angelen, M. R. van den Broeke, A. S. Gardner, B. Wouters, and E. van Meijgaard. Irreversible mass loss of Canadian Arctic Archipelago glaciers. *Geophysical Research Letters*, 40(5):870–874, Mar. 2013. ISSN 1944-8007. doi: 10.1002/grl.50214. URL <http://onlinelibrary.wiley.com/doi/10.1002/grl.50214/abstract>.
- A. Lutz, W. Immerzeel, A. Shrestha, and M. Bierkens. Consistent increase in High Asia’s runoff due to increasing glacier melt and precipitation. 4:587–592, 06 2014.
- H. B. Mann. Nonparametric Tests Against Trend. *Econometrica*, 13(3):245–259, 1945. ISSN 00129682, 14680262. URL <http://www.jstor.org/stable/1907187>.
- S. J. Marshall. *The cryosphere*. Princeton University Press, 2011.
- K. Matsuo and K. Heki. Current Ice Loss in Small Glacier Systems of the Arctic Islands (Iceland, Svalbard, and the Russian High Arctic) from Satellite Gravimetry. *Terrestrial, Atmospheric and Oceanic Sciences*, 24(4-1):657–670, Aug. 2013. ISSN 1017-0839. doi: 10.3319/TAO.2013.02.22.01(TibXS). URL <https://eprints.lib.hokudai.ac.jp/dspace/handle/2115/53027>.
- M. McMillan, A. Shepherd, N. Gourmelen, A. Dehecq, A. Leeson, A. Ridout, T. Flament, A. Hogg, L. Gilbert, T. Benham, M. van den Broeke, J. A. Dowdeswell, X. Fettweis, B. Noël, and T. Strozzi. Rapid dynamic activation of a marine-based Arctic ice cap. *Geophysical Research Letters*, 41(24):2014GL062255, Dec. 2014. ISSN 1944-8007. doi: 10.1002/2014GL062255. URL <http://onlinelibrary.wiley.com/doi/10.1002/2014GL062255/abstract>.
- M. McMillan, A. Leeson, A. Shepherd, K. Briggs, T. W. K. Armitage, A. Hogg, M. P. Kuipers, M. Broeke, B. Noël, W. J. Berg, S. Ligtenberg, M. Horwath, A. Groh, A. Muir, and L. Gilbert. A high-resolution record of Greenland mass balance. *Geophysical Research Letters*, 43(13):7002–7010, 2016. doi: 10.1002/2016GL069666. URL <https://agupubs.onlinelibrary.wiley.com/doi/abs/10.1002/2016GL069666>.
- M. F. Meier, M. B. Dyurgerov, U. K. Rick, S. O’Neel, W. T. Pfeffer, R. S. Anderson, S. P. Anderson, and A. F. Glazovsky. Glaciers Dominate Eustatic Sea-Level Rise in the 21st Century. *Science*, 317(5841):1064–1067, 2007. ISSN 0036-8075. doi: 10.1126/science.1143906. URL <http://science.sciencemag.org/content/317/5841/1064>.
- W. Meier, F. Fetterer, M. Savoie, S. Mallory, R. Duerr, and J. Stroeve. NOAA/NSIDC Climate Data Record of Passive Microwave Sea Ice Concentration, Version 3. 2017. doi: <https://doi.org/10.7265/N59P2ZTG>. URL 10.5067/E7TYRXPJKW0Q.

- A. K. Melkonian, M. J. Willis, M. E. Pritchard, and A. J. Stewart. Recent changes in glacier velocities and thinning at Novaya Zemlya. *Remote Sensing of Environment*, 174: 244 – 257, 2016. ISSN 0034-4257. doi: <https://doi.org/10.1016/j.rse.2015.11.001>. URL <http://www.sciencedirect.com/science/article/pii/S0034425715301899>.
- R. Millan, J. Mouginot, and E. Rignot. Mass budget of the glaciers and ice caps of the Queen Elizabeth Islands, Canada, from 1991 to 2015. *Environmental Research Letters*, 12(2):024016, 2017. ISSN 1748-9326. doi: 10.1088/1748-9326/aa5b04. URL <http://stacks.iop.org/1748-9326/12/i=2/a=024016>.
- G. Moholdt, C. Nuth, J. O. Hagen, and J. Kohler. Recent elevation changes of Svalbard glaciers derived from ICESat laser altimetry. *Remote Sensing of Environment*, 114(11): 2756–2767, Nov. 2010. ISSN 0034-4257. doi: 10.1016/j.rse.2010.06.008. URL <http://www.sciencedirect.com/science/article/pii/S0034425710001987>.
- G. Moholdt, B. Wouters, and A. S. Gardner. Recent mass changes of glaciers in the Russian High Arctic. *Geophysical Research Letters*, 39(10):L10502, May 2012. ISSN 1944-8007. doi: 10.1029/2012GL051466. URL <http://onlinelibrary.wiley.com/doi/10.1029/2012GL051466/abstract>.
- J. Mouginot and E. Rignot. Ice motion of the patagonian icefields of south america: 1984–2014. *Geophysical Research Letters*, 42(5):1441–1449, 2015. doi: 10.1002/2014GL062661. URL <https://agupubs.onlinelibrary.wiley.com/doi/abs/10.1002/2014GL062661>.
- J. Nilsson, L. Sandberg Sørensen, V. R. Barletta, and R. Forsberg. Mass changes in Arctic ice caps and glaciers: implications of regionalizing elevation changes. *The Cryosphere*, 9(1):139–150, 2015a. doi: 10.5194/tc-9-139-2015. URL <https://www.the-cryosphere.net/9/139/2015/>.
- J. Nilsson, P. Vallelonga, B. Simonsen, Sebastian, L. S. Sørensen, F. René, D. Dahl-Jensen, M. Hirabayashi, K. Goto-Azuma, C. S. Hvidberg, H. A. Kjær, and K. Satow. Greenland 2012 melt event effects on CryoSat-2 radar altimetry. *Geophysical Research Letters*, 42(10): 3919–3926, 2015b. doi: 10.1002/2015GL063296. URL <https://agupubs.onlinelibrary.wiley.com/doi/abs/10.1002/2015GL063296>.
- B. Noël, W. J. Berg, S. Lhermitte, B. Wouters, N. Schaffer, and M. R. Broeke. Six Decades of Glacial Mass Loss in the Canadian Arctic Archipelago. *Journal of Geophysical Research: Earth Surface*, 0(0), 2018. doi: 10.1029/2017JF004304. URL <https://agupubs.onlinelibrary.wiley.com/doi/abs/10.1029/2017JF004304>.
- M.-J. Noh and I. M. Howat. The Surface Extraction from TIN based Search-space Minimization (SETSM) algorithm. *ISPRS Journal of Photogrammetry and Remote Sensing*, 129:55 – 76, 2017. ISSN 0924-2716. doi: <https://doi.org/10.1016/j.isprsjprs.2017.04.019>. URL <http://www.sciencedirect.com/science/article/pii/S0924271617300953>.
- C. Nuth, G. Moholdt, J. Kohler, J. Hagen, and K. Andreas. Svalbard glacier elevation changes and contribution to sea level rise. *Journal of Geophysical Research: Earth Surface*,

- 115(F1), 2010. doi: 10.1029/2008JF001223. URL <https://agupubs.onlinelibrary.wiley.com/doi/abs/10.1029/2008JF001223>.
- K. W. Oleson, D. M. Lawrence, G. B. Bonan, B. Drewniak, M. Huang, C. Koven, S. Levis, F. Li, W. Riley, Z. Subin, S. Swenson, P. E. Thornton, A. Bozbiyik, R. Fisher, C. Heald, E. Kluzek, J.-F. Lamarque, P. Lawrence, L. Leung, W. Lipscomb, S. Muszala, D. Ricciuto, W. Sacks, Y. Sun, J. Tang, and Z. L. Yang. Technical description of version 4.5 of the Community Land Model (CLM). *NCAR Technical Note*, 503+STR(July), 2013. doi: 10.5065/D6RR1W7M.
- T. J. Osborn. Winter 2009/2010 temperatures and a record-breaking North Atlantic Oscillation index. *Weather*, 66(1):19–21, 2011. doi: 10.1002/wea.660. URL <https://rmets.onlinelibrary.wiley.com/doi/abs/10.1002/wea.660>.
- E. Palazzi, J. Von Hardenberg, and A. Provenzale. Precipitation in the Hindu-Kush Karakoram Himalaya: observations and future scenarios. *Journal of Geophysical Research: Atmospheres*, 118(1):85–100, 2013.
- W. Peltier. GLOBAL GLACIAL ISOSTASY AND THE SURFACE OF THE ICE-AGE EARTH: The ICE-5G (VM2) Model and GRACE. *Annual Review of Earth and Planetary Sciences*, 32(1):111–149, 2004. doi: 10.1146/annurev.earth.32.082503.144359. URL <https://doi.org/10.1146/annurev.earth.32.082503.144359>.
- M. Pelto. *New Zealand*, chapter 11, pages 171–186. Wiley-Blackwell, 2016. ISBN 9781119068150. doi: 10.1002/9781119068150.ch11. URL <https://onlinelibrary.wiley.com/doi/abs/10.1002/9781119068150.ch11>.
- Pfeffer, A. A. Arendt, A. Bliss, T. Bolch, J. G. Cogley, A. S. Gardner, J. O. Hagen, R. Hock, G. Kaser, C. Kienholz, E. Miles, G. Moholdt, N. Molg, F. Paul, V. Radic, P. Rastner, B. Raup, J. Rich, M. J. Sharp, and C. Randolph. The Randolph Glacier Inventory: a globally complete inventory of glaciers. *Journal of Glaciology*, 60:537–552, 2014. doi: 10.3189/2014JoG13J176.
- E. Pohl, R. Gloaguen, and R. Seiler. Remote Sensing-Based Assessment of the Variability of Winter and Summer Precipitation in the Pamirs and Their Effects on Hydrology and Hazards Using Harmonic Time Series Analysis. *Remote Sensing*, 7(8):9727–9752, July 2015. doi: 10.3390/rs70809727. URL <http://www.mdpi.com/2072-4292/7/8/9727>.
- H. N. Pollack. Spherical harmonic representation of the gravitational potential of a point mass, a spherical cap, and a spherical rectangle. *Journal of Geophysical Research*, 78(11):1760–1768, Apr. 1973. ISSN 2156-2202. doi: 10.1029/JB078i011p01760. URL <http://onlinelibrary.wiley.com/doi/10.1029/JB078i011p01760/abstract>.
- H. D. Pritchard. Asia’s glaciers are a regionally important buffer against drought. *Nature*, 545:169–176, 2017. doi: 10.1038/nature22062. URL <http://dx.doi.org/10.1038/nature22062>.

- H. D. Pritchard, S. R. M. Ligtenberg, H. A. Fricker, D. G. Vaughan, M. R. van den Broeke, and L. Padman. Antarctic ice-sheet loss driven by basal melting of ice shelves. *Nature*, 484:502, apr 2012. URL <http://dx.doi.org/10.1038/nature10968><http://10.0.4.14/nature10968><https://www.nature.com/articles/nature10968>{#}supplementary-information.
- R. Przybylak and P. Wyszyński. Air temperature in Novaya Zemlya Archipelago and Vaygach Island from 1832 to 1920 in the light of early instrumental data. *International Journal of Climatology*, 37(8):3491–3508, 2016. doi: 10.1002/joc.4934. URL <https://rmets.onlinelibrary.wiley.com/doi/abs/10.1002/joc.4934>.
- V. Radić, A. Bliss, A. C. Beedlow, R. Hock, E. Miles, and J. G. Cogley. Regional and global projections of twenty-first century glacier mass changes in response to climate scenarios from global climate models. *Climate Dynamics*, 42(1):37–58, Jan 2014. ISSN 1432-0894. doi: 10.1007/s00382-013-1719-7. URL <https://doi.org/10.1007/s00382-013-1719-7>.
- R. K. Raney. The delay/Doppler radar altimeter. *IEEE Transactions on Geoscience and Remote Sensing*, 36(5):1578–1588, Sep 1998. ISSN 0196-2892. doi: 10.1109/36.718861.
- P. Rastner, T. Strozzi, and F. Paul. Fusion of Multi-Source Satellite Data and DEMs to Create a New Glacier Inventory for Novaya Zemlya. *Remote Sensing*, 9(11), 2017. ISSN 2072-4292. doi: 10.3390/rs9111122. URL <http://www.mdpi.com/2072-4292/9/11/1122>.
- N. A. Rayner, D. E. Parker, E. B. Horton, C. K. Folland, L. V. Alexander, D. P. Rowell, E. C. Kent, and A. Kaplan. Global analyses of sea surface temperature, sea ice, and night marine air temperature since the late nineteenth century. *Journal of Geophysical Research: Atmospheres*, 108(D14), 2003. doi: 10.1029/2002JD002670. URL <https://agupubs.onlinelibrary.wiley.com/doi/abs/10.1029/2002JD002670>.
- J. T. Reager, A. S. Gardner, J. S. Famiglietti, D. N. Wiese, A. Eicker, and M.-H. Lo. A decade of sea level rise slowed by climate-driven hydrology. *Science*, 351(6274):699–703, Feb. 2016. ISSN 0036-8075, 1095-9203. doi: 10.1126/science.aad8386. URL <http://science.sciencemag.org/content/351/6274/699>.
- L. Rey, P. de Chateau-Thierry, L. Phalippou, C. Mavrocordatos, and R. Francis. SIRAL, a high spatial resolution radar altimeter for the Cryosat mission. In *IGARSS 2001. Scanning the Present and Resolving the Future. Proceedings. IEEE 2001 International Geoscience and Remote Sensing Symposium (Cat. No.01CH37217)*, volume 7, pages 3080–3082 vol.7, 2001. doi: 10.1109/IGARSS.2001.978261.
- R. Rietbroek, S.-E. Brunnabend, J. Kusche, J. Schröter, and C. Dahle. Revisiting the contemporary sea-level budget on global and regional scales. *Proceedings of the National Academy of Sciences*, 113(6):1504–1509, Feb. 2016. ISSN 0027-8424, 1091-6490. doi: 10.1073/pnas.1519132113. URL <http://www.pnas.org/content/113/6/1504>.
- E. Rignot and P. Kanagaratnam. Changes in the velocity structure of the Greenland Ice Sheet. *Science*, 311(5763):986–990, 2006.

- M. Roca, S. Laxon, and C. Zelli. The EnviSat RA-2 Instrument Design and Tracking Performance. *IEEE Transactions on Geoscience and Remote Sensing*, 47(10):3489–3506, Oct 2009. ISSN 0196-2892. doi: 10.1109/TGRS.2009.2020793.
- M. Rodell and H. Beaudoin. GLDAS Noah Land Surface Model L4 3 hourly 0.25 x 0.25 degree V2.1. 2016. doi: 10.5067/E7TYRXPJKWOQ. URL 10.5067/E7TYRXPJKWOQ.
- M. Rodell, I. Velicogna, and J. Famiglietti. Satellite Based Estimates of Groundwater Depletion in India. *Nature*, 460:999–1002, 09 2009. doi: 10.1038/nature08238. URL <http://dx.doi.org/10.1038/nature08238>.
- S. Rupper, J. M. Schaefer, L. K. Burgener, L. S. Koenig, K. Tsering, and E. R. Cook. Sensitivity and response of Bhutanese glaciers to atmospheric warming. *Geophysical Research Letters*, 39(19):L19503, Oct. 2012. ISSN 1944-8007. doi: 10.1029/2012GL053010. URL <http://onlinelibrary.wiley.com/doi/10.1029/2012GL053010/abstract>.
- T. Schenk and B. Csatho. A New Methodology for Detecting Ice Sheet Surface Elevation Changes From Laser Altimetry Data. *IEEE Transactions on Geoscience and Remote Sensing*, 50(9):3302–3316, Sept 2012. ISSN 0196-2892. doi: 10.1109/TGRS.2011.2182357.
- E. J. O. Schrama, B. Wouters, and R. Rietbroek. A mascon approach to assess ice sheet and glacier mass balances and their uncertainties from GRACE data. *Journal of Geophysical Research: Solid Earth*, 119(7):6048–6066, July 2014. ISSN 2169-9356. doi: 10.1002/2013JB010923. URL <http://onlinelibrary.wiley.com/doi/10.1002/2013JB010923/abstract>.
- C. Schwatke, D. Dettmering, W. Bosch, and F. Seitz. DAHITI - an innovative approach for estimating water level time series over inland waters using multi-mission satellite altimetry. *Hydrology and Earth System Sciences*, 19(10):4345–4364, 2015. doi: 10.5194/hess-19-4345-2015. URL <https://www.hydrolog-earth-syst-sci.net/19/4345/2015/>.
- L. Serebryanny and E. Malyasova. The Quaternary vegetation and landscape evolution of Novaya Zemlya in the light of palynological records. *Quaternary International*, 45-46:59 – 70, 1998. ISSN 1040-6182. doi: [https://doi.org/10.1016/S1040-6182\(97\)00007-4](https://doi.org/10.1016/S1040-6182(97)00007-4). URL <http://www.sciencedirect.com/science/article/pii/S1040618297000074>.
- B. Sevruk, M. Ondrás, and B. Chvíla. The WMO precipitation measurement intercomparisons. *Atmospheric Research*, 92(3):376–380, 2009.
- A. Sharov, W. Schöner, and R. Pail. Spatial features of glacier changes in the Barents-Kara Sector. 11:3046, 03 2009.
- D. Shepard. A Two-dimensional Interpolation Function for Irregularly-spaced Data. In *Proceedings of the 1968 23rd ACM National Conference*, ACM '68, pages 517–524, New York, NY, USA, 1968. ACM. doi: 10.1145/800186.810616. URL <http://doi.acm.org/10.1145/800186.810616>.

- M. R. Siegfried, R. L. Hawley, and J. F. Burkhart. High-Resolution Ground-Based GPS Measurements Show Intercampaign Bias in ICESat Elevation Data Near Summit, Greenland. *IEEE Transactions on Geoscience and Remote Sensing*, 49(9):3393–3400, Sept 2011. ISSN 0196-2892. doi: 10.1109/TGRS.2011.2127483.
- B. E. Smith, C. R. Bentley, and C. F. Raymond. Recent elevation changes on the ice streams and ridges of the Ross Embayment from ICESat crossovers. *Geophysical Research Letters*, 32(21), 2005. doi: 10.1029/2005GL024365. URL <https://agupubs.onlinelibrary.wiley.com/doi/abs/10.1029/2005GL024365>.
- B. E. Smith, H. A. Fricker, I. R. Joughin, and S. Tulaczyk. An inventory of active subglacial lakes in Antarctica detected by ICESat (2003–2008). *Journal of Glaciology*, 55(192):573–595, 2009. doi: 10.3189/002214309789470879.
- L. S. Sørensen, A. H. Jarosch, G. Aðalgeirsdóttir, V. R. Barletta, R. Forsberg, F. Pálsson, H. Björnsson, and T. Jóhannesson. The effect of signal leakage and glacial isostatic rebound on GRACE-derived ice mass changes in Iceland. *Geophysical Journal International*, 209(1):226–233, Apr. 2017. ISSN 0956-540X. doi: 10.1093/gji/ggx008. URL <http://dx.doi.org/10.1093/gji/ggx008>.
- T. Strozzi, F. Paul, A. Wiesmann, T. Schellenberger, and A. Kääb. Circum-Arctic Changes in the Flow of Glaciers and Ice Caps from Satellite SAR Data between the 1990s and 2017. *Remote Sensing*, 9(9), 2017. ISSN 2072-4292. doi: 10.3390/rs9090947. URL <http://www.mdpi.com/2072-4292/9/9/947>.
- Z. Sun, H. Lee, Y. Ahn, A. Aierken, K. H. Tseng, M. A. Okeowo, and C. K. Shum. Recent Glacier Dynamics in the Northern Novaya Zemlya Observed by Multiple Geodetic Techniques. *IEEE Journal of Selected Topics in Applied Earth Observations and Remote Sensing*, 10(4):1290–1302, April 2017. ISSN 1939-1404. doi: 10.1109/JSTARS.2016.2643568.
- T. C. Sutterley, I. Velicogna, B. Csatho, M. van den Broeke, S. Rezvan-Behbahani, and G. Babonis. Evaluating Greenland glacial isostatic adjustment corrections using GRACE, altimetry and surface mass balance data. *Environmental Research Letters*, 9(1):014004, 2014.
- S. Swenson and J. Wahr. Methods for inferring regional surface-mass anomalies from Gravity Recovery and Climate Experiment (GRACE) measurements of time-variable gravity. *Journal of Geophysical Research: Solid Earth*, 107(B9):ETG–3, 2002.
- S. Swenson and J. Wahr. Post-processing removal of correlated errors in GRACE data. *Geophysical Research Letters*, 33(8), 2006a. doi: 10.1029/2005GL025285. URL <https://agupubs.onlinelibrary.wiley.com/doi/abs/10.1029/2005GL025285>.
- S. Swenson and J. Wahr. Post-processing removal of correlated errors in GRACE data. *Geophysical Research Letters*, 33(8), 2006b.
- S. Swenson, D. Chambers, and J. Wahr. Estimating geocenter variations from a combination of GRACE and ocean model output. *Journal of Geophysical Research: Solid Earth*, 113

- (B8):B08410, Aug. 2008. ISSN 2156-2202. doi: 10.1029/2007JB005338. URL <http://onlinelibrary.wiley.com/doi/10.1029/2007JB005338/abstract>.
- B. D. Tapley, S. Bettadpur, M. Watkins, and C. Reigber. The gravity recovery and climate experiment: Mission overview and early results. *Geophysical Research Letters*, 31(9):L09607, May 2004. ISSN 1944-8007. doi: 10.1029/2004GL019920. URL <http://onlinelibrary.wiley.com/doi/10.1029/2004GL019920/abstract>.
- M. Tedesco, J. E. Box, J. Cappelen, R. S. Fausto, X. Fettweis, K. Hansen, T. Mote, C. J. P. P. Smeets, D. v. As, R. S. W. v. d. Wal, and J. Wahr. Greenland Ice Sheet [in Arctic Report Card 2015]. *Arctic Report Card*, pages 22–32, Dec. 2015. URL <https://academiccommons.columbia.edu/catalog/ac:196257>.
- V. M. Tiwari, J. Wahr, and S. Swenson. Dwindling groundwater resources in northern India, from satellite gravity observations. *Geophysical Research Letters*, 36(18):L18401, Sept. 2009. ISSN 1944-8007. doi: 10.1029/2009GL039401. URL <http://onlinelibrary.wiley.com/doi/10.1029/2009GL039401/abstract>.
- M. van den Broeke, J. Bamber, J. Ettema, E. Rignot, E. Schrama, W. J. van de Berg, E. van Meijgaard, I. Velicogna, and B. Wouters. Partitioning recent greenland mass loss. *science*, 326(5955):984–986, 2009.
- W. Van Wychen, D. O. Burgess, L. Gray, L. Copland, M. Sharp, J. A. Dowdeswell, and T. J. Benham. Glacier velocities and dynamic ice discharge from the Queen Elizabeth Islands, Nunavut, Canada. *Geophysical Research Letters*, 41(2):2013GL058558, Jan. 2014. ISSN 1944-8007. doi: 10.1002/2013GL058558. URL <http://onlinelibrary.wiley.com/doi/10.1002/2013GL058558/abstract>.
- D. Vaughan, J. Comiso, I. Allison, J. Carrasco, G. Kaser, R. Kwok, P. Mote, T. Murray, F. Paul, J. Ren, E. Rignot, O. Solomina, K. Steffen, and T. Zhang. Observations: Cryosphere. *Climate Change 2013: The Physical Science Basis. Contribution of Working Group I to the Fifth Assessment Report of the Intergovernmental Panel on Climate Change*, pages 317–382, 2013. doi: 10.1017/CBO9781107415324.012.
- I. Velicogna. Increasing rates of ice mass loss from the Greenland and Antarctic ice sheets revealed by GRACE. *Geophysical Research Letters*, 36(19), 2009. doi: 10.1029/2009GL040222. URL <https://agupubs.onlinelibrary.wiley.com/doi/abs/10.1029/2009GL040222>.
- I. Velicogna and J. Wahr. Greenland mass balance from GRACE. *Geophysical Research Letters*, 32(18), 2005.
- I. Velicogna and J. Wahr. Time-variable gravity observations of ice sheet mass balance: Precision and limitations of the GRACE satellite data. *Geophysical Research Letters*, 40(12):3055–3063, June 2013. ISSN 1944-8007. doi: 10.1002/grl.50527. URL <http://onlinelibrary.wiley.com/doi/10.1002/grl.50527/abstract>.

- I. Velicogna, T. Sutterley, and M. Van Den Broeke. Regional acceleration in ice mass loss from Greenland and Antarctica using GRACE time-variable gravity data. *Geophysical Research Letters*, 41(22):8130–8137, 2014a.
- I. Velicogna, T. C. Sutterley, and M. R. van den Broeke. Regional acceleration in ice mass loss from Greenland and Antarctica using GRACE time-variable gravity data. *Geophysical Research Letters*, 41(22):8130–8137, Nov. 2014b. ISSN 1944-8007. doi: 10.1002/2014GL061052. URL <http://onlinelibrary.wiley.com/doi/10.1002/2014GL061052/abstract>.
- S. A. Venegas and L. A. Mysak. Is There a Dominant Timescale of Natural Climate Variability in the Arctic? *Journal of Climate*, 13(19):3412–3434, 2000. doi: 10.1175/1520-0442(2000)013<3412:ITADTO>2.0.CO;2. URL [https://doi.org/10.1175/1520-0442\(2000\)013<3412:ITADTO>2.0.CO;2](https://doi.org/10.1175/1520-0442(2000)013<3412:ITADTO>2.0.CO;2).
- C. Vörösmarty, C. Federer, and A. Schloss. Potential evaporation functions compared on us watersheds: Possible implications for global-scale water balance and terrestrial ecosystem modeling. *Journal of Hydrology*, 207(3):147 – 169, 1998. ISSN 0022-1694. doi: [https://doi.org/10.1016/S0022-1694\(98\)00109-7](https://doi.org/10.1016/S0022-1694(98)00109-7). URL <http://www.sciencedirect.com/science/article/pii/S0022169498001097>.
- J. Wahr, M. Molenaar, and F. Bryan. Time variability of the Earth’s gravity field: Hydrological and oceanic effects and their possible detection using GRACE. *Journal of Geophysical Research: Solid Earth*, 103(B12):30205–30229, 1998. doi: 10.1029/98JB02844. URL <https://agupubs.onlinelibrary.wiley.com/doi/abs/10.1029/98JB02844>.
- J. Wahr, S. Swenson, and I. Velicogna. Accuracy of GRACE mass estimates. *Geophysical Research Letters*, 33(6):L06401, Mar. 2006. ISSN 1944-8007. doi: 10.1029/2005GL025305. URL <http://onlinelibrary.wiley.com/doi/10.1029/2005GL025305/abstract>.
- J. Wahr, R. S. Nerem, and S. V. Bettadpur. The pole tide and its effect on GRACE time-variable gravity measurements: Implications for estimates of surface mass variations. *Journal of Geophysical Research: Solid Earth*, 120(6):2015JB011986, June 2015. ISSN 2169-9356. doi: 10.1002/2015JB011986. URL <http://onlinelibrary.wiley.com/doi/10.1002/2015JB011986/abstract>.
- J. M. Wahr. Time-variable gravity from satellites. 2015.
- F. Wang, J. L. Bamber, and X. Cheng. Accuracy and Performance of CryoSat-2 SARIn Mode Data Over Antarctica. *IEEE Geoscience and Remote Sensing Letters*, 12(7):1516–1520, July 2015. ISSN 1545-598X. doi: 10.1109/LGRS.2015.2411434.
- Q. Wang, S. Yi, and W. Sun. Precipitation-driven glacier changes in the Pamir and Hindu Kush mountains. *Geophysical Research Letters*, 44(6):2017GL072646, Mar. 2017. ISSN 1944-8007. doi: 10.1002/2017GL072646. URL <http://onlinelibrary.wiley.com/doi/10.1002/2017GL072646/abstract>.

- R. Williams and J. Ferrigno. *Glaciers of Asia*: U.S. Geological Survey. *Professional Paper*, 1386-F:349, 2010.
- M. J. Willis, A. K. Melkonian, M. E. Pritchard, and A. Rivera. Ice loss from the Southern Patagonian ice field, South America, between 2000 and 2012. *Geophysical research letters*, 39(17), 2012.
- D. Wingham, C. Francis, S. Baker, C. Bouzinac, D. Brockley, R. Cullen, P. de Chateau-Thierry, S. Laxon, U. Mallow, C. Mavrocordatos, L. Phalippou, G. Ratier, L. Rey, F. Rostan, P. Viau, and D. Wallis. CryoSat: A mission to determine the fluctuations in Earth's land and marine ice fields. *Advances in Space Research*, 37(4):841–871, 2006. ISSN 0273-1177. doi: <https://doi.org/10.1016/j.asr.2005.07.027>. URL <http://www.sciencedirect.com/science/article/pii/S0273117705009348>. Natural Hazards and Oceanographic Processes from Satellite Data.
- D. J. Wingham, A. J. Ridout, R. Scharroo, R. J. Arthern, and C. K. Shum. Antarctic Elevation Change from 1992 to 1996. *Science*, 282(5388):456–458, 1998. ISSN 0036-8075. doi: 10.1126/science.282.5388.456. URL <http://science.sciencemag.org/content/282/5388/456>.
- B. Wouters, A. Martín-Español, V. Helm, T. Flament, J. M. van Wessem, S. R. M. Ligtenberg, M. R. van den Broeke, and J. L. Bamber. Dynamic thinning of glaciers on the Southern Antarctic Peninsula. *Science*, 348(6237):899–903, 2015. ISSN 0036-8075. doi: 10.1126/science.aaa5727. URL <http://science.sciencemag.org/content/348/6237/899>.
- T. Yao, L. Thompson, W. Yang, W. Yu, Y. Gao, X. Guo, X. Yang, K. Duan, H. Zhao, B. Xu, J. Pu, A. Lu, Y. Xiang, D. B. Kattiel, and D. a. Joswiak. Different glacier status with atmospheric circulations in Tibetan Plateau and surroundings. *Nature Climate Change*, 2:663, 07 2012. doi: 10.1038/nclimate1580. URL <http://dx.doi.org/10.1038/nclimate1580>.
- A. Yatagai, K. Kamiguchi, O. Arakawa, A. Hamada, N. Yasutomi, and A. Kitoh. APHRODITE: Constructing a Long-Term Daily Gridded Precipitation Dataset for Asia Based on a Dense Network of Rain Gauges. *Bulletin of the American Meteorological Society*, 93(9):1401–1415, 2012. doi: 10.1175/BAMS-D-11-00122.1. URL <https://doi.org/10.1175/BAMS-D-11-00122.1>.
- G. Young and K. Hewitt. Hydrology research in the upper Indus basin, Karakoram Himalaya, Pakistan. *IAHS Publ*, 190:139–152, 1990.
- J. Zeeberg. *Climate and glacial history of the Novaya Zemlya Archipelago, Russian Arctic*. 2001. doi: 10.13140/RG.2.1.4498.1209.
- J. Zeeberg and S. L. Forman. Changes in glacier extent on north Novaya Zemlya in the twentieth century. *The Holocene*, 11(2):161–175, 2001. doi: 10.1191/095968301676173261. URL <https://doi.org/10.1191/095968301676173261>.

- J. J. Zeeberg, S. L. Forman, and L. Polyak. Glacier extent in a Novaya Zemlya fjord during the "Little Ice Age" inferred from glaciomarine sediment records. *Polar Research*, 22(2): 385–394, 2003. doi: 10.1111/j.1751-8369.2003.tb00119.x. URL <https://onlinelibrary.wiley.com/doi/abs/10.1111/j.1751-8369.2003.tb00119.x>.
- J. Zhan, H. Shi, Y. Wang, and Y. Yao. Complex principal component analysis of mass balance changes on the Qinghai–Tibetan Plateau. *The Cryosphere*, 11(3):1487–1499, 2017. doi: 10.5194/tc-11-1487-2017. URL <https://www.the-cryosphere.net/11/1487/2017/>.
- M. Zhao, J. Ramage, K. Semmens, and F. Obleitner. Recent ice cap snowmelt in Russian High Arctic and anti-correlation with late summer sea ice extent. *Environmental Research Letters*, 9(4):045009, 2014. URL <http://stacks.iop.org/1748-9326/9/i=4/a=045009>.
- Z. Zuo and J. Oerlemans. Contribution of glacier melt to sea-level rise since AD 1865: a regionally differentiated calculation. *Climate Dynamics*, 13(12):835–845, Dec 1997. ISSN 1432-0894. doi: 10.1007/s003820050200. URL <https://doi.org/10.1007/s003820050200>.
- H. Zwally, B. Schutz, W. Abdalati, J. Abshire, C. Bentley, A. Brenner, J. Bufton, J. Dezio, D. Hancock, D. Harding, T. Herring, B. Minster, K. Quinn, S. Palm, J. Spinhirne, and R. Thomas. ICESat’s laser measurements of polar ice, atmosphere, ocean, and land. *Journal of Geodynamics*, 34(3):405 – 445, 2002. ISSN 0264-3707. doi: [https://doi.org/10.1016/S0264-3707\(02\)00042-X](https://doi.org/10.1016/S0264-3707(02)00042-X). URL <http://www.sciencedirect.com/science/article/pii/S026437070200042X>.